UNIVERSIDADE DE SÃO PAULO
INSTITUTO DE GEOCIÊNCIAS

"High-resolution paleoclimate reconstruction of the last 9000 years based on speleothem isotope records from northeastern Venezuela"

NATHALIE MELISSA MARTINEZ MEDINA

Dissertação apresentada ao Programa Geociências (Geoquímica e Geotectônica) para a obtenção do título de Mestra em Ciências.

Área de concentração: Geoquímica dos Processos Exógenos

Orientador: Prof. Dr. Francisco William da Cruz Junior

São Paulo
2022

Serviço de Biblioteca e Documentação do IGc/USP

Ficha catalográfica gerada automaticamente com dados fornecidos pelo(a) autor(a)
via programa desenvolvido pela Seção Técnica de Informática do ICMC/USP

Bibliotecários responsáveis pela estrutura de catalogação da publicação:
Sonia Regina Yole Guerra - CRB-8/4208 | Anderson de Santana - CRB-8/6658

M. Medina, Nathalie Melissa
High-resolution paleoclimate reconstruction of the last 9000 years based on speleothem isotope records from northeastern Venezuela / Nathalie Melissa M. Medina; orientador Francisco William da Cruz Junior. -- São Paulo, 2022.
102 p.

Dissertação (Mestrado - Programa de Pós-Graduação em Geoquímica e Geotectônica) -- Instituto de Geociências, Universidade de São Paulo, 2022.

1. Inter-tropical Convergence Zone. 2. Holocene. 3. Venezuela. 4. Speleothems. 5. Cariaco Basin. I. da Cruz Junior, Francisco William, orient. II. Título.

UNIVERSIDADE DE SÃO PAULO
INSTITUTO DE GEOCIÊNCIAS

“High-resolution paleoclimate reconstruction of the last 9000 years based on speleothem isotope records from northeastern Venezuela”

NATHALIE MELISSA MARTÍNEZ MEDINA

Orientador: Prof. Dr. Francisco William da Cruz Junior

Dissertação de Mestrado

Nº 889

COMISSÃO JULGADORA

Dr. Francisco William da Cruz Junior

Dra. Marília de Carvalho Campos Garcia

Dr. Valdir Felipe Novello

São Paulo
2022

A mis padres: Lucero y Bernardo.

ACKNOWLEDGMENTS

Thanks to São Paulo Research Foundation (FAPESP) for financial support through grant 2019/16745-1 and FAPESP Project 2017/50085-3. I would like to thank my advisor, Chico, for his guidance and support throughout the process of completing this work. And Amos Winter for providing the speleothems samples which are the focus of this current work. This project would not have been possible without the collaboration of Haiwei Zhang and his students, who conducted the vast majority of the U-Th dating analyses. And the work of Marcela Della Libera and Julio Cauhy in obtaining some preliminary dates. I also thank Professor Sergio Foghin from the Experimental Libertador University (Venezuela) for providing meteorological data from the INAMEH.

I am also grateful with the people from the *Grupo Sistemas Cársticos*: Veronica, Giselle, Angela and Nicolás, and to the Stable Isotope Laboratory (LES-CPGEO) at the Geoscience Institute (USP). Special thanks to Angela Ampuero and Victor Chavez Mayta who helped me with the back-trajectory and cluster analysis. And Andrés Zúñiga for the support with R.

Finally, I would like to thank my family and friends for their unconditional love and support.

"Nos quedaremos algunos meses en Caracas, de entrada, estamos aquí en el más divino y rico país. Plantas maravillosas: gymnotos*, tigres, armadillos, monos, loros y cantidad de indígenas semisalvajes, raza humana muy bella e interesante (…).*

La ciudad está situada en un golfo, detrás de un anfiteatro de 5 a 8,000 pies de altura, (…), rodeado de montañas adornadas de bosques (…).

¡Qué árboles! Cocoteros de 50 a 60 pies de altura (…), plátanos y una masa de árboles con hojas monstruosas y flores perfumadas de tamaño de una mano (…). Y qué colores poseen los pájaros, los peces, hasta los cangrejos (azul cielo y amarillo) (…).

Lo que es más bello aún que estas maravillas vistas particularmente, es la impresión que produce el conjunto de esta naturaleza (…) poderosa, exuberante, y sin embargo tan dulce, tan fácil, tan serena. Siento que sería muy feliz aquí y que estas impresiones me alegrarán frecuentemente todavía en lo porvenir."

(Humboldt., A, V. Cartas Americanas, Cumaná, 16 julio, 1799, ed, Charles Minguet, 1980, pp. 13-14)

RESUMO

Medina, N.M.M., 2022, High-resolution paleoclimate reconstruction of the last 9000 years based on speleothem isotope records from northeastern Venezuela [Master's Thesis], São Paulo, Instituto de Geociências, Universidade de São Paulo, 102 p.

Existem poucos registros paleoclimáticos de alta resolução disponíveis de regiões localizadas sob influência direta da Zona de Convergência Inter-tropical (ZCIT) na América do Sul, sendo a Bacia de Cariaco uma das áreas com maior número de estudos. O presente trabalho é baseado em registros isotópicos de alta resolução de $\delta^{18}O$ e $\delta^{13}C$ de espeleotemas de duas cavernas localizadas nas adjacências da Bacia de Cariaco, os quais cobrem a maior parte dos últimos 9,0 ka, durante o Holoceno. Os dados isotópicos obtidos indicam oscilações climáticas em escalas de tempo multidecenal a secular, ainda pouco estudadas na região da ZCIT, que são comparadas a outros registros isotópicos de alta resolução no Atlântico Norte, Caribe e região tropical da América do Sul. Os dados isotópicos sugerem que as condições climáticas mais frias no Atlântico Norte durante os eventos Bond estão associadas com mudanças na precipitação no nordeste da Venezuela, assim como na produtividade primária na Bacia de Cariaco. Entretanto, a relação climática com registros caribenhos depende da magnitude destes eventos e da fase de insolação vigente. O clima predominantemente úmido é observado na Venezuela e Caribe durante o Holoceno médio entre 8,1-6,5 ka, enquanto condições mais secas ocorrem no evento de maior magnitude, Bond (4), por volta de 5,5 ka. Já em eventos de menor intensidade e de mais curta duração, como o Bond 3, a comparação entre registros isotópicos sugere um estreitamento da ZCIT entre Venezuela e Barbados, que resultou em condições mais secas a norte em Cuba e a sul no Peru. O registro de espeleotema da caverna Caripe, nordeste da Venezuela, difere significativamente do registro das concentrações de titânio da Bacia de Cariaco durante os últimos 2300 anos. Durante este período, é observado o predomínio de uma relação climática antífásica com os registros caribenhos e em fase com os registros mais a sul, no domínio do Sistema de Monção Sul Americana (SMSA). Contrário ao que foi descrito em estudos anteriores da Bacia de Cariaco, os dados de espeleotemas indicam um clima mais seco na região costeira da Venezuela no período correspondente a Anomalia Climática do Período Medieval (900-

1100 CE). Já o período da Pequena Idade do Gelo, foi marcado pela não deposição de espeleotema, possivelmente associada a condições mais secas e o deslocamento mais a sul da ZCIT, que intensificou o regime de chuvas do SMSA em parte do continente sul-americano.

Palavras chave: Zona de Convergência Inter-tropical, Holoceno, Venezuela, espeleotemas, Bacia de Cariaco, paleoclima, isótopos estáveis, América do Sul, Caribe, Ciclos Bond.

ABSTRACT

Medina, N.M.M., 2022, High-resolution paleoclimate reconstruction of the last 9000 years based on speleothem isotope records from northeastern Venezuela [Master's Thesis], São Paulo, Instituto de Geociências, Universidade de São Paulo, 102 p.

Few high-resolution paleoclimate proxy records exist in the region located under the direct influence of the Inter-tropical Convergence Zone (ITCZ) in South America (SA); most of them retrieved from the Cariaco Basin (CB) off the coast of Venezuela. Here we present new high-resolution $\delta^{18}O$ and $\delta^{13}C$ records of speleothems collected in caves in the region adjacent to the CB in Venezuela, covering the Mid and Late Holocene. We document previously undetected multidecadal- to secular-scale climate variability in the core region of the ITCZ, which is being compared to other high-resolution records from the North Atlantic (NA), Caribbean and southern tropical South America. We show that the northeastern Venezuelan Holocene hydroclimate variability and the input of nutrients, productivity and oxygen demand in the CB has primary (but not exclusively) responded to NA climate (Bond cycles). However, the magnitude of those events and the background insolation conditions might have been the main determinants. Increased Northern Hemisphere (NH) insolation during the Mid-Holocene likely led to mostly in-phase relation between Venezuela and eastern Caribbean records (i.e. wet conditions occurred between 8.1-6.5 ka despite coinciding with Bond 5, due to the enhanced NH insolation and northward position of the ITCZ, whereas dry conditions were observed during the strongest of the Bond Cycles (4) around 5.5 ka). In addition, the comparison between the speleothem record of this study and other ones suggest that ITCZ stayed between Venezuela and Barbados as a narrower band during weaker and shorter events such as the Bond 3 with drying conditions observed to the north in Cuba and to the south in Peru. Our NE Venezuela record from Caripe Cave considerable differs from the Cariaco Basin Ti record during the last 2.3 ka. Pointing to non-previously reported relations to Caribbean and southern hemisphere tropical high-resolution records. During this period an out-phase relation is observed between Venezuela and Caribbean records and rather appears to be closely related to the South American Monsoon System (SAMS) dynamics. Contrary to results from previous studies in Cariaco, our results point out to drier conditions during

Medieval Climate Anomaly (MCA, 900-1100 CE) close to the coast in Venezuela. No speleothem deposition occurred during most of Little Ice Age (LIA) which might be related to dryer conditions in response to a southward position that led to major moisture income to the SASM domain.

Key words: Inter-tropical Convergence Zone, Holocene, Venezuela, speleothems, Cariaco Basin, paleoclimate, stable isotopes, South America, Caribbean, Bond Cycles.

INDEX

LIST OF FIGURES

LIST OF ABBREVIATIONS

AABW – Antarctic Bottom Water

AMO – Atlantic Multidecadal Oscillation

AMOC – Atlantic Meridional Overturning Circulation

AWP – Atlantic Warm Pool

CB – Cariaco Basin

cps – counts per second

DJF – December-January-February

ENSO – El Niño Southern Oscillation

GNIP – Global Network of Isotopes in Precipitation

GPM – Global Precipitation Measurement

HS – Heinrich Stadials

HSG – Hematite-stained grains

IAEA – United Nations International Atomic Energy Agency

INAMEH – Instituto Nacional de Meteorología e Hidrología, Venezuela

ITCZ – Inter-tropical Convergence Zone

IRDs – Ice-rafted debris

IRMS – Isotope Ratio Mass Spectrometry

JJA – June-July-August

LIA – Little Ice Age

masl – meters above sea level

MAM – March-April-May

mbsl – meters below sea level

MCA – Medieval Climate Anomaly

Mo – Molybdenum

MOC – Meridional Overturning Circulation

NA – North Atlantic

NASH – North Atlantic Subtropical High

ND – November-December

NADW – North Atlantic Deep Water

OLR – Outgoing Longwave Radiation

OM – Organic matter

SA – South America

Ti – Titanium

SA – South America

SO – September-October

SOI – Southern Oscillation Index

SON – September-October-November

SSTs – Sea surface temperatures

VPDB – Vienna Pee Dee Belemnite

VSMOW – Vienna Standard Mean Ocean Water

Wiser – Water Isotope System for data analysis, visualization, and Electronic Retrieval

WMO – World Meteorological Organization

LIST OF SYMBOLS

% – Percent

‰ – Permil

^{2}H – Hydrogen stable isotope with 1 proton and 1 neutron: deuterium

^{18}O – Oxygen stable isotope with 8 protons and 10 neutrons

O_2 – Oxygen

$\delta^{18}O$ – Delta eighteen

$\delta^{13}C$ – Delta thirteen

CO_2 – Carbon dioxide

1. INTRODUCTION

1.1. What is the ITCZ?

The Inter-tropical Convergence Zone (ITCZ) is defined as a narrow or confined latitudinally low-pressure band of atmospheric deep convective clouds along the equator, where northerly and southerly trade winds converge and most of the rain of the Earth falls (Philander et al., 1996; Waliser & Gautier, 1993). During a year cycle the ITCZ migrates meridionally depending on the amount of solar radiation received on Earth by season and by latitude. Similarly, on longer time scales, paleo-records (Deplazes et al., 2013; Haug et al., 2001; Lea et al., 2003;) and modeling studies (Broccoli et al., 2006; Chiang & Bitz, 2005) have revealed that the ITCZ migrates, with some exceptions, towards a differentially warming hemisphere (Schneider, Bischoff, & Haug, 2014; Adam, Bischoff, & Schneider, 2016). Although the solar radiation has a maximum at the equator, the ITCZ location is not uniform around the globe. Currently, over the central Atlantic and Pacific oceans, the ITCZ migrates between 9°N in boreal summer and 2°N in boreal winter. And over the Indian Ocean and adjacent land surfaces, between 20°N in boreal summer and 8°S in boreal winter. Then, mean position of the ITCZ around the Earth´s middle situates further north at 6°N (Schneider et al., 2014). The explanation for this asymmetry is the northwards heat transport across the equator by the Atlantic Meridional Overturning Circulation (AMOC). Compensated by the southward atmospheric heat transport achieved by shifting the tropical circulation northward of the equator (Marshall et al., 2014) .

Given that there is no unambiguous definition for the ITCZ in reason of the number of different variables used to describe it, in addition to the confusion derived from the extrapolation of the ITCZ concept to land (Nicholson, 2018); two parameters have been frequently used to track the ITCZ position. The latitude of maximum precipitation (above a specific quantile) and minimum outgoing longwave radiation (OLR) in each longitude (Gu & Zhang, 2002; Mamalakis et al., 2021). Reminding that quantity of OLR is inversely related to the deep convective cloudiness (Poveda et al., 2006), as the cloud cover hamper the emission of electromagnetic radiation from the Earth and its atmosphere out to the space. However, continuing research based on observations and simulations has intended to unify the above parameters into a formula to describe the position of the ITCZ

and its rainfall intensity: the atmospheric energy balance equation (Schneider, Bischoff & Haug, 2014). Defined as the absorbed solar radiation at the top of the atmosphere, minus the outgoing longwave radiation and any ocean energy uptake owing to transport or storage in the oceans (Schneider, Bischoff & Haug, 2014).

The ITCZ must be seen as an atmosphere-ocean interplay coupled by the trade winds near the surface. Which are especially important over the Atlantic and Pacific Oceans, where the continents are less influential (Philander et al., 1996). The Hadley cell meridional overturning circulation is the atmospheric process controlling zonal-mean ITCZ position. While the belt of ocean currents (Meridional Overturning Criculation-MOC) has a key role in transporting large amounts of heat and salt around the world and thus in determining the inter-hemispheric heat balance (Manabe and Stouffer, 1999).

Hadley cells rise tropical air masses to the upper troposphere through evaporation (Schneider, Bischoff & Haug, 2014; Davis, et al., 2016). As the sun-warmed ocean heats the overlying air, air becomes less dense due to an increase in the particle´s kinetic energy and rises. As air rises, loses temperature and its capacity of retaining moisture, becomes supersaturared and some of its water vapor condenses into water droplets. Those condensed water droplets form clouds. When enough moisture has condensed and the droplets have grown too heavy to stay suspended by air currents, fall as rain. This rising air near the ocean surface is replaced by air masses from north and south of the equator which are deflected to the west due to the Coriolis effect, creating the easterly trade winds. Trade winds blow southwest toward the equator in the Northern Hemisphere (northeasterlies), and northwest toward the equator in the Southern Hemisphere (southeasterlies). In the upper troposphere, air masses detrain from clouds and diverge in the Northern and Southern hemispheres and subside at approximately 30°N and 30°S, respectively, in the extra-tropics at the subtropical highs. From here, air masses flow back to the equator through warm and moist surface zonal winds (Schneider, Bischoff & Haug, 2014; Davis, et al., 2016). Because these trade winds converge near the equator, the tropical rain belt occurring over the ocean is known to meteorologists as the Inter-tropical Convergence Zone. Whereas, the expression of the convectively equatorial active zone over the inland area is observed as rather scattered cloud masses known as the equatorial trough (Riehl, 1979).

The AMO (Manabe and Stouffer, 1999) is manifested in the Atlantic Ocean as the AMOC. As is described by Kuhlbrodt et al., (2007), the AMOC consist of four main branches: the wind-driven processes that transport cold depth water near to the surface through upwelling at the Southern Ocean; the surface currents that accumulate warm and less saline waters on their path through the tropical waters toward northern high latitudes; the Southern (Antarctic Bottom Water, AABW) and the North Atlantic Deep Water (NADW) formation branches; together with the deep currents closing the loop.

Since the AMOC effectively contributes to the warming of the North Atlantic it is reasonable to think that a change in some of this branches would have its strongest response around this region (Vellinga & Wood, 2002; Schmittner et al., 2005). However, significant changes may occur over the entire globe. Various climate reconstructions/simulations of past and future scenarios, shows that increasing meltwater input into the North Atlantic may cause a slowdown of the AMOC (negative AMOC phase) or even the collapse of the oceanic heat transport (Vellinga & Wood, 2002; Schmittner et al., 2005). Not only triggering colder and drier conditions in much of the Northern Hemisphere, but also a relatively warmer Southern Hemisphere, stronger northeasterly winds, southward shift of the ITCZ over the Atlantic and eastern Pacific Basins, and enhanced precipitation in South America and Africa monsoon regions (Vellinga & Wood, 2002).

1.2. High Resolution Western Atlantic ITCZ Paleorecords: Cariaco Basin Sedimentary and Stable Isotope Records in Speleothems

Since the recovery of the first sediments cores from Cariaco Basin (CB) in 1957 (Peterson et al., 2000b), several proxy data sets were analyzed. Some of them reaching a temporal depth of up to 600.000 years BP (Gibson & Peterson, 2014; Peterson et al., 2000b), covering over five glacial cycles, with an extraordinary sampling interval of up to 5 years for the last 14 ka (Haug et al., 2001). Hence, CB located at 10°N has become the biggest source of information of northern South American paleoclimate and a worldwide reference to the ITCZ position. However, the spatial distribution of ITCZ rainfall over continental northern South America remained more speculative. Until the high-resolution $\delta^{18}O$ speleothem record from Caracos Cave located in the eastern Andean Cordillera at 6°N

came into light, revealing the complementary picture of ITCZ variability for a period spanning almost the entire last glacial cycle (Ramirez, 2018).

CB off the coast of Venezuela is an east-west trending pull apart basin that actually consist of two small sub-basins reaching depths of ~1400 mbsl, separated by a shallower central saddle of ~900 mbsl. Surrounding this structural depression to the north, the much shallower Tortuga Bank that extends from the Margarita Island to the east, to Cabo Cordera to the west, acts like a barrier that limits the exchange of waters with the rest of the Caribbean (Fig. 1) (Peterson et al., 2000b; Sweere et al., 2016).This key feature in combination with the large sedimentation rates (0.3 to >1 mm/year) make the CB a particularly sensitive repository to high-latitude climatic events. Such as the expansion and demise of polar ice sheets during glacial-interglacial transitions accompanied by dramatic sea level changes. And the trigger of a rapid tropical feedback through atmospheric-ocean teleconnections (Chiang & Bitz, 2005; Lea et al., 2003). Indeed, the correlation between Greenland temperatures (ice core $\delta^{18}O$ in ‰; Wolff et al., 2010) to past changes in CB ventilation (Mo in cps, Gibson & Peterson, 2014), upwelling (gray scale from 0-255; Hughen et al., 2000 and total reflectance in L*; Deplazes et al., 2013), surface productivity (alkenone concentration in µg/g sediment, Herbert & Schuffert, 2000) and sea surface temperatures (Mg/Ca in mmol/mol; Lea et al., 2003) point to a link between NH cooling and the strengthening of trade wind-driven upwelling in a situation analogous to the nowadays boreal winter dry season (December-January-February).

Like northern Venezuela, central Colombia also experiences a dry season during boreal winter due to the southward shift of the ITCZ. However, Ramirez, (2018) showed that during the Last Glacial Cycle there was a prevalence of an antiphased relationship with the Cariaco Basin at orbital (Marine Isotopes Stages) and millennial (Greenland Stadials and Interstadials) scales. Exceptions were observed in extreme cold events known as Heinrich Stadials (HS) in which both, the Cariaco Basin and central Colombia experienced a shortfall of precipitation. Providing evidence to the southward displacement of the ITCZ, already suggested by the enhancement of the South American Monsoon System (SAMS) (Cruz et al., 2009; X. Wang et al., 2004), weakening of the AMOC (Bohm et al., 2015; McManus et al., 2004; Mulitza et al., 2017) and a suite of water-hosing modeling studies (Kageyama et al., 2013).

Dry (wet) periods were observed in the Caracos speleothem stable-isotope record as enriched (depleted) $\delta^{18}O$ values. Whilst, in the CB were interpreted/observed in the lithology and geochemistry proxies as oxic (anoxic) bottom waters, colder (warmer) sea surface temperatures, and as lighter (darker), inorganic-biogenic (organic-carbon-rich), typically bioturbated (laminated) sediments. Besides, high detrital Fe and Ti abundances during periods of warm interstadials are thought to indicate increased terrigenous input to the Cariaco Basin, implying higher rainfall and increased runoff from the local watersheds. Namely of the small drainages of Cumaná, Neverpi, Unare and Tuy rivers (Fig. 1) (Deplazes et al., 2019; González et al., 2008; Haug et al., 2001; Peterson et al., 2000).

The coherence of the above-mentioned proxies has certainly probed to reflect ITCZ past meridional migrations in close synchronicity with NH climate in orbital to millennial time scales. Particularly for the Holocene, the consistency between the variability observed in the numerous proxy records from the CB is less apparent. Still, the Ti concentrations in sediments (Haug et al., 2001) have been used in several proxy comparisons and modeling studies as unequivocally evidence for the southward displacement of the ITCZ, following the gradual decrease in local insolation since the mid-Holocene, leading to rainfall diminution in northern Venezuela. Other Holocene data from the CB such of oxygen balance (Gibson & Peterson, 2014) and sediment color (Deplazes et al., 2013) instead shows a marked cyclicity pattern during the Mid Holocene. And for the Late Holocene, an opposite scenario to the Ti interpretation is exposed by progressively darker sediments approaching the present (Hughen et al., 2000), which might indicate a greater terrigenous input by increased river discharges expected by an ITCZ directly overhead. Then, the present study aims to reconcile the exposed discrepancies by providing new independent high-resolution $\delta^{18}O$ and $\delta^{13}C$ hydroclimate proxies from stalagmites collected in two caves located just 20 km of the Cariaco Basin. And contribute to northern South America hydroclimate reconstructions by giving important time windows of the Holocene period.

2. OBJECTIVES

2.1. General Objective

To carry out paleoclimatic and paleoenvironmental reconstructions based on $\delta^{18}O$ and $\delta^{13}C$ profiles from stalagmites collected in northern Venezuela caves, spanning the most of Holocene.

2.2. Specific Objectives

- To understand the factors driving precipitation variability and stable isotope composition of rain along the ITCZ region in northern Venezuela.
- To describe secular to multidecadal hydroclimate variability from Early to Late Holocene periods.
- To compare $\delta^{18}O$ and $\delta^{13}C$ profiles to the nearby Cariaco Basin records as well as to other high-resolution time series from the Caribbean and South American regions.
- To discuss possible forcing mechanisms involved in the observed stalagmite stable isotopes variability.

3. STUDY SITE

3.1. Environmental Characterization

Alfredo Jahn and Caripe caves are located close to the coastal region in northeastern Venezuela, nearby the CB (Fig. 1). Alfredo Jahn Cave (10°28´45´´N, 66°16´24´´W, 210 masl) is located in Brión Municipality, Miranda State, over the westernmost portion of the Bay of Cariaco, over the lower altitude foothills of the Serranía del Litoral (Central Coastal Cordillera). It is also located close to the Tuy depression, which is part of the region known as “Llanura de Barlovento”. Whereas, Caripe Cave is located in Caripe municipality, Mónagas State (10°10´27´´N, 63°33´06´´W, 1090 masl), at the easternmost portion of the Cariaco Gulf, over the hills of the Eastern Coastal Cordillera.

Alfredo Jahn Cave (also known as Cueva de la Tapa del Cambural) is hosted in calcitic and calcitic dolomitic marbles of Las Mercedes Formation of early Cretaceous age (Forti, Urbani & Rossi, 1999; Urbani, 1973). The cave has a horizontal development of 4292 m, 67 m a deep and 15 entrances (Urbani, 1973). The permanent Cambural creek flows through parts of the cave, sinking and re-emerging at different points (Forti, Urbani & Rossi, 1999). A map of the Cave with the description of its chambers and corridors can be consulted in the *Boletín de la Sociedad Espeleológica de Venezuela* (SEV, 1973).

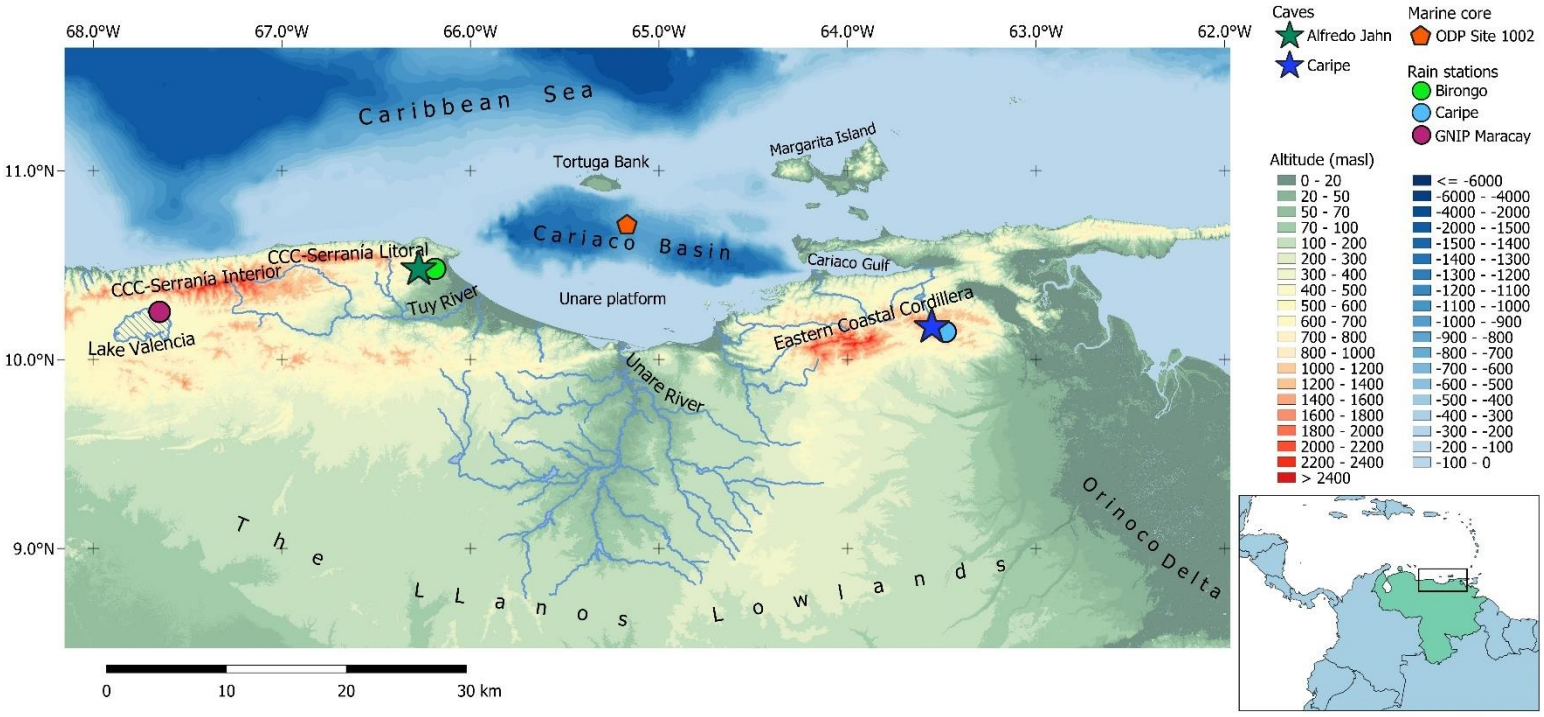

Fig. 1. Map of North Central-Eastern Venezuela showing the location of Alfredo Jahn (green star) and Caripe caves (blue star). Birongo (90 masl, green dot) and Caripe (960 masl, blue dot) closest rain stations to the cave sites are also shown (INAMEH), along with the Maracay GNIP station (442 masl, pink dot) next to the Lake Valencia (IAEA/WMO, 2021). Note the proximity of both caves to the Cariaco Basin. Marine sediment ODP Site 1002C (orange hexagon, Haug et al., 2001) represent one of the many cores retrieved from the central saddle of the Basin. CCC: Central Coastal Cordillera.

Currently, speleogenesis is thought to be dominated by erosion and corrosion rather than by calcite precipitation processes. The thickness of the rock above the cave is variable from 10 to 30 meters. The local vegetation is typical of a seasonal, semi-deciduous sub-montane ombrophilous broadleaf forest (Fig. 2). Which means that even with well distributed rainfall throughout the year (ombrophilous), some trees lose their foliage (semi-deciduous) with characteristic large surface-area (broadleaf) for a brief period during the short dry season. The climate is hot and rainy, with average annual precipitation around 1970 mm. The interior temperature of the cave oscillates between 22°C and 24.6°C (Urbani, 1973). Unfortunately, there is no information about relative humidity inside this cave.

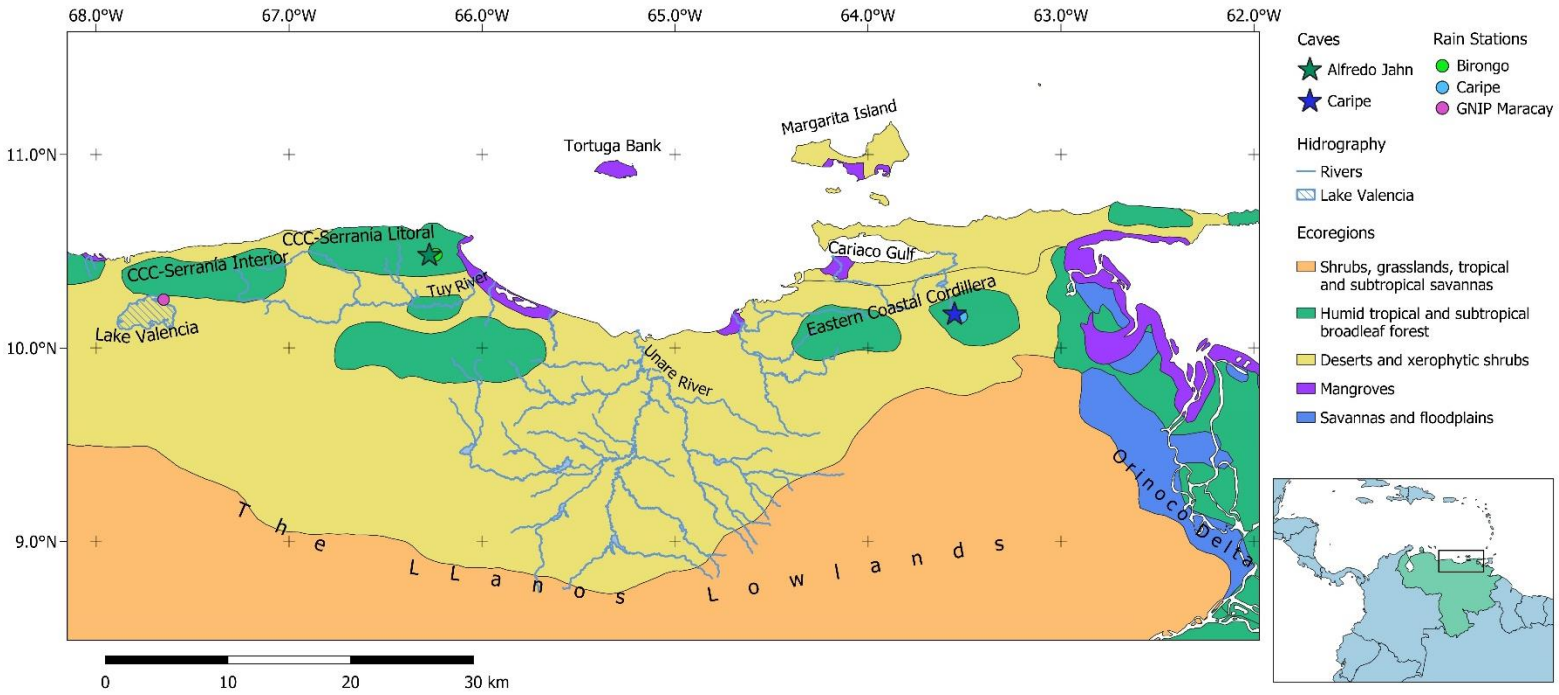

Fig. 2. Map showing the ecosystems of North Central-Eastern Venezuela. Both, Alfredo Jahn (green star) and Caripe (blue star) situates in the humid tropical and subtropical broadleaf forest patches surrounded by deserts. CCC: Central Coastal Cordillera. From Porto (2005), based on Olson (2001) and World Wildlife Fund (2003).

Caripe Cave (mostly known as Guácharos Cave) is the third largest cave of Venezuela with a horizontal development of 10100 meters and up to 338 entrances (Urbani, 1999, 1995). The map of the Cave was published in two parts, separated by the "El paso del Viento" which divides the touristic (SVE, 1968) from the non-touristic sections (SVE, 1971). Caripe Cave is hosted in the top of the massive 170m thick limestone levels of the Guácharo Member of El Cantil Formation of Aptian-Albian ages (Yoris et al., 1992), just 30 or 40 meters below the upper stratigraphic limit. Structurally this is a very complex zone, with several anticlines and synclines, much of them are overturned and faulted (Rod, 1959; Urbani, 1971). As there are no faults in the direction of the principal axis of the cave, its formation is thought to be controlled by the planes of stratification and the action of the Quebrada de la Cueva creek (Rod, 1959). The climate is humid, with temperatures between 16 and 24°C and average annual precipitation around 1400 mm. Mean cave temperature is 18.5°C and relative humidity 95% (Pérez, 1970). The adjacent regions of the Caripe Cave are mostly surrounded by agricultural terrains mainly dedicated to coffee production. Only some forested areas remains in the hill above the cave and along the Rio Negro immediately west of the Cave (Tannenbaum & Wrege, 1978). Those correspond to tall, canopied montane ombrophilous, sub-evergreen broadleaf forests (Fig. 2).

3.2. Modern Climate

3.2.1. Interannual variability

The Atlantic Multidecadal Oscillation (AMO) (Enfield et al., 2001; Kerr, 2000) and El Niño Southern Oscillation (ENSO) are the dominant mode of low-frequency climate variability in the Atlantic and Pacific Oceans, respectively. Natural fluctuations in sea surface temperatures (SSTs) of these basins are known to influence inter-annual hydroclimate variability around the globe (Enfield et al., 2001; Poveda et al., 2006; Sutton & Hodson, 2005). With important effects over tropical regions including Venezuela (Hetzinger et al.,

2008; Pulwarty et al., 1992). Based on instrumental analyses, various indices have been derived to account for anomalous SSTs in each basin. The AMO index is typically constructed by averaging North Atlantic SSTs and then subtracting a background time series to remove the anthropogenic changes (Frajka-Williams et al., 2017). Average SSTs of certain regions in the Pacific Ocean constitute the different ENSO indices for characterizing anomalous temperatures in this basin. While, the Southern Oscillation Index (SOI) tracks the atmospheric part of the of the ENSO by comparing the surface air pressure anomalies in the western Pacific (Darwin, Australia), to pressure anomalies in the central Pacific (Tahiti).

3.2.1.1. Atlantic Multidecadal Oscillation (AMO)

Warmer SST anomalies in the North Atlantic occur during positive AMO phases, while colder SST conditions are observed during negative AMO phases. Over the last 160 yrs, two full AMO cycles have been captured in the instrumental period (1856 to present) with a duration between 40- to 80-yr (Kerr, 2000; Lapointe et al., 2020). The last cold phase of the AMO index was from 1961 to 1990 (Frajka-Williams et al., 2017), followed by positive phase which have been linked to the strong hurricane activity observed during the last decades with direct impacts on Venezuelan precipitation (Hetzinger et al., 2008), since its northern coast lies within the main development region of Atlantic Hurricanes (Goldenberg et al., 2001). Anthropogenic warming might be also likely responsible for the observed trends in tropical Atlantic and hurricane development as well (Mann & Emanuel, 2006). Accounting for the influence of the recent global warming trend, positive AMO phases are associated to positive rainfall anomalies in the northernmost portion of SA either by enhanced hurricane activity or the northward displacement of the ITCZ (Goldenberg et al., 2001; Knight et al., 2006). Whereas, negative AMO phases are likely related to southward position of the ITCZ deriving in negative precipitation anomalies in Venezuela (Kayano & Capistrano, 2014).

3.2.1.2. El Niño Southern Oscillation (ENSO) and Southern Oscillation index (SOI)

ENSO quasi periodic oscillation of SSTs over the Pacific region occurs approximately every 3–7 years, fluctuating between two extremes known as El Niño corresponding to

the warm phase (positive SST anomaly), and La Niña, the cooling phase (negative SST anomaly) (NOAA). Usually during warm El Niño, SOI is in its negative phase, that means that the pressure is lower than average over the central Pacific and higher than average over Australia. During La Niña, the SOI is positive and the anomalies are reversed. However, ENSO phases can occur independently of SOI fluctuations (Diaz & Pulwarty, 1992).

Those ocean and atmosphere anomalies in the Pacific Basin affect the tropical Atlantic climate as a result of adjustments in the location and strength of the Hadley and Walker circulations (Kayano & Capistrano, 2014). In general, in Venezuela, El Niño is related with positive (warmer) air temperature anomalies and negative anomalies of precipitation. While La Niña has the opposite effect, with cooler temperatures and positive anomalies of precipitation (Poveda et al., 2006; Pulwarty et al., 1992). Nevertheless, the precipitation variability driven by ENSO can have particular manifestations in timing and amplitude (López Pérez, 2012).

3.2.2. Annual cycle of precipitation

The main atmospheric system that controls the annual cycle of rainfall over the region comprised by the above-mentioned caves is the meridional migration of the ITCZ (Fig.3) (Poveda et al., 2006; Pulwarty et al., 1992), leading into two main dry and wet seasons. The dry season occur during January to March when the ITCZ is located in its southernmost latitudinal range over the Brazilian Nordeste (Chiessi et al., 2021; Cruz et al., 2009; Utida et al., 2020). Whereas, the wet season occur from May to December, when the ITCZ progressively migrates toward the north, which represents around 85% and 88% of the annual rainfall totals of Birongo-1515 (1862 ± 414 mm) and Caripe-1886 (1146 ± 202 mm), the closest meteorological stations to the Alfredo Jahn and Caripe Caves, respectively (Fig. 1,3,4). During April to May, the band of atmospheric deep convective clouds reaches the Guianas. Then, during the boreal summer (June-July-August, JJA) situates over Venezuela. Reaching its northernmost position over the central Lesser Antilles in the subsequent months during September-October (SO) (Martinez et al., 2019) (Fig.3). From where it migrates toward the south, again standing over Venezuela during the last months of the year (November-December, ND).

Bimodal precipitation regimes in the northeastern portion of SA respond to the double passage of the ITCZ during the year cycle. With one peak associated to the monsoon or first passage of the ITCZ during JJA and the other, to the second passage during November-December. However, unimodal patterns are also observed as a conspicuous or absent ND peak. Which is primary associated to inland-more sheltered and/or high elevation sites (Appendix figures A1-A5).

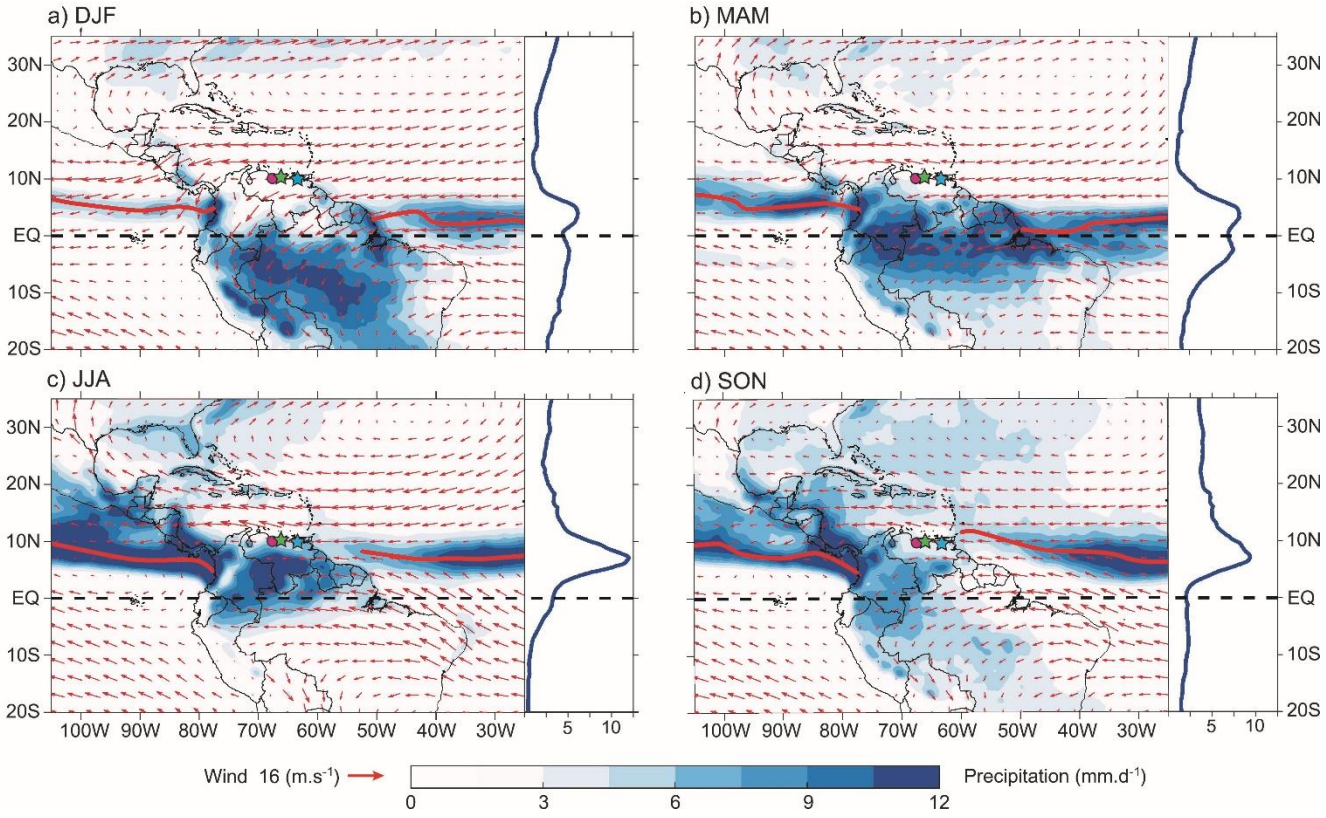

Fig. 3. Seasonal mean precipitation in mm d^{-1} from 2001 to 2020 (GPM, Huffman et al., 2019) (blue shadow scale) and seasonal mean low-level wind circulation in m.s-1 at 850 hPa from 2001 to 2020 (ERA5) (red vectors). Green star: Alfredo Jahn Cave. Blue star: Caripe Cave. Pink dot: Maracay GNIP Station. The red line marks the approximate position of the ITCZ, based on the meridional maximum precipitation values. The blue line in the left panels marks the mean latitude in which the increase in precipitation occurs (mm/day) for each season evaluated. Black dotted line: equatorial line.

Indeed, the rainfall annual totals of Birongo-1515 and Caripe-1886 are distributed in a bimodal precipitation pattern with rainfall season maxima occurring in JJA and ND at Birongo station (Fig. 4a) And in a unimodal pattern with roughly uniform precipitation from June to November, with a more notable peak in July at the higher elevation Caripe station (Fig. 4b). Maracay GNIP station (702 ± 176 mm), next to the Lake Valencia, also has a unimodal rainfall pattern (Fig. 14) and is located to the leeward sites of the high elevation mountains of the Serrania del Interior in the Central Coastal Cordillera (Fig. 1). Looking the geographical pattern of precipitation in a broader scale, there is an apparent relation of bimodality with the regions exposed to moisture-laden winds. Moreover, those stations in which the major precipitation peak occur in ND are located at low-elevation areas or slopes situated on the sides facing the northeasterly winds (Appendix figures A1-A5). As is further supported by the cluster analyses of precipitation in the Cariaco hydrographic basin (Fig. 5).

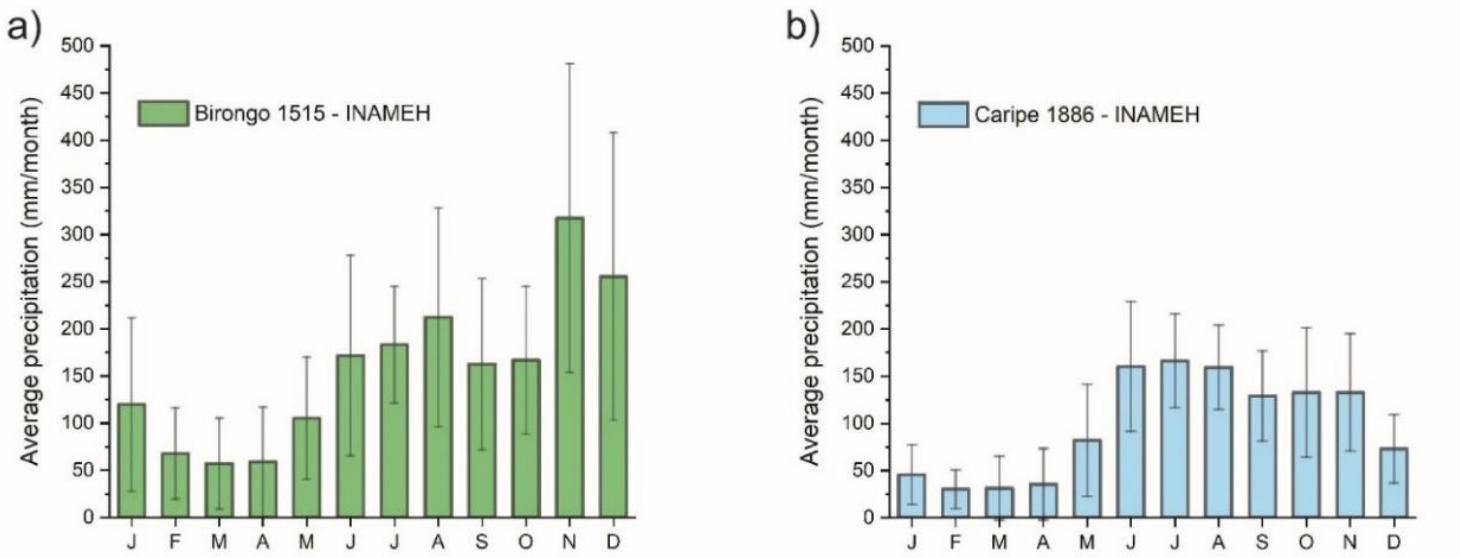

Fig. 4. Monthly mean precipitation for INAMEH (Instituto Nacional de Meteorología e Hidrología, Venezuela) meteorological stations located closest to cave sites a) Birongo-1515 (Alfredo Jahn Cave). b) Tierra Blanca-1886 (Caripe Cave). Birongo monthly data is roughly continuous between the years 1951-1954 and 1960-1999, and Caripe between 1960-2007. Error bars correspond to +/- 1 sigma.

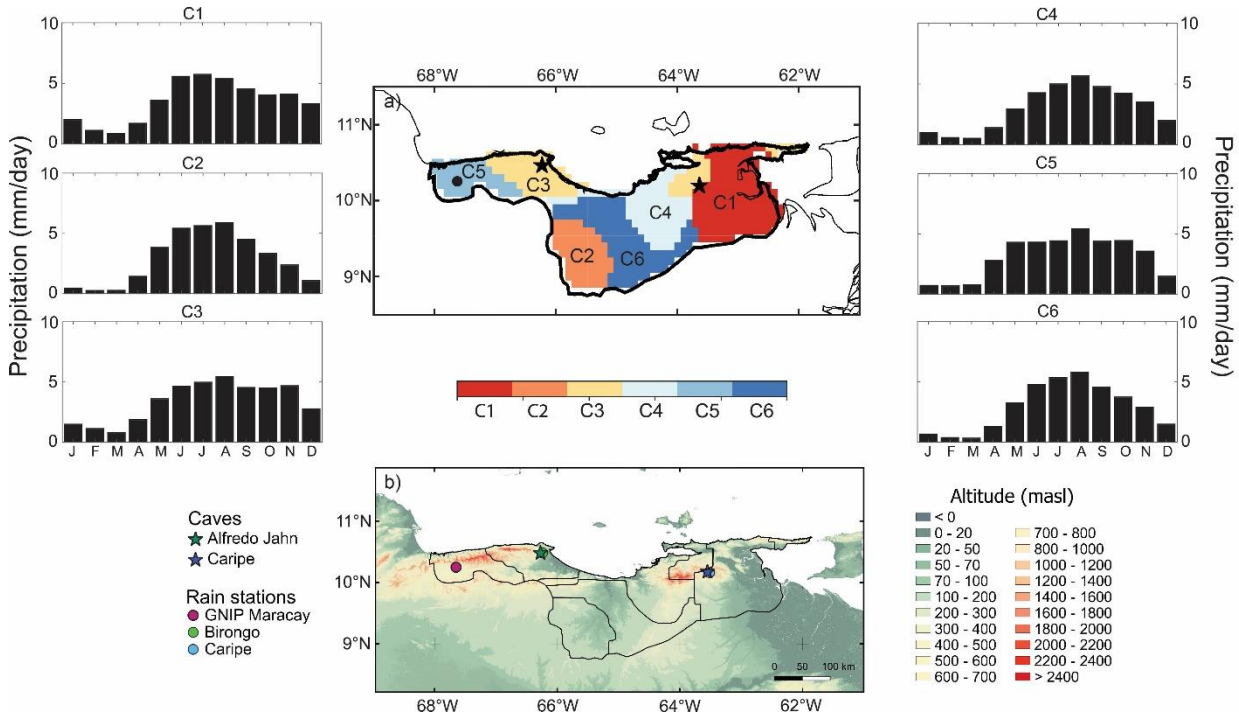

Fig. 5. a) Cluster analysis of precipitation over the Cariaco hydrographic basin. Each different color represents one cluster: a region grouped by similar characteristics in the total precipitation amounts and its annual distribution. The panels at the sides shows the average regime reconstructed for each cluster. **b)** Map showing the correspondence of each cluster to the topography. The stars represent the caves sites and the dots the rainfall stations.

Noteworthy, Alfredo Jahn and Caripe caves fall within the windward regions grouped in clusters 3 and 1, whose reconstructed regimens show a precipitation peak in November. Additionally, to the most pronounced monsoon peak occurring in August and July, respectively. The remaining clusters 2, 4, 5 and 6 only show the rainfall maxima associated to the summer monsoon and as observed above, are located inland in the Unare depression (Fig. A3), or mostly leeward as in the region corresponding to cluster 5, where Maracay GNIP station was grouped (Fig. 5).

4. SAMPLES AND METHODS

4.1. Speleothem Samples

Venezuelan speleothems VEAJ from Alfredo Jahn Cave and VECA from Caripe Cave were collected in 2012 as part of a study of recent Caribbean paleoclimate. VEAJ is a 340 mm-long stalagmite that grew in three major parts (Fig. 6). The lower stalagmite (VEAJ-base) grew first and has axes that slightly shifted to the sides, as a result of drip realignments due to overburden changes or perhaps by the opening of new adjacent dripping ducts as the previous one got sealed with time. Two adjacent stalagmites grew over the top of the lower one: the top left (VEAJ-top left) and top right (VEAJ- top right), also characterized by significant changes in axis position (Fig. 6). Sample VECA is a 314 mm long stalagmite. The first 191 mm from the base underwent dissolution and reprecipitation of carbonate in the central portion, leading to a vitreous luster that contrasts with the pristine white-colored layers on the sides (Fig. 7).

4.2. U-Th Dating Method

Subsampling for U-Th-dating analysis was carried out at the Laboratório de Sistemas Cársticos, Instituto de Geociências, University of São Paulo (Brazil). First, a longitudinal section of the stalagmites was previously polished by using a *Bosch Angular Wet Polishing Machine Gns 5-100* with five different grits (50, 200, 400, 800 and 1500 for the final surface finish). Then, a handheld drill was used to take approximately 0.100g of the least porous, not colored, most traceable layers at the side of the growth axis (Fig. 6-7). Drilling was made in the layers devoid of any visible dissolution or recrystallization. Special care was taken in the subsampling of the bottom segment of VECA speleothem. Here, the drilling was performed in the clearly unaffected adjacent layers of characteristic pristine white color, which contrast the vitreous luster of the altered portions (Fig. 7). Between each subsampling the drill bit was blown with compressed air and carefully clean with a solution of HNO_3 at a concentration of 41%, distilled water, and ethyl alcohol. Stalagmite surface was also blown with compressed air and clean with alcohol before each drill to avoid any possible contamination. Powder samples were stored in glass jars and meticulously marked with the sample name, weight and distance from the top. A total of 72 U-Th dating in speleothems was performed at the Institute of Global Environmental

Change at Xi'an Jiaotong University in China (Appendix Tables A1-A2). Few samples (6) were analyzed in the University of Minnesota in the USA. A multicollector inductively coupled plasma mass spectrometer (MC-ICP-MS-Thermo-Finnigan NEPTUNE) was operated following the procedures described by Cheng et al., (2013).

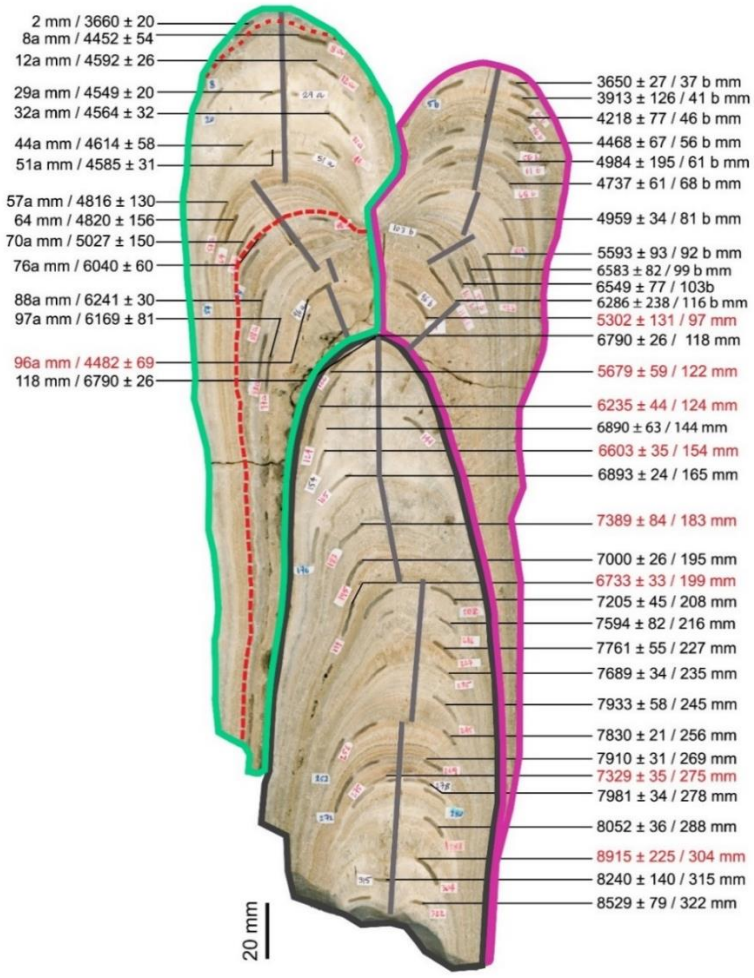

Fig. 6. Sample VEAJ from Alfredo Jahn Cave (Venezuela) with the color outlines enclosing the major three growth axes (VEAJ-base, dark gray; VEAJ-top left, green; and VEAJ-top right, pink). Milling channels for stable isotopes are shown in light gray. Depths from the top of the stalagmite to the sample location (mm) and their corresponding U-Th dates in years BP (1950) are shown. A total of 48 U-Th dates were produced for VEAJ: 21 for the VEAJ-base, 14 for VEAJ-top left and 12 for VEAJ-top right. The date in 6790±26 was common to the three stalagmites, so it was included in the three independent age models. Dates in red were find as outliers by StalAge algorithm (Scholz & Hoffmann,

2011). Red dashed lines represent hiatuses identified after the age modeling of VEAJ-top left (between 5014-6112 and 4479-4400 yrs BP).

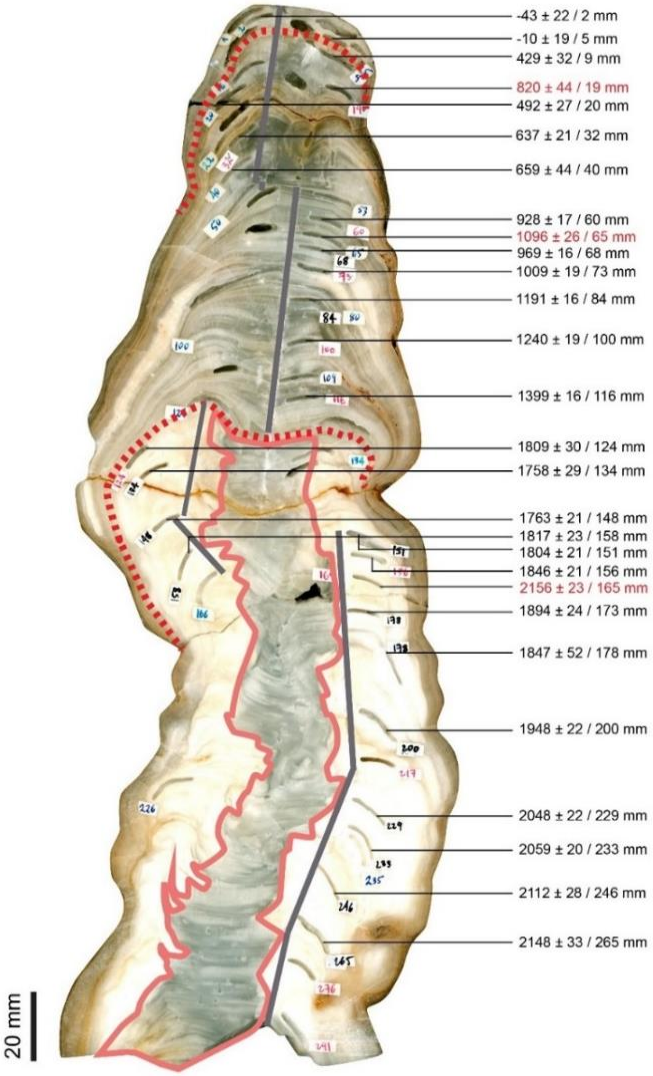

Fig. 7. Sample VECA from Caripe Cave (Venezuela). Depths from the top of the stalagmite to the sample location (mm) and their corresponding U-Th dates in years BP (1950) are shown. A total of 28 U-Th dates were produced for this sample, of which 3 dates were identified as outliers when constructing the age model by using StalAge algorithm (Scholz & Hoffmann, 2011). Pink color outline encloses the vitreous portion of post-depositional crystals formed by calcium carbonate reprecipitation after primary crystal dissolution. Milling channels for stable isotopes (dark gray lines) in the lower half of the stalagmite were taken in the pristine white-colored layers on the sides, avoiding the reprecipitated parts. Milling channels in the upper half followed the stalagmite growth axis

when possible. Red dashed lines represent hiatuses identified in the StalAge model (Scholz & Hoffmann, 2011).

4.3. Stable Isotopes Analyses

Approximately 200 µg of $CaCO_3$-powder subsamples for $\delta^{18}O$ and $\delta^{13}C$ stable isotopic analyses were collected using a manually controlled Sherline 5400 milling device along the growth axes at a resolution of 0.4 mm for samples VEAJ (Fig. 6) and 0.5 mm for VECA (Fig. 7). Stable isotope profile in the bottom section of VECA was done avoiding the altered carbonate in the inner portion of the stalagmite (Fig. 7), which might not give systematic differences with the profile taken from the original calcite in the central axis (Fairchild et al., 2006). Analyses were carried out by using an Isotope Ratio Mass Spectrometer (IRMS) coupled to a Gas Bench II at the Stable Isotopes Laboratory (LES-CPGeo), Geoscience Institute, University of São Paulo (Brazil). δ-notation in per mil units (‰) was used to express the sample isotopic ratios deviation from the Vienna Pee Dee Belemnite (VPDB) standard. The $\delta^{18}O$ and $\delta^{13}C$ isotopic profiles of VEAJ-base, VEAJ-top left and VEAJ-top right are based on 530, 310 and 250 samples, respectively. VECA isotopic profiles consist of 670 samples.

The procedure for the analysis of 1 set consisting of 56 samples and 16 standards occurs in a 72°C thermostated sample tray, takes approximately 24 hours and is comprised of three phases: flush, acid bath and data acquisition. During the flushing procedure the atmospheric air is removed from the sample vials by using He (Fig. 8). Then, previously calibrated microliter pump injects about the same amount of anhydrous phosphoric acid H_3PO_4 (98%) into the sample vials containing the $CaCO_3$ powder, converting the calcite to CO_2 as shown in the following reaction:

$$CaCO_3 + 2H^+ \rightarrow CO_2 + H_2O + Ca^{2+} \qquad \textbf{Eq. 1}$$

Since all the C in the calcite is transferred to the CO_2 there is no fractionation and the $\delta^{13}C$ measured for the gas is the same as the calcite. However, as one of the three oxygen atoms in the calcite is loss, the oxygen molecule will fractionate and thus $\delta^{18}O$ in the gas will differ considerable from the calcite. Fortunately, the oxygen isotopic contents in the $CaCO_3$ can still be calculated because this fractionation is constant at a given temperature (Clark & Fritz, 1997).

Then, short after the reaction releases the target CO_2, it passes along the first diffusion trap for water remotion and through the loop injection system which delivers CO_2 aliquots onto the gas chromatographic column to separate the molecular species. After passing the second diffusion trap for water remotion, the CO_2 species continue to the open split interface and into the IRMS (Fig. 8). If the signal of the first sample exceeds a pre-defined threshold of 5000 mV, a dilution step is performed in the open split before continuing to the ion source. In the IRMS, the stablished routine injects 5 reference gases, each with 10 pulses at the beginning, middle and end of the sample lectures to allow an accurate referencing of each sample aliquot to isotopic standards. Each sample instead produces 15 aliquots that are represented in 15 pulses, of which only the last 10 are used. To ensure statistical significance a minimum of 7 pulses were required to the calculations. Samples with less than 7 pulses were removed.

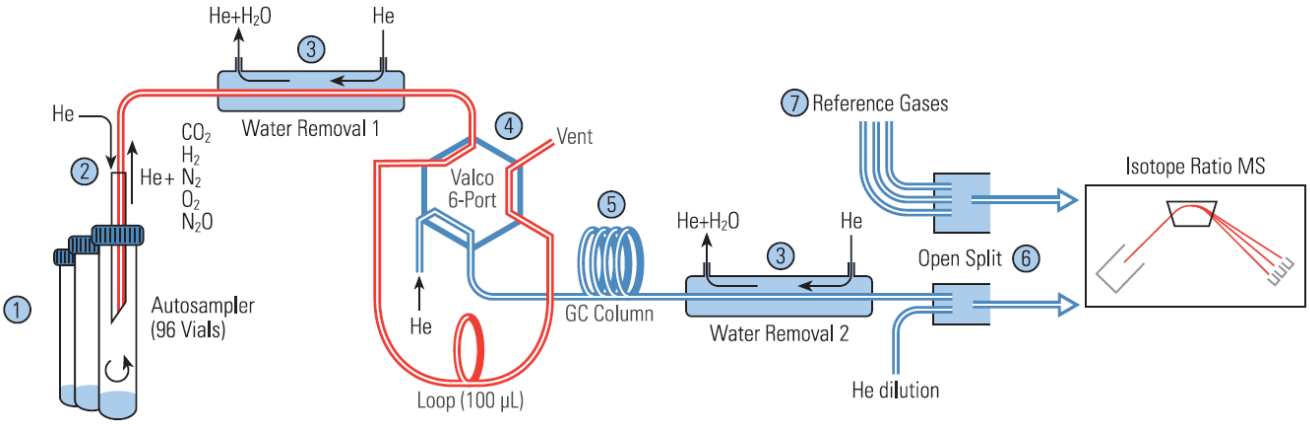

Fig. 8. Gas bench scheme consisting of a programable autosampler (1), a gas sampling system (2), a maintenance-dree water removal system (3), a loop injection system (4), an isothermal gas chromatograph (GC) (5), an open split (6), a reference gas injection system (7). Image taken from www.thermoscientific.com/irms.

4.4. Spectral Analysis of Time Series

Spectral analysis of a time-series transforms the original signal in the time domain into the sum of the different signals in the frequency domain. Higher spectral signals above random noise denote a distinct periodic phenomenon which can be reconstructed and associated to physical processes (Schulz & Mudelsee, 2002).

To that end we used the PAST software v.4.06 (Hammer et al., 2001) REDFIT spectral analysis module developed by Schulz & Mudelsee (2002), which shows the power spectrum above a red-noise background defined by the theoretical AR(1) and 0.01 and 0.05 significance levels ('white noise lines').

To assess transient oscillatory patterns we use the dplR library (Bunn, 2008) in R (R Core Team, 2022), which is an implementation of the wavelet transform developed by Torrence & Compo, (1998). This method is based on fast convolution of the signal under consideration with a mother wavelet at different scales, using the Fast Fourier transform FFT. Which produces "discrete blocks" of wavelet power that gives the most compact representation of the signal (Torrence & Compo, 1998). Here we employed the Morlet wavelet, consisting of a plane wave modulated by a Gaussian, that usually perform the best (Hammer et al., 2001). The significance of the power spectrum was tested against a red noise background spectrum with lag-1 coefficient of 0.9856, 0.9878, 0.9602 for VEAJ, the oldest portion of VECA and the portion between the hiatus, respectively (Hammer et al., 2001; Torrence & Compo, 1998). Estimated by ARMA analysis with a first order AR (autoregressive) process and MA (moving-average) values of 0 and 1, as specified in the PAST reference manual (Hammer et al., 2001).

4.5. Back-trajectories

To broadly assess the possible moisture pathways, we computed seven-day air parcel back-trajectories arriving at Alfredo Jahn (10.74 °N, 66.23 °W) and Caripe Cave sites (10.20 °N, 63.64 °W) with the HYSPLIT4 model (HYbrid Single-Parcel Lagrangian Integrated Trajectory) (Stein et al., 2015) with ERA Interim data (Hersbach et al., 2020) in native resolution (~80 km). Back-trajectories were initiated at 18 hours local time (23 UTC), at a height of 1000 m.a.g.l (~750 hPa), within the atmospheric layer where the most significant moisture transport to the study site takes place. Accounting for the numerical error during the computation, 280 and 850 back-trajectories were eliminated, resulting in 1911 and 1341 consistent back-trajectories between December October 2012 to December September 2018 from Alfredo Jahn and Caripe Cave, respectively.

To obtain the representative patterns the of the back-trajectories and assess their contribution to local precipitation at Alfredo Jahn and Caripe Caves, frequency and timing, we performed a cluster analysis (Fig. 13). We applied the hierarchical clustering analysis

(HCA) algorithm with Squared Euclidean distance from the HYSPLIT model. We clustered only the back-trajectories initiated on days when local precipitation was detected at the cave site. Local precipitation was estimated with precipitation data from the Global Precipitation Measurement Mission (GPM: Huffman et al., 2019) with spatial resolution of 0.25°, as the average of the nine grid cells centered at Alfredo Jahn and Caripe caves.

5. THE USE OF OXYGEN AND CARBON STABLE ISOTOPE RECORDS IN PALEOCLIMATIC RECONSTRUCTIONS

An isotope refers to a particular form of an element defined by a specific number of neutrons (Sharp, 2017). An element can have different isotopes, each with different mass numbers (defined by the sum of protons and neutrons in the atomic nucleus). And since the atomic number (protons in the nucleus) does not change among different isotopes neither should its chemical behavior. The different masses, instead, affect the bond strength resulting in different fractionation or partitioning, which is predictable at a given temperature (Clark & Fritz, 1997; Sharp, 2017). The isotopic fractionation between two substances (or phases of the same substance) A and B can be expressed by a constant α, which measure the ratio between the isotopic exchange (Eq. 2).

$$\alpha_{A-B} = \frac{R_A}{R_B} \qquad \textbf{Eq. 2}$$

Where *R* is the ratio of the two most abundant isotopes of a given element in the particular phase or substance. In the case of oxygen in the water molecule, the ratio of the abundance of heavy (^{18}O, with a terrestrial abundance of 0.204%) to light isotope (^{16}O, which represents the 99.796% of terrestrial oxygen) is expressed as ^{18}O /^{16}O. In the case of carbon the isotopic ratio is reported as ^{13}C /^{12}C, and ^{2}H /^{1}H for hydrogen isotope ratios (Clark & Fritz, 1997).

As an example, consider the change of phase of the water from liquid to vapor at 25°C:

$$H_2O \text{ (liquid)} \rightarrow H_2O \text{ (vapor) at } 25°C \qquad \textbf{Eq. 3}$$

The fractionation factor of liquid water to water vapor is expressed as follows:

$$\alpha_{liquid-vapor} = \frac{(^{18}O/^{16}O)_{liquid}}{(^{18}O/^{16}O)_{vapor}} = 1.00935 \qquad \textbf{Eq. 4}$$

Since, the energy required to break a bond is slightly higher for a heavy isotope than it is for a light one (Sharp, 2017), it is more likely that the stronger chemical bonds last longer than weaker ones. As observed in the previous example, the vapor phase retains the lighter isotopes, whose bonds in the water molecule are easier to break.

5.1. Delta Notation and Standards

However, rather than knowing the absolute isotopic ratios of two phases, we are mainly interested in comparing the variations in stable isotope concentrations of a given material to a known reference or standard. The produced data sets are comparable between isotope laboratories around the word by the use of recognized isotopes references in their routines.

Isotopic concentrations are then expressed as the difference between the measured ratios of the sample and standard over the measured ratio of the standard:

$$\delta^{18}O_{sample} = \frac{(^{18}O/^{16}O)_{sample} - (^{18}O/^{16}O)_{std}}{(^{18}O/^{16}O)_{std}} \quad \textbf{Eq. 5}$$

Generally, relative differences in isotopic ratios between samples and standards are small. So, they are reported in per mil (‰) by multiplying by 1000:

$$\delta^{18}O_{sample} = \left(\frac{(^{18}O/^{16}O)_{sample}}{(^{18}O/^{16}O)_{std}} - 1\right) \times 1000 \quad \textbf{Eq. 6}$$

Oxygen isotope compositions are expressed by using the symbol $\delta^{18}O$ and those of carbon by $\delta^{13}C$. A positive δ value means that the ratio of heavy to light isotope is higher in the sample than it is in the standard, and a negative δ value that the isotopic ratio is lower in the sample than in the standard (Sharp, 2017). In other words, a positive δ value (i.e. 10‰), signifies that the sample has 10‰ or 1% more ^{18}O than the reference. While a negative δ value has the opposite meaning, that is, less ^{18}O than the reference. (Clark & Fritz, 1997).

The Vienna Standard Mean Ocean Water (VSMOW), prepared from distilled seawater (United Nations International Atomic Energy Agency, IAEA) is the international accepted reference for ^{18}O and ^{2}H in waters and organic molecules. Whereas, the reference against which all $\delta^{13}C$ measurements and carbonate-$\delta^{18}O$ are reported is the analog of the fossil rostrum (internal calcite structure) of the cretaceous fossil mollusk *Belemnitella americana* from the Cretaceous Pee Dee Formation, designated as Vienna Pee Dee Belemnite (VPDB) (IAEA).

5.2. Equilibrium Isotopic Fractionation

Equilibrium in the isotope exchange between two phases is reached when the isotopic ratios stop changing with time. For the isotopes in the water molecules thus equilibrium fractionation occurs when the relative humidity is 100%. Low humidity and wind intensity effects during evaporation led to kinetic fractionation. Whereas, the condensation is a process in which equilibrium fractionation between vapor and water dominates. And is intimate related to the temperature, since when the vapor mass loses temperature and its capacity of retaining moisture, the water droplets become supersaturared and fall as rain. Temperature has also a direct effect on isotopic fractionation since it becomes greater at lower temperatures.

5.2.1. Rayleigh fractionation

Rayleigh isotopic fractionation is an important type of fractional distillation or condensation under equilibrium conditions. And describes the process by which vapor mass becomes progressively depleted in ^{18}O and ^{2}H as heavy isotopes are *distilled* in precipitation. Then, isotopically enriched rain or snow falls form an isotopically depleted vapor mass. Subsequent rains, while enriched with respect to the remaining vapor, will be depleted with respect to earlier rains from the same vapor mass (Clark & Fritz, 1997; Dansgaard, 1964), a process known as *amount effect*. As this vapor mass moves from its source area along a trajectory it will also experience successively Rayleigh distillation processes through rainout, a process known as *continental effect*. Elevated topography will make the vapor mass rise to lower pressures, from which it may cool and precipitate also following Rayleigh distillation giving to an *altitude effect* on isotopic fractionation. Seasonal temperature effects on isotopic fractionation can be disregarded in tropical regions.

5.3. Global Meteoric Water Line (GMWL)

Since mid-20th century, many studies on the isotopic composition of natural waters have either contributed with the isotopic data or properly recognized the existing correlation between $\delta^{18}O$ and $\delta^{2}H$ values of precipitation. And thus, the so-called Global Meteoric Water Line (GMWL) Craig, (1961) by computing the regression line of its long-term averages. Whose most precise equation (Eq.7) (Rozanski et al., 1993) uses the data of

219 stations produced by the Global Network of Isotopes in Precipitation (GNIP) established by the IAEA in collaboration with the World Meteorological Organization (WMO) as mentioned in Clark & Fritz, (1997).

$$\delta\ ^{2}H = 8.17(\pm 0.07)\ \delta^{18}O + 11.27(\pm 0.65)\ ‰\ \text{VSMOW} \qquad \textbf{Eq.7}$$

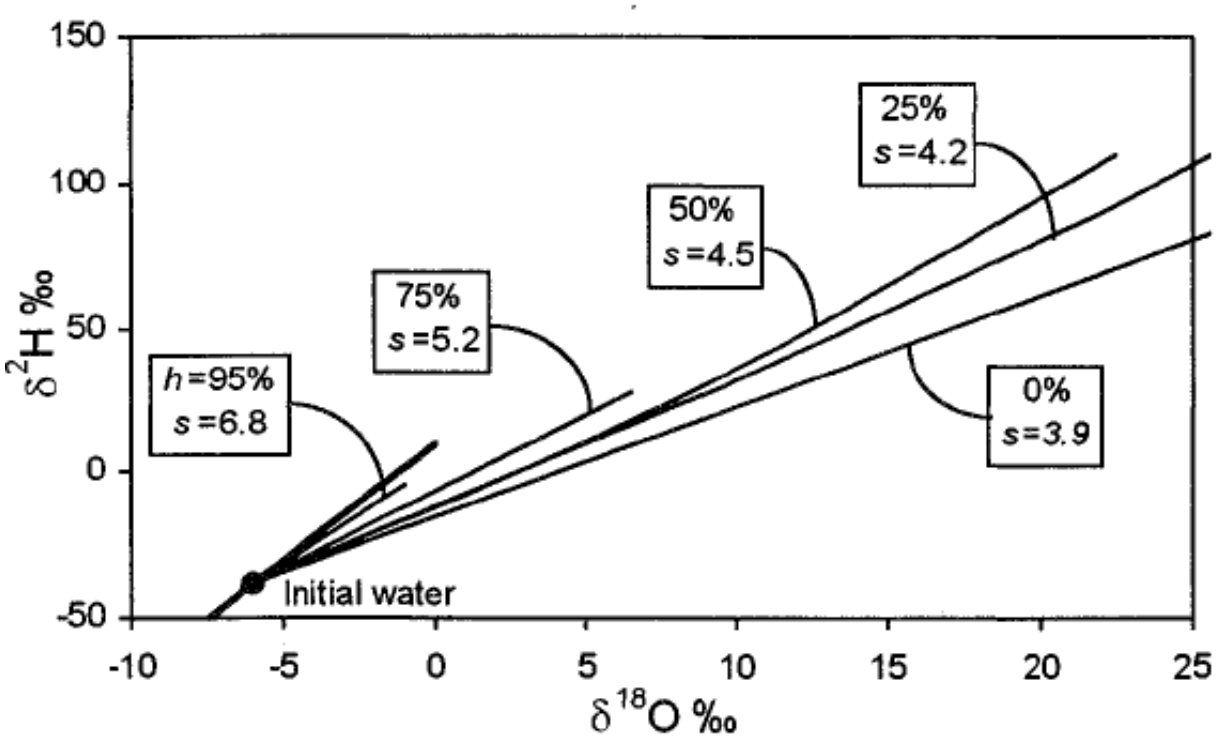

Fig. 9. $\delta^{18}O$ vs. $\delta\ ^{2}H$ plot. Lower slopes (s<8) depend on the relative humidity, h, deviating from the GMWL (heavy line). From Gonfiantini, (1986), taken from Clark & Fritz, (1997).

The GMWL is essentially the weighted average of Local Meteoric Water Lines (LMWL) which vary in slope and intercept according to local and regional meteorological conditions. The slope (s) strongly depends on humidity (h). When the relative humidity is below 100%, the kinetic fractionation during evaporation dominates and the precursor vapor mass becomes progressively enriched in ^{18}O and ^{2}H. Throwing the delta values of precipitation down the GMWL (Fig. 9). Vapor masses influenced by the evaporation of finite reservoirs such as lakes, rivers or flooded soils will also become progressively enriched in heavy isotopes.

5.3.1. Deuterium excess (d-excess) in meteoric waters

The intercept of the GMWL equation, is referred to the d-excess parameter (Dansgaard, 1964) and express the measure of the relative proportions of $\delta^{18}O$ and $\delta\,^{2}H$ contained in water (Fröhlich et al., 2002),. By rearranging the form of the Eq. 7 proposed by Craig, (1961), the d-excess is expressed as:

$$d - excess = \delta\,^{2}H - 8\,\delta^{18}O \qquad \textbf{Eq. 8}$$

The d-excess parameter in water precipitation might deviate from +10‰ mainly due to the kinetic effects of the evaporation in the oceanic source area, and mixture of air mases during the trajectory to the precipitation sites (Fig. 10) (Fröhlich et al., 2002). The combination of the effects of physical parameters such as relative humidity, air temperatures, SSTs and wind speed might play important roles in determining d-excess. In temperate regions, for example, the relative humidity appears to be far more important than the SSTs. Leading to higher d-excess under lower the relative humidity conditions (Pfahl & Sodemann, 2014).

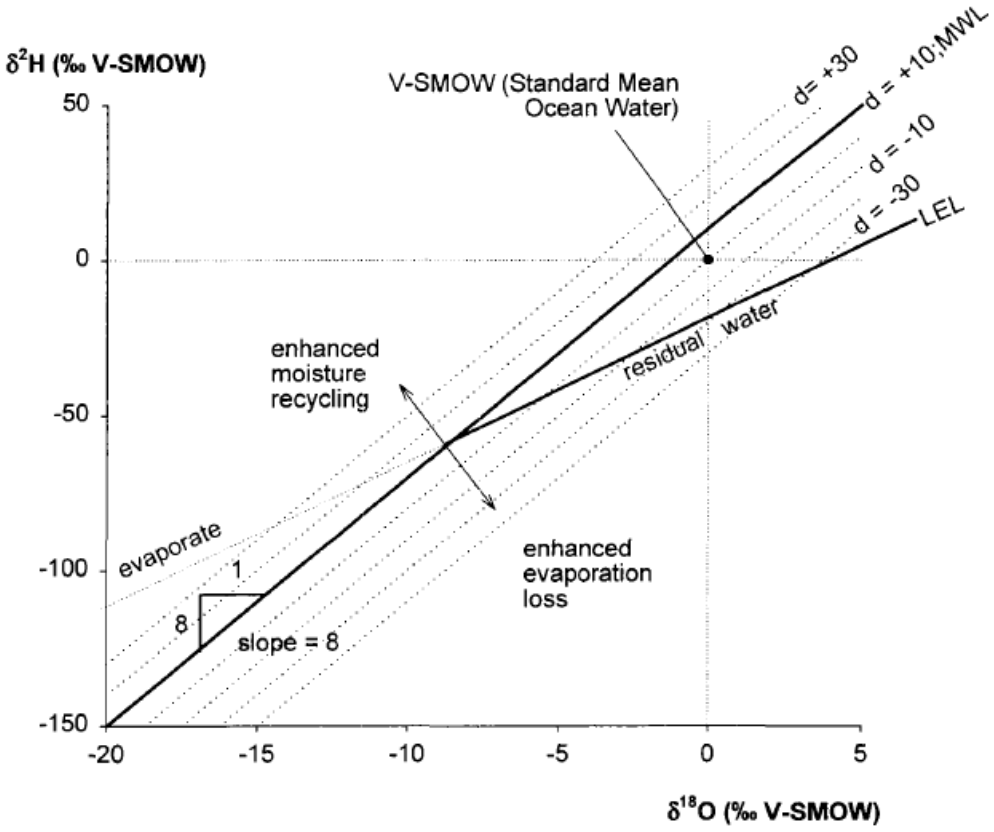

Fig. 10. Schematic plot showing the GMWL with slope=8 and d-excess d= +10‰, the local evaporation line of a finite volume of water (LEL) with slope<8 and the ocean water SMOW with d= -10‰. Relative changes in d-excess in precipitation might increase in response to enhanced moisture recycling or decrease in the case water is lost by evaporation. Figure taken from Fröhlich et al., (2002).

5.4. Main Processes Controlling $\delta^{18}O$ and $\delta^{13}C$ Values in Speleothems

The oxygen in speleothem calcium carbonate deposited under equilibrium conditions might mainly reflect the isotopic composition of the water molecules that fall as rain. However, it may significantly differ from its original isotopic signature due to changes along percolation down through multiple pathways in the karstic system. Whereas, the sources of carbon in speleothem $CaCO_3$ can vary between ^{13}C-depleted organic CO_2, and ^{13}C-enriched inorganic carbon from the carbonate bedrock (McDermott, 2004; Novello et al., 2021; Utida et al., 2020). Understanding the controls of equilibrium and kinetic fractionation for properly interpretation of speleothem $\delta^{18}O$ and $\delta^{13}C$ values is imperative for paleoclimatic and paleoenvironmental studies (Fairchild et al., 2006; Lachniet, 2009). The process of speleothem formation begins above the epikarst when water from rain reacts with the CO_2 present in the soil to form carbonic acid (Eq. 9). The CO_2 in the soil is biogenic derived from the plant's roots respiration and organic matter (OM) decomposition among other processes.

$$H_2O + CO_2 \rightarrow H_2CO_3 \qquad \textbf{Eq. 9}$$

The carbonic acid in contact with the carbonate bedrock along its percolation through the conduits and fractures dissolves the calcium and bicarbonate ions into the solution (Eq. 10).

$$CaCO_3 + H_2CO_3 \rightarrow Ca^{2+} + 2HCO_3^- \qquad \textbf{Eq. 10}$$

Then, speleothem precipitation occurs when the drip water becomes supersaturated by degassing of CO_2 by diffusion into the cave atmosphere with relatively low pCO_2. (Eq. 11).

$$Ca^{2+} + 2HCO_3^- \rightarrow CaCO_3 + H_2O + CO_2 \qquad \textbf{Eq. 11}$$

During the infiltration into the soil, the surface water can suffer ^{18}O-enrichment by evaporation. The enrichment will depend on the humidity in the soil pores, the volume of water evaporated and thus the extent of the dry season (Fairchild et al., 2006; Lachniet, 2009). Which should be followed by a rapid increase in precipitation in order to transport the waters with the $\delta^{18}O$ enriched signal to the cave dripping solution (Fairchild et al., 2006).

5.4.1. The role of soil and vegetation type on $\delta^{13}C$ values of speleothems

The presence of dense forests can reduce evaporation by keeping soil moisture, thus contributing to conserve the rain $\delta^{18}O$-isotopic signature. On the other hand, plant transpiration can reduce the water volume in the soils but this won't cause any fractionation in the oxygen isotopes (Gat, 1996).

Two-end-member model for analyzing the proportional contribution of soil and host-rock to the $\delta^{13}C$ carbon isotopic composition fingerprint in speleothems have been proposed. In an open system the soil CO_2 reservoir is infinite and remains in equilibrium with the percolating waters, thus the $\delta^{13}C$ holds the isotopic signature of the soil above the epikarst and the isotopic signature of the bedrock can be neglected. In a closed system, the solution loses contact with the soil reservoir as soon as carbonate dissolution commences and the initial amount of CO_2 is rapidly consumed, leading to a major contribution of the host-rock to the $\delta^{13}C$ signal in the solution (McDermott, 2004).

The nature of the dominant photosynthetic pathway of the vegetation above the epikarst may also determine the $\delta^{13}C$ values of the soil reservoir. Which as listed by Novello et al., (2021) is conditioned by climatic parameters such as temperature, pluviosity, rainfall seasonality and atmospheric CO_2. Plants are distinguished as C_3, C_4 and CAM based on whether the first product of CO_2 fixation is a 3- or 4- carbon molecule. C_3 plants are best fitted to humid conditions and/or high concentration of CO_2 and have $\delta^{13}C$ ranges between -32‰ and -20‰ (VPDB), that can vary depending of the water availability. C_4 include tropical grasses favored over the C_3 plants during dry-warmer seasons and climates, and lower concentrations of atmospheric CO_2. C_4 plants have a narrower range of carbon isotopic composition between -17‰ and -9‰ (VPDB). CAM plants include some water-storing plants (called succulents), even better adapted to dry-warmer climates than C_4 plants and have $\delta^{13}C$ values that overlap with both C_3 and C_4 plants. Those $\delta^{13}C$ values

of the soil reservoir under certain dominant vegetation are transferred do the carbon isotopic values of the stalagmites. Typically, vegetation above the epikarst dominated by C_3 and C_4 plants conduce to lower and higher $\delta^{13}C$ speleothem values ranging between -14‰ to -6‰ and -6‰ to -2‰, respectively (Novello et al., 2021).

5.4.2. Prior Calcite Precipitation (PCP)

The CO_2 degassing from the solution into the cave atmosphere and air pockets within fissures can lead to fractionation of the $\delta^{13}C$ from the dissolved inorganic carbon (DIC) influencing the $\delta^{13}C$ value recorded in the stalagmites. During dry periods, the volume of air pockets along the flow path may increment. As also may increase the exposure time of the seepage due to a reduction in the dripping rate, leading to enhanced diffusion of CO_2. As the lighter carbon isotope ^{12}C is preferentially removed from the solution, the $\delta^{13}C$ of the precipitated carbon during dry periods will be higher. During wet periods instead, air pockets are likely to be reduced and thus the $\delta^{13}C$ fractionation by the prior calcite precipitation.

It has been proposed that the rapid loss of CO_2 could led to kinetic fractionation between dissolved carbonate phases and solid $CaCO_3$, masking the paleoclimatic information of both oxygen and carbon isotope values in the stalagmites (Hendy, 1971). Positive correlation between $\delta^{18}O$ and $\delta^{13}C$ values along the growth axis are thought to be indicative of kinetic fractionation processes. However, this has been extensively debated since covariation between $\delta^{18}O$ and $\delta^{13}C$ can happen under isotopic equilibrium conditions as a response to a first order climatic control (Dorale & Liu, 2009; Lachniet, 2009).

6. BASIS FOR INTERPRETING $\delta^{18}O$ IN VENEZUELAN SPELEOTHEM RECORDS

6.1. Maracay LMWL and d-excess

Maracay GNIP is the closest isotopic rainfall monitoring station to Alfredo Jahn and Caripe caves, and Birongo and Caripe INAMEH stations. When plotted in $\delta^{18}O$ and $\delta^{2}H$ space, various data falls below the GMWL (Fig. 11) showing a LMWL with slope s = 5.35. This means that kinetic fractionation has an important role during evaporation. Possibly related to low relative humidity close to 0.75 (Gat, 1971). However, since Maracay GNIP station is located near the Lake Valencia (Fig.1), isotopic enrichment of this finite reservoir through evaporation could also contribute to heavier values in precipitation, thus deviating from the s~8 of the GMWL. The possible factors related to kinetic fractionation during evaporation are evaluated in Fig.12 by comparing calculated weighted d-excess from monthly $\delta^{18}O$ and $\delta^{2}H$ values (Eq. 8) to evaporation at the side of Lake Valencia (Fig. 12a) and other physical parameters measured at the Maracay GNIP station (Fig. 12b).

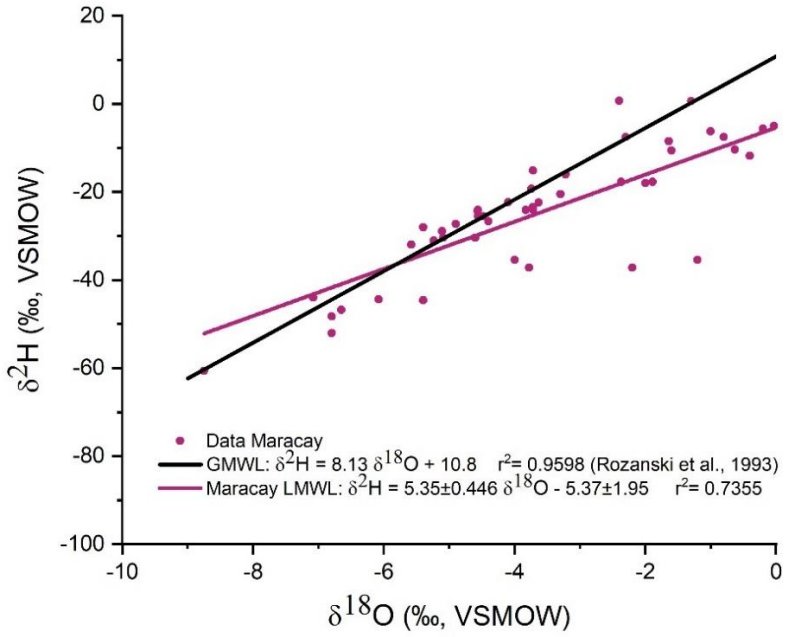

Fig. 11. LMWL for Maracay GNIP $\delta^{18}O$ and $\delta^{2}H$ isotopes in precipitation collected monthly over a scattered period between 1961 and 1975. A total pair of 48 isotope values were plotted and used to calculate the LWML of Maracay: $\delta^{2}H = (5.35 \pm 0.446)\ \delta^{18}O - (5.37 \pm 1.95)$. The equation of the GMWL corresponds to the one calculated by Rozanski et al., (1993).

The deuterium excess (d-excess) was first calculated for individual months using equation 8. Then, the weighted values d-excess values ($\bar{d}_w$) for each month were obtain following the formula in equation 12.

$$\bar{d}_w = \frac{\sum_{i=1}^{n} d_i * p_i}{\sum_{i=1}^{n} p_i} \qquad \textbf{Eq. 12}$$

Where d_i and p_i are the d-excess and precipitation amount (mm), respectively, and n is the number of data having the three: $\delta^{18}O$, $\delta^{2}H$ and precipitation values for the specific month. Because the three values were needed for the calculation, it was only possible to calculate the weighted values for April (2), June (2), July (5) and November (2) with the n reported between the parenthesis. Thus, the computed weighted d-excess values are not conclusive and since its high analytical uncertainty can be relatively high in comparison with its natural variability (Fröhlich et al., 2002), caution should be taken in the interpretation of this parameter. However, comparisons with the monthly averaged precipitation at the side of Lake Valencia barely suggest a possible correlation between high evaporation during April and negative weighted d-excess. Whereas, positive d-excess during the wet and warm months of June and July could be indicative of prevailing conditions close to the global average (+10‰). The contrasting negative values of April and November possibly reflects sub-cloud raindrop re-evaporation due to drier conditions in the NH source regions and along its path to Venezuela (see back trajectories Fig.13). Though, more isotopic data of rainfall are needed to validate these preliminary observations.

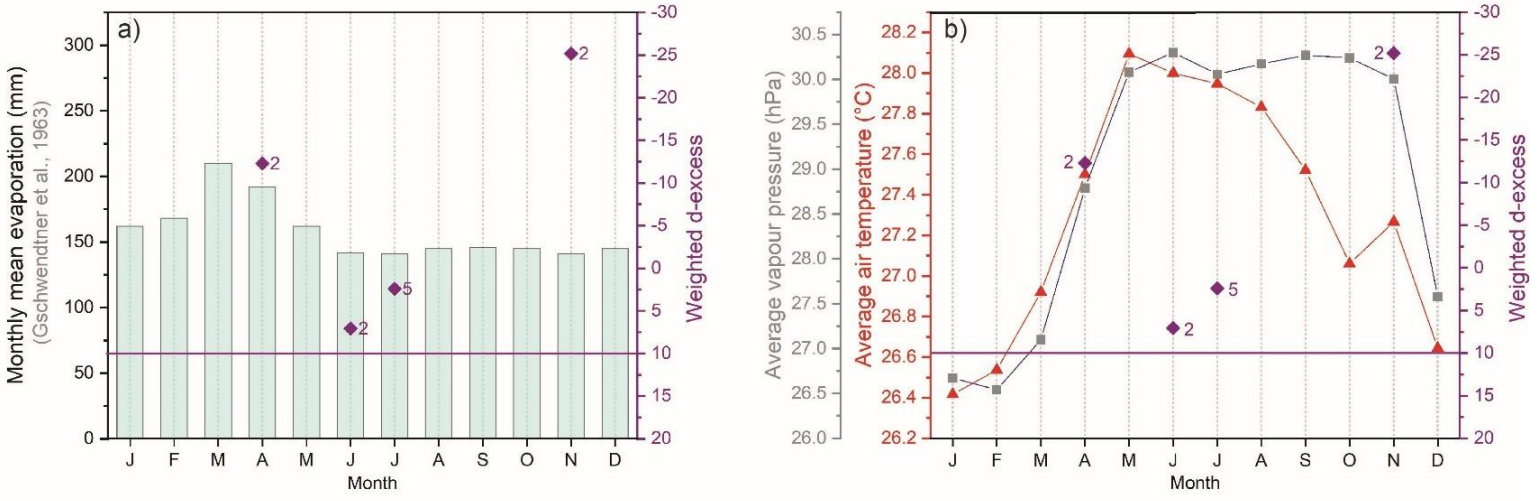

Fig. 12. Comparisons between weighted d-excess (purple diamonds) and a) monthly mean evaporation at the lake Valencia side (mm, light blue bars) (Gschwendtner, 1963). b) Average air temperature (°C, red triangles) and average vapour pressure (hPa, gray squares). Purple line in 10 represents the d-excess of the GMWL.

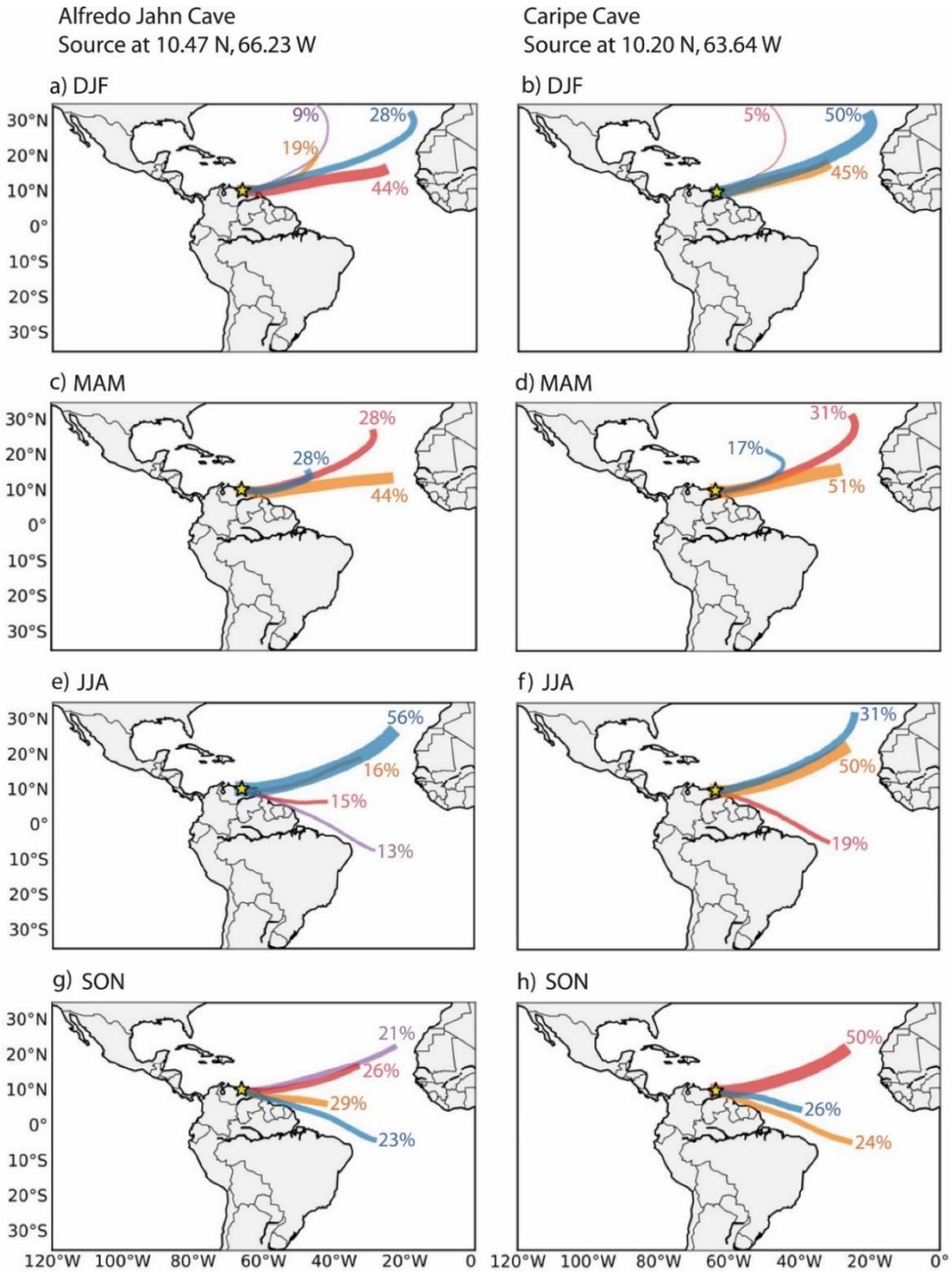

Fig. 13. Seven-day back-trajectories starting at 10.74 °N, 66.23 °W (Alfredo Jahn, left panels) and 10.20 °N, 63.64 °W (Caripe Cave, right panels), 1000 m above ground level

(~750 hpa), from 2012 to 2018. The colors show the average path and the percentage of back-1911 trajectories for Alfredo Jahn and 850 for Caripe, for each cluster for **a, b)** December-January-February; **c, d)** March-April-May; **e, f)** June-July-August and **g, h)** September-October-November.

6.2. $\delta^{18}O$ As a Regional Proxy of Precipitation

As previously suggested, Maracay GNIP $\delta^{18}O$ values in precipitation also differ between the dry and wet seasons. Indeed, heavy $\delta^{18}O$ values between 0.5 and -0.5‰ are observed during January and March. From were a ~2.5‰ depletion occurs in April, variating between -2.5 to -4.5‰ range in the subsequent months (Fig. 14). Unfortunately, due to the low number of data, correlations between precipitation totals and weighted-$\delta^{18}O$ values although negative, are found to be non-significant (p-value<0.05) at monthly and annual scales for Birongo (-0.54, p-value= 0.0878), Caripe (-0.22, p-value=0.4935) and Maracay (-0.42, p-value= 0.1759). Still the *amount effect* might be the main control of isotope values in precipitation in northeastern Venezuela as has been widely suggested for tropical regions (Dansgaard, 1964; Fairchild et al., 2006; Rozanski et al., 1993; Vuille et al., 2003).

The *amount effect* can be in great part explained by the partial evaporation of light rains in the source areas during the dry months from January to March leading to heavier $\delta^{18}O$ isotopic values. And to ^{18}O-depleted rainfall by the successively Rayleigh distillation of water vapor within intense high-troposphere low pressure systems occurring during the wet season from April to December (Fig.14). And in particular during May to August, when

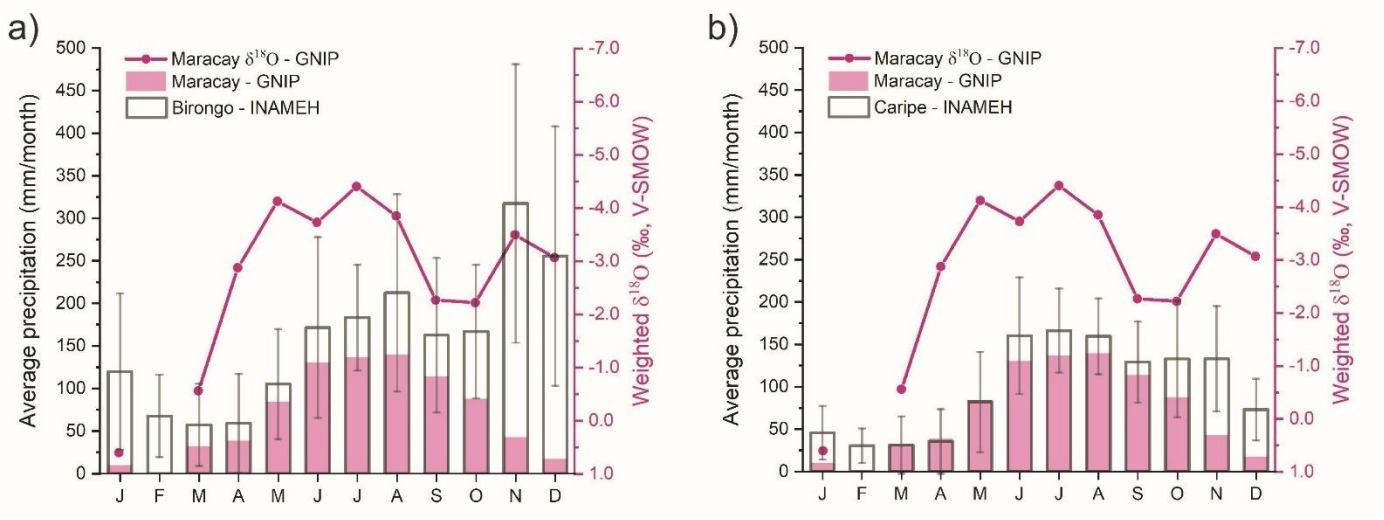

Fig. 14. Monthly mean precipitation for GNIP, INAMEH and IDEAM meteorological stations located close to the cave sites a) Alfredo Jahn Cave: Maracay and Birongo. b) Caripe Cave: Maracay and Caripe. Weighted $\delta^{18}O$ oxygen isotope ratios for Maracay (1961-1975) were calculated from GNIP IAEA/WMO database (IAEA/WMO, 2021). Birongo (1951-1954, 1960-1999), Caripe (1960-2007) data are from INAMEH (Instituto Nacional de Meteorología e Hidrología, Venezuela). Note that scale for right-side y-axis ($\delta^{18}O$) is inverted in the two panels.

the most depleted $\delta^{18}O$ isotopic values are observed (Fig.14) as the ITCZ-related convective activity migrates to a progressively more northern position over Venezuela (Fig.3). During September and October, when the ITCZ has reached its northernmost position over the central lesser Antilles (Martinez et al., 2019), $\delta^{18}O$ values become slightly more enriched, before again becoming slightly more negative in November (Fig.15), once the ITCZ migrates southward.Relatively heavier $\delta^{18}O$ values in November- December than those observed during May to August might be related to decreased convection due to cooler temperatures in the NH source areas (Fig.13). And/or to the income of local moisture sources with a heavier isotopic signal.

As explain in section *3.2.2*, the regional variability in precipitation might be governed by the particular geographic setting and exposure to the moisture carrying winds. Whereas, isotopic composition imprint on rainfall represents more regional mechanisms. Based on the visual match with the available $\delta^{18}O$ data from Maracay GNIP station, both Birongo and Caripe closest stations to the cave sites seems to be sensitive to rainfall amount (Fig.14). However, more data are needed for further supporting these observations and the possible influence of local sources of moisture during the last months of the year.

The ability of the $\delta^{18}O$ oxygen isotopes in tracking the meridional migration of the ITCZ in near coastal stations and islands along the eastern border of SA is tested by analyzing the monthly weighted values of the next GNIP station further north, the Seawell Airport station in Barbados (13°N) (Fig. 15). Coherently, to the 1.5‰ relatively enrichment in the $\delta^{18}O$ values of Maracay during September-October, the Seawell Airport values get relatively depleted by 1.5‰ during the same period. In consistence with a northward position of the ITCZ overt the central Lesser Antilles (Martinez et al., 2019).

In order to test possible influence of the ENSO in the annual variability we performed an additional correlation of the annual data. This time, between the weighted $\delta^{18}O$ from July of one year to June of the following year and its corresponding precipitation annual totals. And found also a non-significant, slightly less negative correlation than with the conventional calendar-year data (-0.32, p-value= 0.3441).

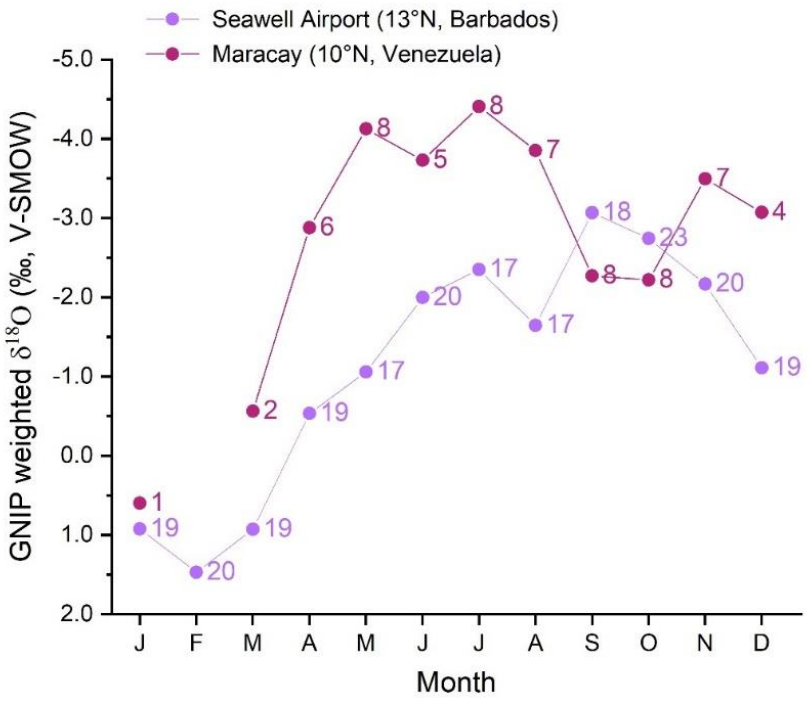

Fig. 15. Monthly weighted mean of $\delta^{18}O$ oxygen isotope ratios for Maracay (1961-1975 (pink) and Seawell (1961-1990) (light purple) GNIP stations (IAEA/WMO, 2021), showing the number of data used in its calculation.

7. RESULTS

7.1. Age-depth Chronologies

Age model chronologies for speleothem samples were constructed using StalAge algorithm developed by Scholz & Hoffmann (2011). Several age reversals along stalagmite VEAJ were noted (Fig. 16). Some of them were detected as outliers and removed from the age models by using Bayesian statistics. While for other age inversions, an iterative procedure was applied to increase the range of uncertainty in order to fulfil the monotonicity criterion (Fig. 16a-c) (Scholz & Hoffmann, 2011). Also, for sample VECA some outliers were detected and removed, while for other age reversals, the error was enlarged (Fig. 16d). Most of the dating analyses conducted in the bottom part of VECA, next to the altered portion did not show age inversions, further supporting the visual characterization of the unaltered layers (Fig. 7). In the case of VECA, the few removed dates were older than expected (Fig. 16d), which is probably caused by diagenic alteration that preferentially leachates the U relative to Th isotopes as described by Dorale et al., (2004) and Scholz et al., (2012). In comparison, the vast majority of the removed ages in the VEAJ samples were younger than expected, which probably associated to the incorporation of non-carbonate constituents with high detrital ^{230}Th (Fig. 16a-c).

According the age model, the base portion of the Alfredo Jahn Cave speleothem (VEAJ-base) grew continuously between 8500 and 6800 yrs BP (Fig. 16c). While the -top left portion partially covered the period between 6710 and 4480 yrs BP, with two hiatuses between 6110-5015 and 4480-4100 yrs BP (Fig. 16a). VEAJ-top right, grew continuously between 6780 and 3430 yrs BP (Fig. 16b). The sample VECA from the higher elevation Caripe Cave complements this record from Venezuela by covering the last 2250 years, except for two hiatuses between 230-510 and 1075-1210 CE and the absence of deposition between 1530 CE to the present (Fig. 16d).

7.2. VEAJ-top Composite

$\delta^{18}O$ and $\delta^{13}C$ time-series were based on StalAge models (Scholz & Hoffmann, 2011) constructed for all the stalagmite samples. Since VEAJ-top left overlaps some sections of the -top right record (Fig. 18), we merge them by using a statistical procedure. For the oldest segment we conducted a cross-correlation analysis and found the greatest positive

correlation occurring when the -top left record lags by 160 years (r= 0.36, p-value< 0.05) (Fig. 17). After adding 160 years to the dates of the oldest top left segment, the isotopic series were linearly interpolated to produce evenly spaced data. Then were merged through normalization and averaging of both series as explained in Della Libera et al., (2022). For the youngest segment, the good visual match between the series (Fig. 18), no needed cross-correlation analysis. Permil values for the merged segments were reconstructed from mean and standard deviation values of the longer VEAJ-right time serie (Fig. 19). The record composed of the merged segments and the remaining -top right record is referred here after as VEAJ-top composite.

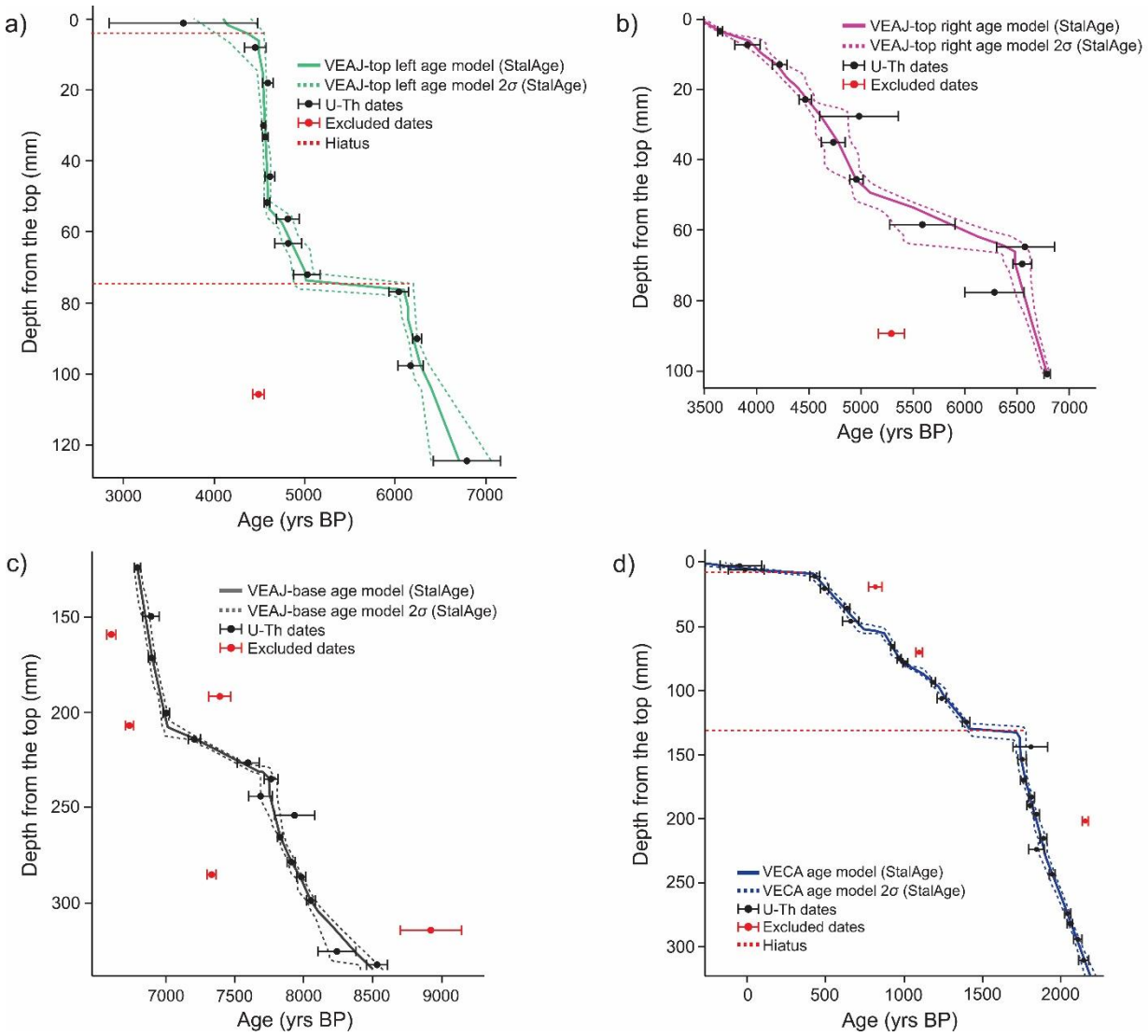

Fig. 16. StalAge (Scholz & Hoffmann, 2011) age-depth models for Alfredo Jahn Cave speleothem three main axes: **a)** VEAJ-top left (green line), **b)** VEAJ-base (dark gray line) and **c)** VEAJ- top right (pink line). **d)** Age-depth model for Caripe Cave speleothem VECA. Dashed lines for color related with each sample represent age-model associated 95% confidence interval. Circles and error bars represent U-Th dates. Red circles are outliers discarded in the age model. Red dashed lines are the identified hiatus.

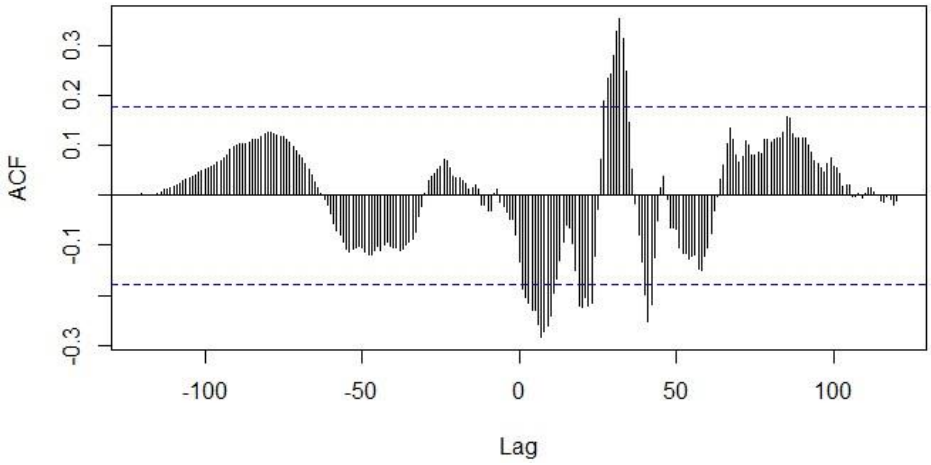

Fig. 17. Cross correlation analysis for the overlapped oldest VEAJ-top left segments and the VEAJ-top right record. The greatest positive correlation occurs when the -top left lags by 160 years (32 x 5 years of temporal spacing) the -top right record (cor= 0.36, p-value= 0.0001).

7.3. $\delta^{18}O$ and $\delta^{13}C$ records and wavelet analyses

7.3.1. Alfredo Jahn cave (VEAJ-base & -top composite)

The base portion of the Alfredo Jahn Cave speleothem (VEAJ-base) has $\delta^{18}O$ values ranging between -2.5 and -4.4‰ (average= -3.5‰) (Fig. 19a). Whereas, the top composite (VEAJ-top composite) has a slightly wider range between -2.5 and 4.6‰ (average= -3.6‰) (Fig. 19a). Spectral analysis of $\delta^{18}O$ in VEAJ-base & top composite record indicates significant periodicities at 95% level centered on 506, 48, 18 and 13 years (Fig. 20). Starting from one of the lowest values of the record at 8.5 ka BP (-4.4‰), an abrupt enrichment of ~1.5‰ occurs within a century until 8.2 ka, follow by a progressive lowering between 8.3 and 7.0 ka, just interrupted by two higher anomalies between 7.65-

7.60 (-2.6‰) and 7.3-7.24 ka (-3.0‰) (Fig. 19a). Between 6.9 and 6.4 ka BP abrupt changes >1‰ occur in less than 150 yrs. Followed by apparent shorter periods (6.4-6.0 and 5.2-4.5 ka) trending toward depleted values, and larger periods (6.0-5.2 and 4.5-3.6 ka) of progressive enrichment (Fig. 19a).

$\delta^{13}C$ record, ranging between -6.3 and -11.8‰, is quite similar to the $\delta^{18}O$ (Fig. 19b) as confirmed by the positive correlation observed in VEAJ-base (r= 0.57, p-value<0.1) and VEAJ-top composite (r= 0.63, p-value<0.1). As so, growth rates roughly followed both $\delta^{13}C$ and $\delta^{18}O$ isotopes, increasing (decreasing) during periods characterized by lower (higher) values (Fig. 19c). Notable, growth rates were higher in the base stalagmite (up to 0.5 mm/yr) than in the top composite (up to 0.08 mm/yr) (Fig. 19c), providing mean temporal stable isotopes sampling resolutions of 3 and 23 yrs, respectively.

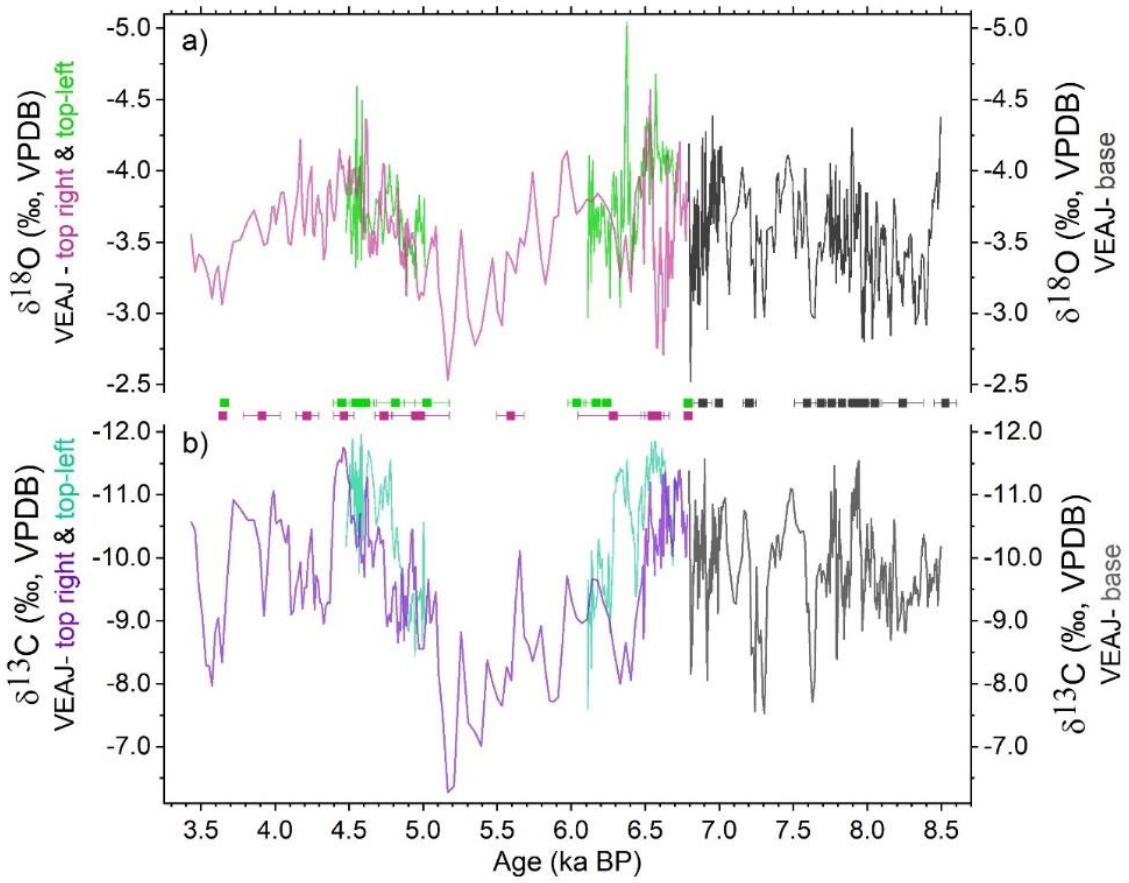

Fig. 18. a) $\delta^{18}O$ and **b)** $\delta^{13}C$ isotopic profiles and U-Th dates of VEAJ major three growth axes: VEAJ-base, VEAJ-top left, and VEAJ-top right. Note the different scales on y-axis. Also note the scale for all $\delta^{18}O$ and $\delta^{13}C$ y-axes is inverted.

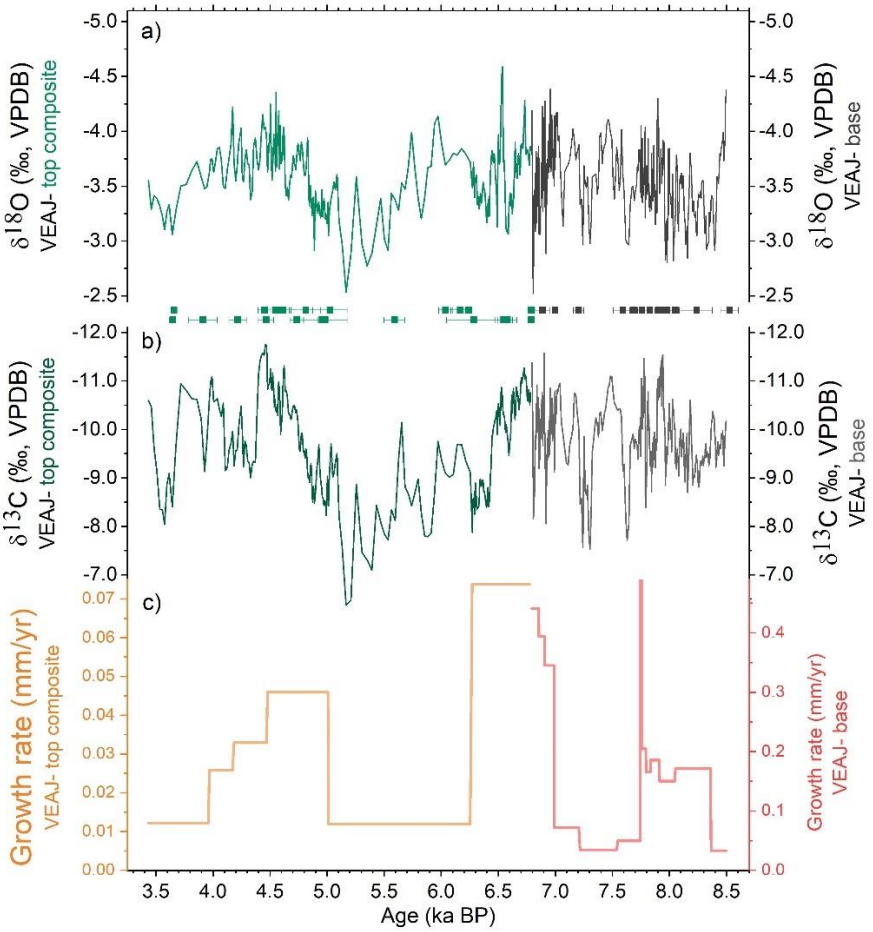

Fig. 19. a) $\delta^{18}O$ and **b)** $\delta^{13}C$ isotopic profiles and U-Th dates of VEAJ-top composite (green) and VEAJ-base (gray). **c)** Growth rates (mm/yr) of VEAJ-base (red) and VEAJ-top composite (orange). Note the different scales on y-axis. Also note the scale for all $\delta^{18}O$ and $\delta^{13}C$ y-axes is inverted.

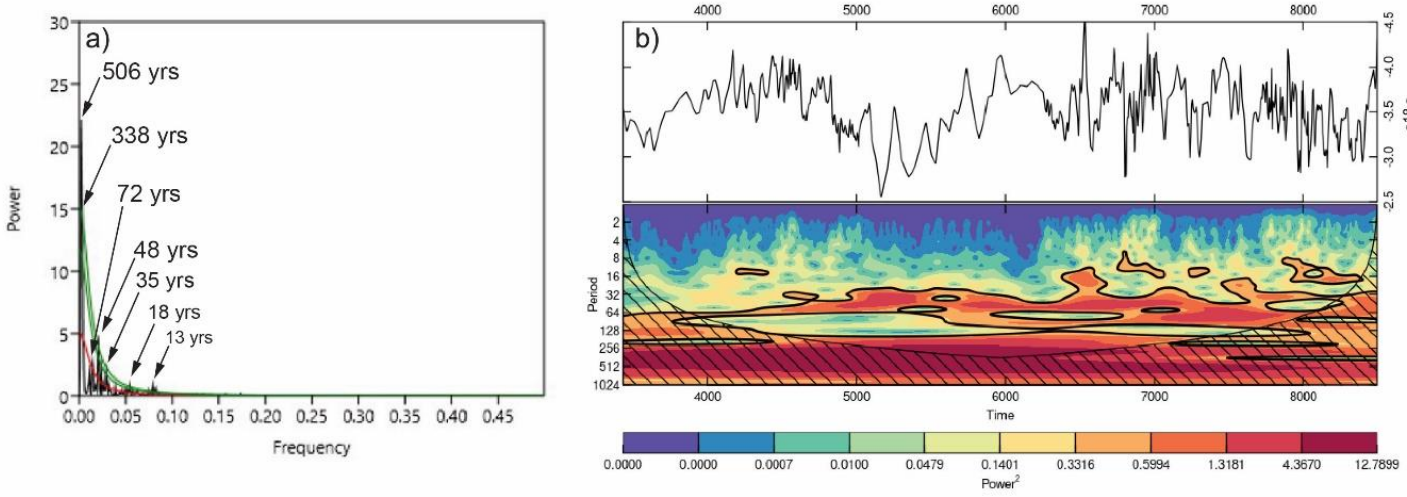

Fig. 20. Spectral analysis of VEAJ-base & -top composite $\delta^{18}O$ record: a) REDFIT showing significant periodicities. Green lines represent the confidence interval calculated for 90% and 95%. Red line shows the AR(1) red-noise model (Schulz & Mudelsee, 2002). b) Wavelet power spectrum using Morlet wave function. The color index indicates the energy of the periodicities in the time series. Black contours denote regions with 95% significance level (Torrence & Compo, 1998).

7.3.2. Caripe cave (VECA)

Caripe Cave sample (VECA) shows a more depleted and wider $\delta^{18}O$ isotopic range than VEAJ, between -2.5 to -5.3‰ (average=3.9‰) (Fig. 21a). A remarkable 41-yrs periodicity within 95% statistical confidence is present along the oldest segment (Fig. 22). Oscillations in the older segment of VECA mostly occur around the mean, however, higher amplitude excursions of lower-higher-lower are observed between 80 BCE and 120 CE. After the first hiatus, a period of lower $\delta^{18}O$ values is observed between 500 CE and the 700 CE (-4.7‰). Followed by an important enrichment of ~1.5‰ which last until the beginning of the MCA at 900 CE. (Fig. 21a). The MCA (900 to 1100 CE) is characterized by a relative depletion in $\delta^{18}O$ values (-3.8‰), including two notable enrichments centered at 940 (-3.3‰) and 1010 CE (-3.0‰). Spectral analysis of the segment between the hiatus indicates periodicities centered on 70, 12 and 9 years, within 95% statistical confidence (Fig. 23). The youngest segment of the record is too short for conducting spectral analysis. However, it shows an important enrichment of ~1.0‰, during transitional period between the MCA and the LIA. Getting depleted again around 1375 CE until the end of the record, 115 years after the start of the LIA at 1400 CE (-4.5‰) (Fig. 21a). $\delta^{13}C$ is positive correlated to $\delta^{18}O$ record ($r= 0.56$, p-value<0.05), perhaps only excepting the period after the MCA when an important trend toward higher values occurs until 1400 CE when it gets slightly depleted but still dominated by a heavier $\delta^{13}C$ signature (Fig. 21b), which contrast the significant depletion of the $\delta^{18}O$ values observed during the oldest portion of the LIA documented in our speleothem record. Growth rates were higher for the oldest portion of the stalagmite which led a resolution of ~1.5 yrs, while the other two segments had an average resolution of ~4 yrs (Fig. 21c).

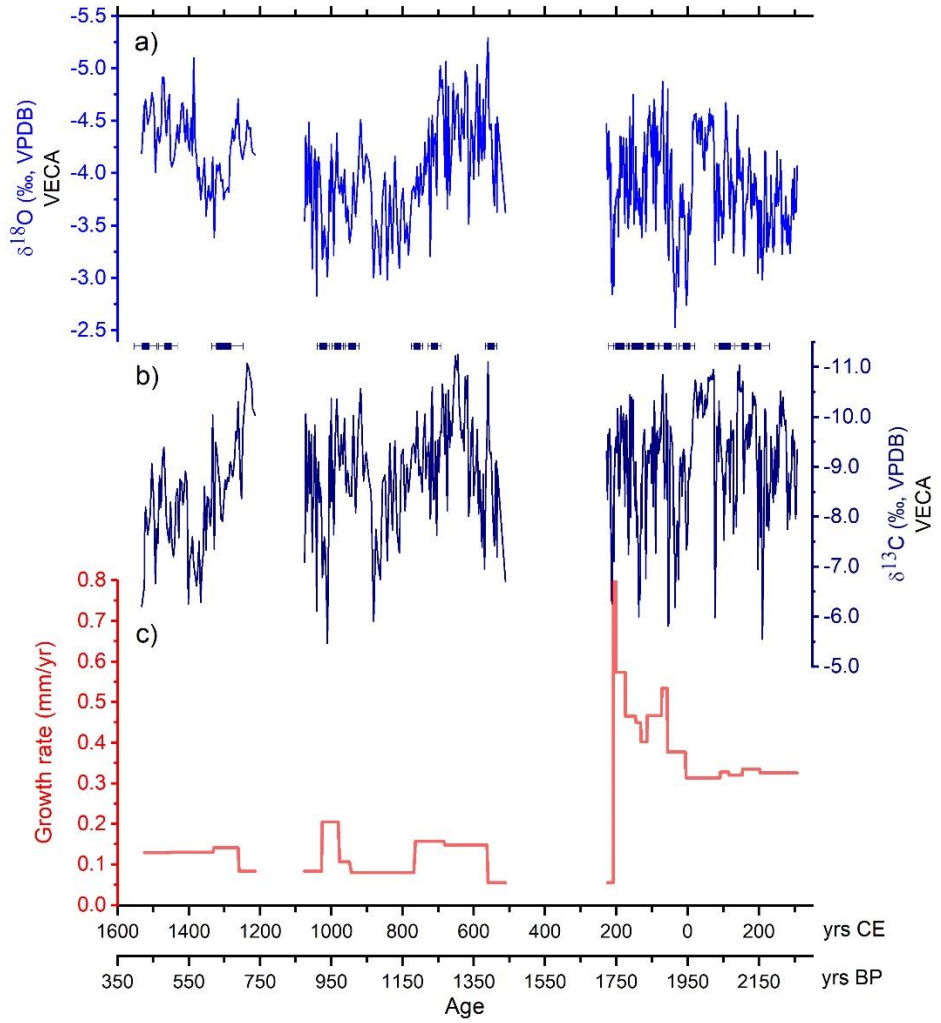

Fig. 21. a) $\delta^{18}O$ (navy blue, upper curve) and **b)** $\delta^{13}C$ (dark blue, lower curve) isotopic profiles of Caripe Cave VECA sample with U-Th dates and associated error bars. **c)** Growth rates in mm/yr.

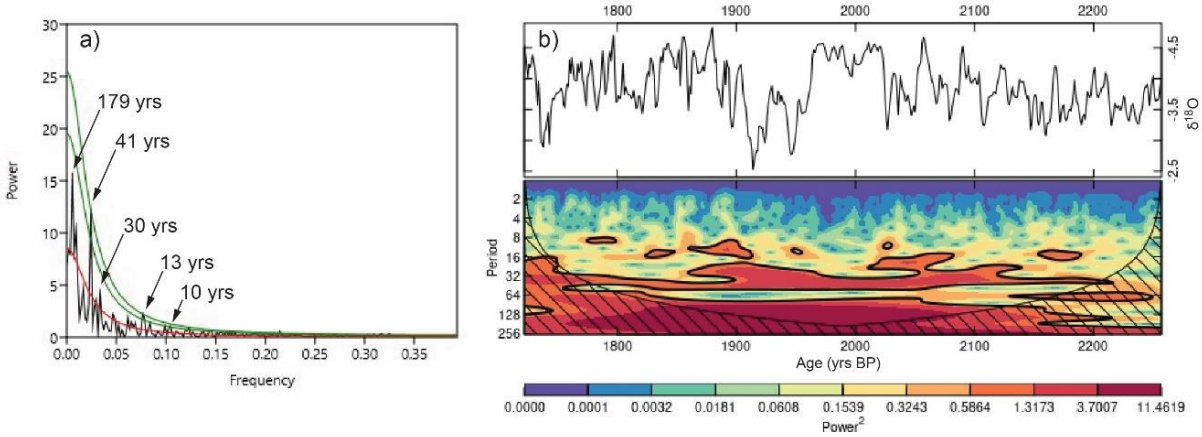

Fig. 22. Spectral analysis for the oldest segment of VECA $\delta^{18}O$ record: a) REDFIT graphic showing significant periodicities. Green lines represent the confidence interval calculated for 90% and 95%. Red line shows the AR(1) red-noise model (Schulz & Mudelsee, 2002). b) wavelet power spectrum using Morlet wave function. The color index indicates the energy of the periodicities in the time series. Black contours denote regions with 95% significance level (Torrence & Compo, 1998).

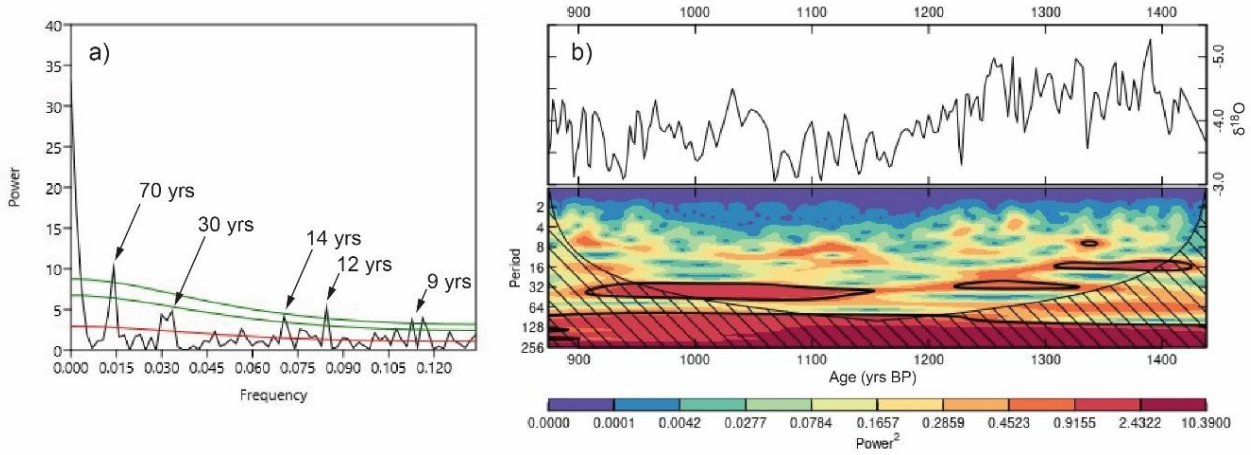

Fig. 23. Spectral analysis of VECA $\delta^{18}O$ record between 510-1075 CE: a) REDFIT graphic showing significant periodicities. Green lines represent the confidence interval calculated for 90 and 95%. Red line shows the AR(1) red-noise model (Schulz & Mudelsee, 2002). b) wavelet power spectrum using Morlet wave function. The color index indicates the energy of the periodicities in the time series. Black contours denote regions with 95% significance level (Torrence & Compo, 1998).

8. DISCUSSION

8.1. Cariaco Basin and Teleconnections to Higher Northern Latitudes

Our mid Holocene Venezuelan VEAJ record shows a striking resemblance to the molybdenum concentrations (Mo, cps) in sediments from the CB (Gibson & Peterson, 2014) (Fig. 24b). Lower (higher) speleothem $\delta^{18}O$ and $\delta^{13}C$ values coincide with increased (decreased) Mo amounts in CB sediments. Mo is thought to be a proxy for bottom water ventilation and therefore it may also be related to the oxygen balance in water masses (Gibson & Peterson, 2014; Yarincik et al., 2000). As Mo does not accumulate under oxygenic conditions, a greater concentration of this element is interpreted as a major level of anoxia in the sediments (Gibson & Peterson, 2014; Yarincik et al., 2000). Furthermore, Mo removal to the sediments in anoxic marine systems depends on the concentration of organic matter (OM) (Algeo & Rowe, 2012; Sweere et al., 2016). This suggest that increased delivery of terrigenous sediments with important concentrations of OM to the CB during periods of enhanced precipitation sustained higher Mo scavenging rates. Higher OM content in the eroded sediments as indicated by depleted speleothem-$\delta^{13}C$ values may have also acted as fertilizer to marine microbial activity with consequent major consumption of oxygen in a positive feedback loop to the sedimentary accumulation of Mo (Brumsack, 2006).

The opposite is also valid during times of decreased precipitation in northeastern Venezuela. Higher availability of oxygen due to reduced marine productivity and terrigenous organic input, led to the observed lowering in Mo concentrations (Fig. 24b). The co-occurrence of these conditions has already been described by Gibson & Peterson, (2014) and Peterson et al., (2000) for interstadials and stadials of MIS 3 interglacial but on a much larger scale. High concentrations of Mo (~1000 cps), total organic carbon (TOC) and $CaCO_3$ accumulation (15 g/cm^2 ky), together with higher abundances of the productivity indicator *Globigerina bulloides* and darker, less reflective sediments, with large amounts of Fe and Ti (~0.65%, Peterson & Haug, 2006), were interpreted to reflect increased precipitation and biological productivity. However, during the Holocene time windows analyzed in the present study, Ti and gray scale variations are not so consistent with the speleothem isotope record (Fig. 24). Comparison to the productivity proxy

published by Black et al. (1999), covering the last 800 years further validate this link (Fig. 24a).

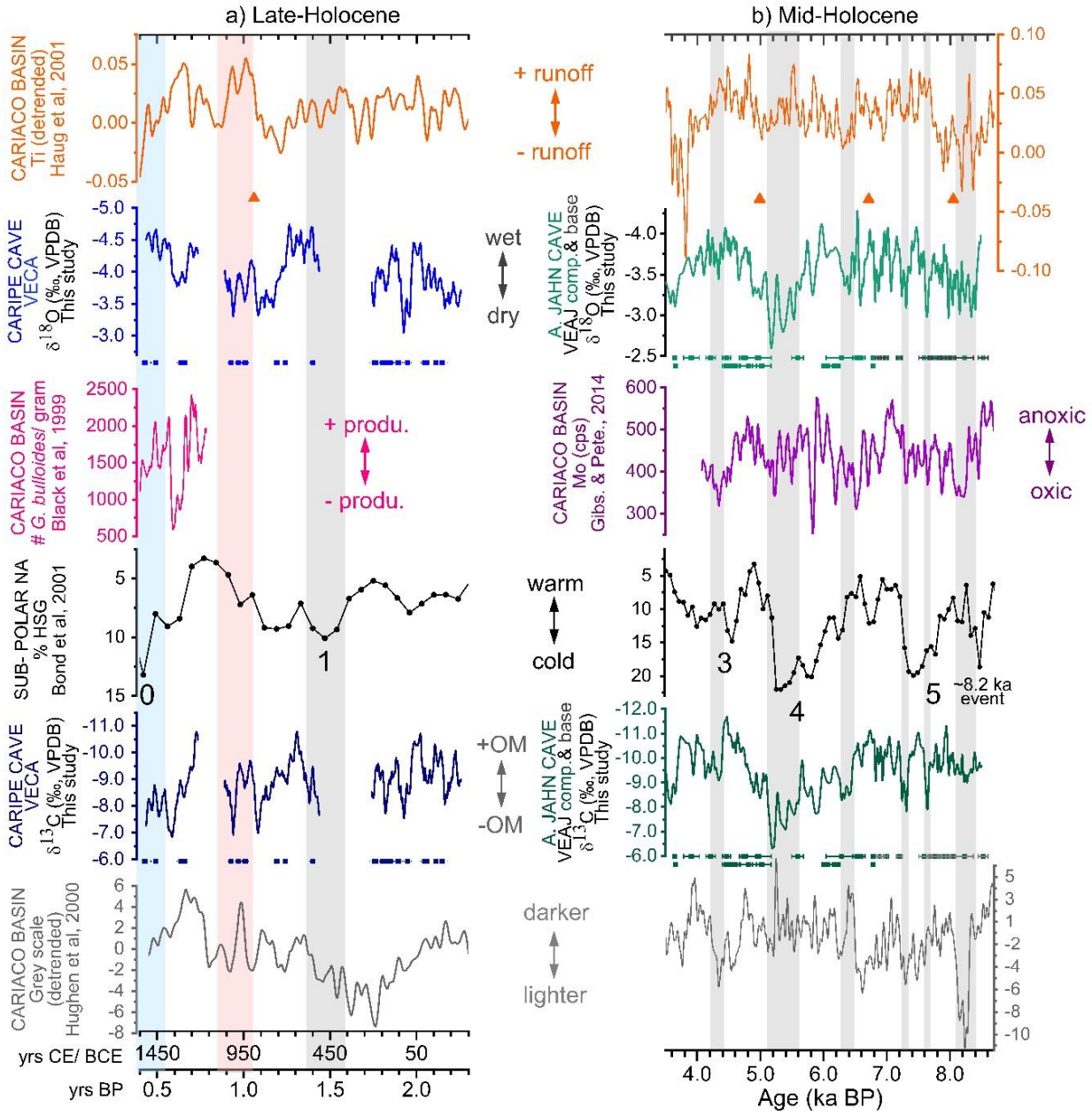

Fig. 24. a) Late and **b)** Mid-Holocene records from Venezuelan speleothems (this study) compared to high-resolution records from the Cariaco Basin and Subpolar North Atlantic. From top to bottom and left to right (when needed): detrended Ti concentration 30-yr running mean (orange, Haug et al., 2001); VECA 20-yr running mean (blue) and VEAJ 25-yr running mean (green) speleothem-$\delta^{18}O$ (this study), Cariaco number of *Globigerina bulloides* per gram 15-yr running mean (pink, Black et al., 1999), Cariaco Molybdenum

concentration 45-yr running mean (purple, Gibson & Peterson, 2014); Subpolar North Atlantic hematite-stained grains (HSG) (Bond et al., 2001); VECA 20-yr running mean (dark blue) and VEAJ 25-yr running mean (dark green) speleothem-$\delta^{13}C$ (this study); and detrended grey scale 30-yr running mean (gray, Hughen et al., 2000). Numbers correspond to the Bond Cycles as shown in the original article and reflect colder temperatures in the North Atlantic Basin. Red and blue shadings in panel a) represent the MCA (900-1100 CE) and LIA (1400-1820 CE) periods as defined in Bird et al., (2011), respectively. Gray shadings in panel a) and b) mark important dry conditions, not always related to Bond cycles. Note that scale for the $\delta^{18}O$ records is inverted; and Ti concentration and grey scale Mid-Holocene graphs have been expanded to better relate its variability.

Their record, when compared to the Caripe Cave speleothem, shows a reasonable correlation between higher numbers of *G. bulloides*/gram, wetter periods and increased soil cover and darker sediments (Fig. 24a). We refrain from making further detailed inferences from these comparisons as uncertainties in the age models can lead to large differences in interpretations. However, an out-of-phase relation is observed between our $\delta^{18}O$-speleothem record and Ti concentrations during the last 1000 years (Fig. 24a). For instance, during the MCA, relatively higher $\delta^{18}O$ values co-occurs with relatively higher Ti amounts.

Over the Middle and Late Holocene, several sustained dry periods in our Venezuelan speleothem records coincide with the advection of cooler surface waters as interpreted by increased amount of ice-rafted debris in subpolar North Atlantic sediment cores (Bond cycles) (Bond et al., 2001). The most remarkable example is the event with the highest $\delta^{18}O$ values centered at ~5.2 ka BP corresponding to the Bond cycle 4, the strongest of the so-called IRDs (Bond et al., 2001). Other events with predominantly higher $\delta^{18}O$ values observed at ~8.3, ~7.7 and 7.3, and 1.12 ka BP in the VEAJ and VECA records can roughly be related to the 8.2 ka cold event, Bond cycles 5 and 1, respectively. Both Bond cycle 0 or Little Ice Age (LIA) and the oldest portion of the Bond cycle 1 between 230 and 510 CE, are represented as a hiatus in our speleothem, which might reflect dry local conditions in association with these events (Fig. 24a). Another important dry period as interpreted in our Venezuelan record occurs at ~6.4 ka, and appears to be roughly

synchronous to the other proxies from the Cariaco Basin (Fig. 24b). This anomaly could also found its origins in the NA as suggested by the subtle increase in HSG concentration, but tropical factors could also play an important role as amplifiers or even as the triggering mechanisms (Gibson & Peterson, 2014). The resolution of the Bond events, however, is considerably lower than our stable isotope records and they are not as well dated as our speleothems, therefore they may not correlate perfectly. However, when compared to other high-resolution records from the Caribbean, more detailed analysis can lead to additional observations.

8.2. Mid-Holocene Comparisons

Detailed comparisons between tropical America high-resolution records and HSG concentration shows a not straightforward relation between hydroclimate variability and cold events in the NA during the Mid-Holocene Bond Cycles 5, 4 and 3. Based on the similitude between Venezuela (this study) and Cuba speleothems (Fensterer et al., 2013), we show that the onset and termination of the Bond Cycle 5 (Bond et al., 2001) seems to have been bounded by abrupt dry periods in the Caribbean (Fig. 25). Whereas at peak Bond 5 between ~7.6 and 7.4 ka, precipitation in western Caribbean increased. Noteworthy, these wet conditions were concurrent with decreased convection in the SAMS domain as observed in the low elevation Andes of Peru (Bustamante et al., 2016). These wet northern/dry southern tropics scenario during the Bond 5 is at odds to the notion of a southern positioned ITCZ and enhanced SAMS during NA cold events. However, it might respond to background peak conditions in NH insolation (Berger & Loutre, 1991; Hodell et al., 1991) that derived in warm and wet Caribbean conditions. Indeed, reconstructed Mg/Ca-SSTs in the Gulf of Mexico (GOM) show that temperatures were higher above 27°C during this period (LoDico et al., 2006) (Fig. 25). And high-resolution E-P record from Lake Miragoane in Haiti shows rising lake levels between 8.2 to 7.0 ka BP (Hodell et al., 1991). The lowest $\delta^{18}O$ values in precipitation are observed during the Caribbean rainy season from June to September when the North Atlantic Subtropical High (NASH) and the mean ITCZ position moves northward, driving increased precipitation over Cuba and northern Venezuela, respectively (Martinez et al., 2019). In addition, to the simultaneous eastward expansion of the Atlantic Warm Pool (AWP) (Wang

& Enfield, 2001; Wang et al., 2007). We suggest that precessional-forced increase in NH insolation as reflected by warmer Caribbean SSTs, led for increased convection in the Circum-Caribbean during a period of relative increase in NA ice sheets.

Insolation in the NH started decreasing in simultaneous to the increase in SH insolation at some point around 6 ka (Berger & Loutre, 1991; Laskar et al., 2004). And so, eastern Caribbean drying and SAMS convection were favored during Bond Cycle 4, as observed in the higher $\delta^{18}O$ speleothem values in Cuba, Barbados and Venezuela, and lower values in Peru (Fig. 26). Western Caribbean precipitation was enhanced and relatively stable during this period (Lachniet et al., 2004; Serrato Marks et al., 2021; Winter et al., 2020), just showing an abrupt anomaly toward dryer conditions around 5.6 ka as depicted by Yucatan Peninsula speleothem high-resolution record (Serrato Marks et al., 2021). Suggesting that hydroclimate variability in the eastern and western Caribbean responded to different forcing mechanisms. Eastern Caribbean appears to have been more sensible to NA cold SSTs during the mid-Holocene. Bond event 4 is characterized by the greatest drift-ice discharge (~22 %HSG). Associated to climax cold, windy NA climate conditions (Bond et al., 2001; Jackson et al., 2005a; O'Brien et al., 1995) and reduction in the NADW as inferred from the $\delta^{13}C$ of benthic foraminifers from the NA Ocean (Oppo et al., 2003).

The Bond cycle 3 was weaker and of shorter duration than the previous events (Bond et al., 2001). So, it did not lead to an ITCZ displacement farther down south of Barbados and Venezuela, likely in a situation analogous to the October-November months. In such scenario analogous to the modern annual cycle, the contraction of the AWP and the divergence observed in the NW Caribbean derives in drying in Cuba as is indeed observed over the duration of the Bond Cycle 3 between 4.6 and 4.4 ka BP. During this period the convection in SAMS weakens as depicted by the higher values of Shatuca record (Fig. 26).

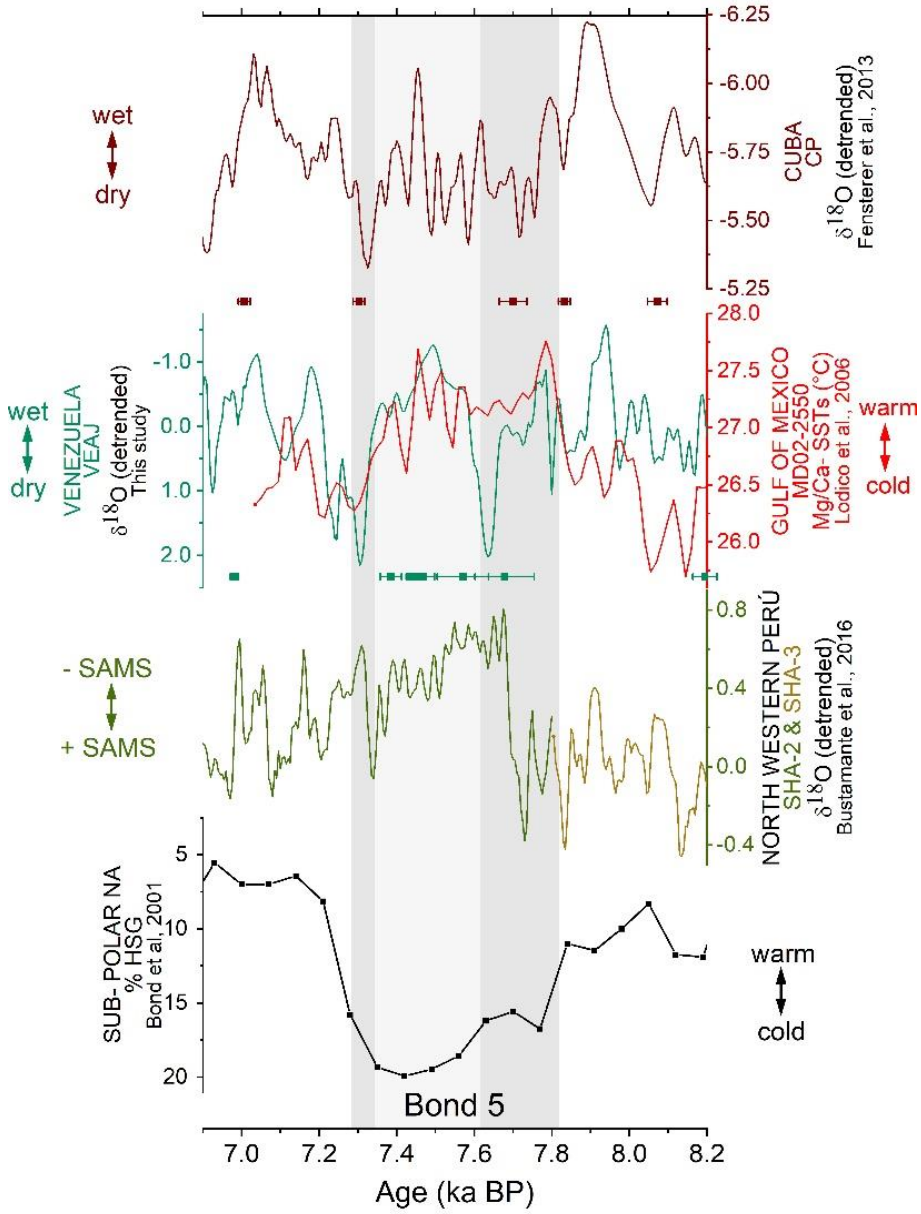

Fig. 25. Comparison between detrended and 15-yrs smoothed speleothem $\delta^{18}O$ (‰ VPDB) records from Cuba (red wine, Fensterer et al., 2013), northern Venezuela VEAJ (jade green, this study) and northern Peru SHA-2 and SHA-3 (green and yellow, Bustamante et al., 2016) spanning the period between 8.2 and 6.9 ka BP. Mg/Ca-SSTs 30-yr running average (red, °C) and 25-yr resolution sea water $\delta^{18}O$ (blue, ‰ VSMOW) reconstructions from the Orca Basin, Gulf of México are also shown (LoDico et al., 2006). Subpolar North Atlantic hematite-stained grains (black, %HSG) reflect colder

temperatures in the NA Basin (Bond et al., 2001). Dark and light gray shadings mark dry and wet conditions in the Caribbean, respectively, associated to Bond cycle 5.

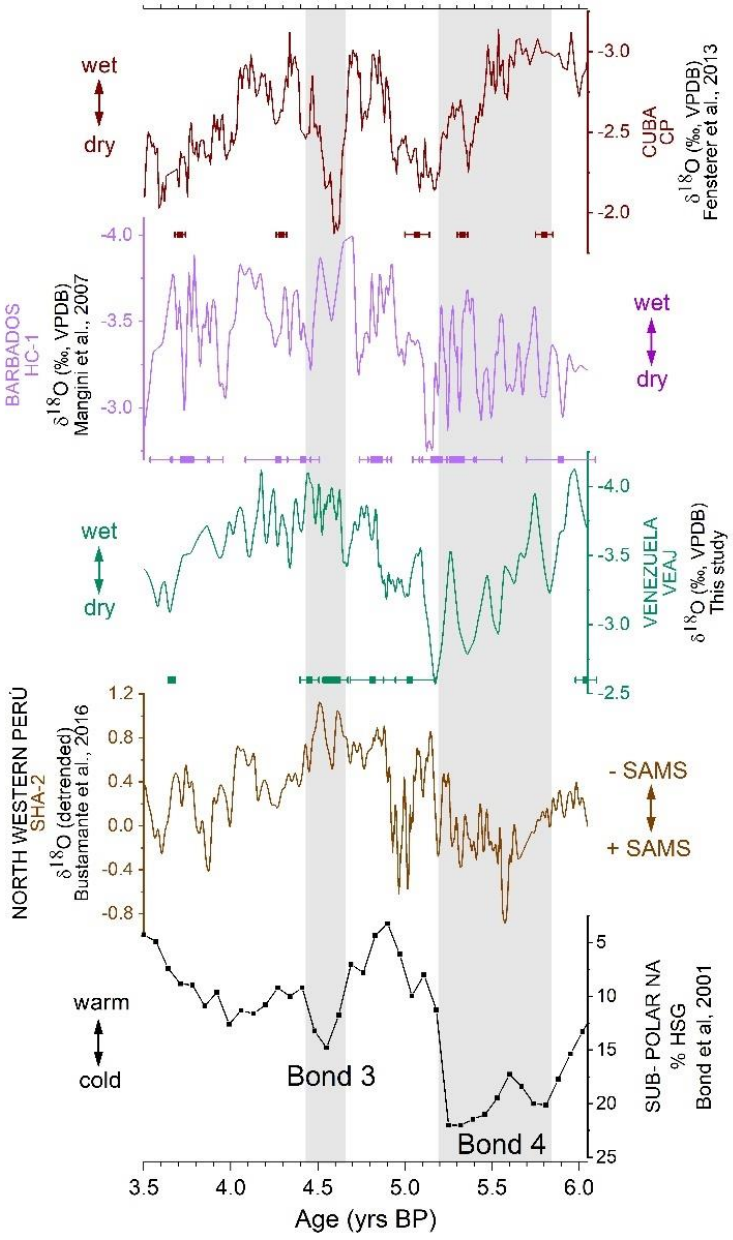

Fig. 26. High resolution speleothem $\delta^{18}O$ (‰ VPDB) records from the Caribbean region: a) Cuba (red wine, Fensterer et al., 2013), b) Barbados (light purple, Mangini et al., 2007), c) northern Venezuela (green, this study), compared to d) mid-altitude Peruvian Andes (Bustamante et al., 2016) and e) subpolar North Atlantic hematite-stained grains (%HSG) (black, Bond et al., 2001), during the period between 3.5 and 6.0 ka BP. Note that scale

for the y-axis is inverted for all records, except for the Shatuca record. Gray shadings mark anomalies in the $\delta^{18}O$ speleothems records, associated to Bond cycle 4 and 3.

8.3. The Late Holocene

Our NE Venezuela record from Caripe Cave considerable differs from the Cariaco Basin Ti record (Haug et al., 2001) during the last 2300 yrs. Pointing to non-previously reported relations to Caribbean and southern hemisphere tropical high-resolution records. Prior to 700 CE, as in the SAMS domain, precipitation in the region of influence of the ITCZ also appear to have been stable, with observed variability closely relating northeastern Brazil (NEB) (Della Libera et al., 2022; Novello et al., 2012) (Fig. 27). Whereas, during almost the last 1000 years our Caripe record, closely resembles the western tropical SA records (Apaéstegui et al., 2014; Bird et al., 2011; Della Libera et al., 2022) (Fig. 27). Which means a relatively dry (wet) mean state of the climate during the MCA (first part of the LIA) and a connection to the SAMS convection. What seems strange at first, makes sense if we account for the relative displacement of the ITCZ from northern Venezuela. We suggest that during the MCA (900-1100 CE), the ITCZ located further north of Venezuela which led to the observed relatively high $\delta^{18}O$ values.

Likely mirroring September-October months, when the precipitation decreases in Caripe and $\delta^{18}O$ values gets relatively enriched (Fig.15) due to the northward migration of the ITCZ to the southern Lesser Antilles. In addition to an expansion of the AWP, which indeed could have been the case during the MCA, when anomalous warm temperatures where observed in the NH (Mann et al., 2009; Moberg et al., 2005). This scenario is supported by the peak wet conditions observed in Cuba around 950 CE (Fensterer et al., 2012) and the Yucatan Peninsula (Medina-elizalde et al., 2010). Thus, locations with greater precipitation in the MCA might have responded to the spatial pattern observed in Fig.28d. In phase wet conditions between Caripe and the monsoon core region during the first part of the LIA (1400-1530 CE) (Fig. 27), might reflect an ITCZ mean position close to NE Venezuela, likely over Guianas, enhancing the moisture conduit to the SAMS region. We hypothesize this situation might be analogous to the one observed during December with Caribbean spatial patterns likely of resembling those in Fig. 28f. Cold conditions might have prevailed during this period leading to open vegetation and heavier $\delta^{13}C$ values in

Caripe, as also indicated by the persistence of pioneer species *Cecropia* in pollen records from French Guiana (Ledru, 2001) and glacial advances in the Cordillera de Merida (Polissar et al., 2006).

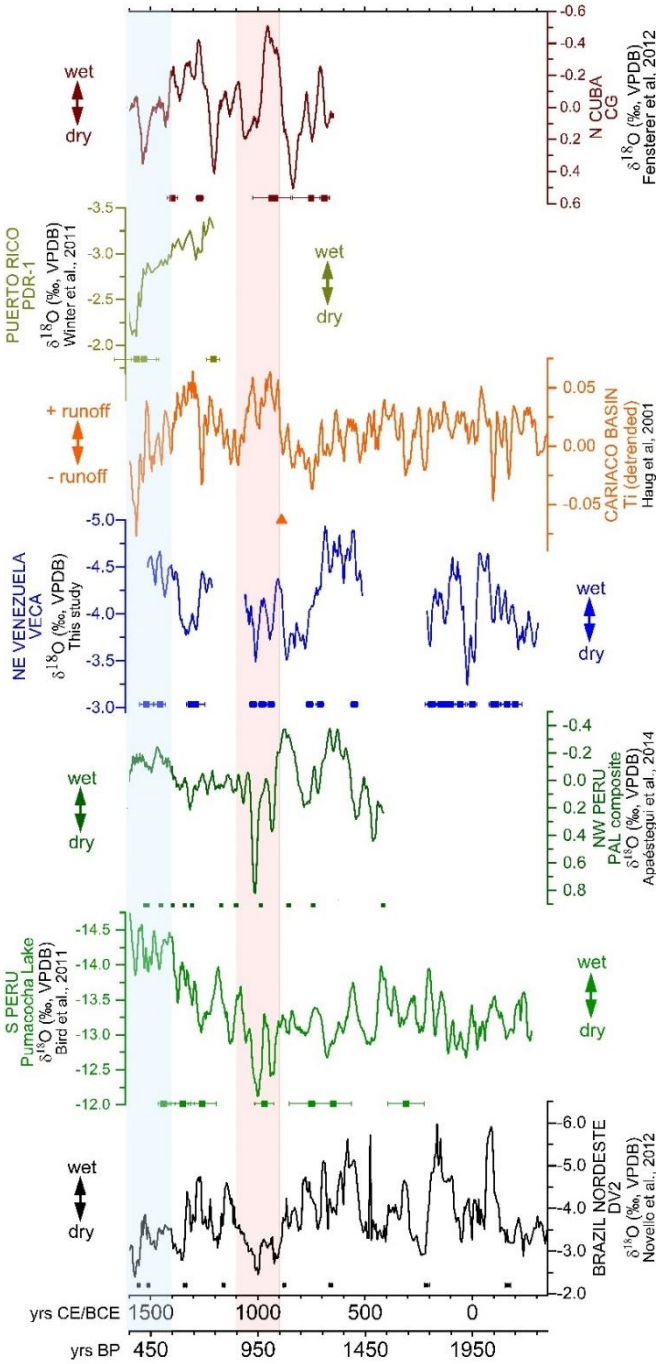

Fig. 27. Comparison between detrended and 25-yrs smoothed speleothem $\delta^{18}O$ (‰ VPDB) records from Cuba (red wine, Fensterer et al., 2012), Puerto Rico (yellow, Winter et al., 2011), Cariaco Basin Ti (orange, Haug et al., 2001), northeastern Venezuela VECA

(blue, this study), northwestern Peru (dark green, Apaéstegui et al., 2014), southern Peru (green, Bird et al., 2011) and northeastern Brazil (black, Novello et al., 2012) spanning the period between 350 BCE and 1600 CE. Red and blue shadings represent the MCA (900-1100 CE) and LIA (1400-1820 CE) periods as defined in Bird et al., (2011), respectively. Note that scale for the $\delta^{18}O$ records is inverted.

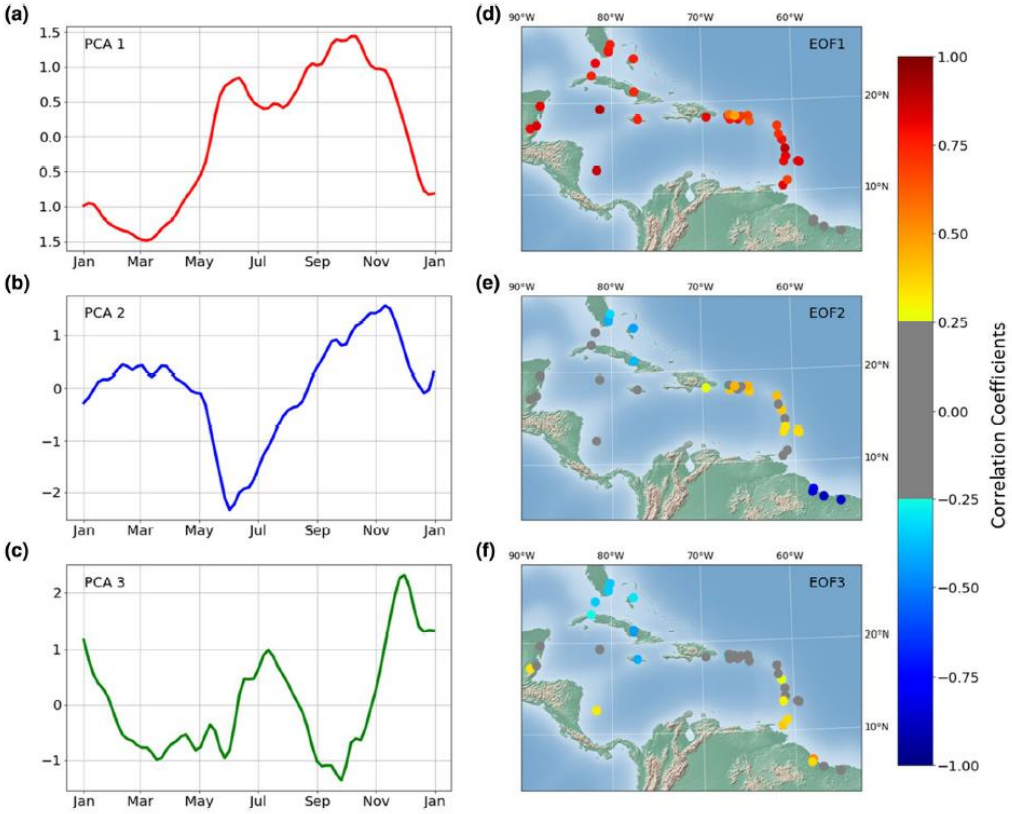

Fig. 28. Principal component analysis of seasonal rainfall cycle over the Caribbean (a-c), explaining 54%, 16% and 8% of the total variance, respectively, and spatial correlation coefficients (d-f) of the climatological Caribbean pentad rainfall at 38 CIMH/ GHCN stations. Coefficients > 0.25 or <-0.25 are colored for significance. **(a, d)** PCA 1 display the known seasonal characteristics dominant in the Caribbean, with maximum rainfall occurring during September to mid-November. **(b, e)** PCA 2 also shows a gradual ascent of rainfall towards September-October-November in positively correlated stations in the southeast, from the mid to upper portion of the lesser Antilles, Virgin Islands and Puerto Rico. Negative correlations are observed in Florida, Cuba, the Bahamas and in the Guianas and implies peak June precipitation and weaker SON precipitation. **(c, f)** positive

correlations to the PCA 3 indicates stations with higher precipitation during July-August, peaking in late November and December (i.e. some stations in central America, the lower tier of the Lesser Antilles, and Guyana). Stations in the NW Caribbean (i.e. Cuba, Jamaica, Bahamas, and Florida) have negative correlations. Modified from Martinez et al., (2019).

9. CONCLUSIONS

Precipitation in northeastern Venezuela is subjected to the geographic location that mainly determines the exposure to the moisture carrying trade winds. Whereas, isotopic composition imprint on rainfall represents more regional mechanisms. Based on the available data, we suggest that on monthly scales, $\delta^{18}O$ isotopic variability mainly responds to the *amount effect* related to the latitudinal migration of the ITCZ convective activity. Which in turn is associated to the evaporative enrichment of the raindrops during the dry months from January to March leading to heavier $\delta^{18}O$ values. And enhanced Rayleigh distillation during the wet season from May to December inducing lighter $\delta^{18}O$ values in precipitation (Fröhlich et al., 2002; Rozanski et al., 1993). More data are needed for further supporting this hypothesis and the possible influence of local sources of moisture during the last month of the year.

The negative correlation between annual weighted $\delta^{18}O$ values and precipitation totals point to the *amount effect*. However, the non-significance (p-value= 0.1759>0.05) might be related to the few data included in the correlation. Again, we highlight the need for producing more continuous meteorological data with information on the isotope composition of water. As well as conducting parallel monitoring surveys of dripping waters and calcite precipitates in Venezuelan Caves of paleoclimatic interest.

Covariation between $\delta^{18}O$ and $\delta^{13}C$-speleothem values in northeastern Venezuela and molybdenum concentration in CB sediments points to a close relation between hydroclimate, vegetation density/soil cover and oxygen balance in the CB. We suggest that wet conditions and increased delivery of organic matter-rich terrigenous-sediments likely led to necessary reductive conditions to accumulate Mo in CB sediments through the increase in primary productivity and O_2 consumption. Those observations were accompanied by minor, almost negligibly variations in Ti and sediment reflectance. Except for the last 2300 yrs, in which the relation to $\delta^{18}O$ and CB Ti concentration in sediments considerable differs.

Venezuelan records are strategically located to track the mean position of the ITCZ during important climate perturbations. An attempt that has been previously assessed indirectly by Caribbean (Fensterer et al., 2012, 2013; Mangini et al., 2007; Winter et al., 2011) and

tropical SH paleorecords (Apaéstegui et al., 2014; Bird et al., 2011; Novello et al., 2012; Stríkis et al., 2011; Vuille et al., 2012). We show that Holocene hydroclimate variability in Venezuela has primary (but not exclusively) responded to NA climate (Bond cycles) (Bond et al., 2001) with repercussions in the Cariaco Basin dynamics (Black et al., 1999; Gibson & Peterson, 2014; Haug et al., 2001; Hughen et al., 2000). The magnitude of those events as depicted by the concentration of HSG in the sub-polar NA sediments and the background insolation conditions might have been the main determinants. Increased NH insolation during the Mid-Holocene likely led to mostly in-phase relations between Alfredo Jahn and eastern Caribbean records. Contrasting the invariable convective activity observed over Central America (Serrato Marks et al., 2021; Winter et al., 2020). Whereas, during the Late-Holocene and out-phase relation is observed between Caripe and Caribbean records. During this particular period Caripe record appears to be closely related to the SAMS dynamics.

Apparent wet conditions are observed during peak Bond Cycle 5 in Cuba (Fensterer et al., 2013) and Venezuela, suggesting an ITCZ overhead and warmer Caribbean SSTs (LoDico et al., 2006). Conversely, between 5.8 and 5.2 ka, cold and windy NH climate in sync with the strongest of the Bond events (Bond 4) (Bond et al., 2001; Jackson et al., 2005b; Oppo et al., 2003), induced the southward displacement of the ITCZ and enhancement of the SAMS (Bustamante et al., 2016). Wet conditions in Venezuela and the southern Lesser Antilles (Mangini et al., 2007) were observed during the relative weak Bond Cycle 3, suggesting a subtle displacement of the mean position of the ITCZ, hence diminished convection in the SAMS region.

The Late Holocene Caripe record shows two distinct periods. From 350 BCE to 870 CE the convection was high and relatively stable, with variability apparently related to the Diva de Maura record from the NEB (Novello et al., 2012) likely also forced by the AMO in a common 40-yr periodicity. During the last 1000 years, instead, Caripe closely resembled the SAMS paleorecords in timing and direction (Apaéstegui et al., 2014; Bird et al., 2011; Della Libera et al., 2022). Relatively higher $\delta^{18}O$ values during the MCA reflects a further north position of the ITCZ. And lower values during the first part of the LIA point to mean

ITCZ position over the Guianas, which apparently by this time was enough to drive important moisture influx to the SAMS domain.

10. REFERENCES

Adam, O., Bischoff, T., & Schneider, T. (2016). Seasonal and interannual variations of the energy flux equator and ITCZ. Part I: Zonally averaged ITCZ position. *Journal of Climate*, *29*(9), 3219–3230. https://doi.org/10.1175/JCLI-D-15-0512.1

Algeo, T. J., & Rowe, H. (2012). Paleoceanographic applications of trace-metal concentration data. *Chemical Geology*, *324–325*, 6–18. https://doi.org/10.1016/j.chemgeo.2011.09.002

Apaéstegui, J., Cruz, F. W., Sifeddine, A., Vuille, M., Espinoza, J. C., Guyot, J. L., Khodri, M., Strikis, N., Santos, R. V., Cheng, H., Edwards, L., Carvalho, E., & Santini, W. (2014). Hydroclimate variability of the northwestern Amazon Basin near the Andean foothills of Peru related to the South American Monsoon System during the last 1600 years. *Climate of the Past*, *10*(6), 1967–1981. https://doi.org/10.5194/cp-10-1967-2014

Berger, A., & Loutre, M. F. (1991). Insolation values for the climate of the last 10 million years. *Quaternary Science Reviews*, *10*(4), 297–317. https://doi.org/10.1016/0277-3791(91)90033-Q

Bird, B. W., Abbott, M. B., Vuille, M., Rodbell, D. T., Stansell, N. D., & Rosenmeier, M. F. (2011). A 2,300-year-long annually resolved record of the South American summer monsoon from the Peruvian Andes. *Proceedings of the National Academy of Sciences of the United States of America*, *108*(21), 8583–8588. https://doi.org/10.1073/pnas.1003719108

Bischoff, T., & Schneider, T. (2014). Energetic constraints on the position of the intertropical convergence zone. *Journal of Climate*, *27*(13), 4937–4951. https://doi.org/10.1175/JCLI-D-13-00650.1

Black, D. E., Peterson, L. C., Overpeck, J. T., Kaplan, A., Evans, M. N., & Kashgarian, M. (1999). Eight centuries of North Atlantic ocean atmosphere variabitity. *Science*, *286*(5445), 1709–1713. https://doi.org/10.1126/science.286.5445.1709

Bohm, E., Lippold, J., Gutjahr, M., Frank, M., Blaser, P., Antz, B., Fohlmeister, J., Frank,

N., Andersen, M. B., & Deininger, M. (2015). Strong and deep Atlantic meridional overturning circulation during the last glacial cycle. *Nature*, *517*(7532), 73–76. https://doi.org/10.1038/nature14059

Bond, G., Kromer, B., Beer, J., Muscheler, R., Evans, M. N., Showers, W., Hoffmann, S., Lotti-Bond, R., Hajdas, I., & Bonani, G. (2001). Persistent solar influence on north atlantic climate during the Holocene. *Science*, *294*(5549), 2130–2136. https://doi.org/10.1126/science.1065680

Broccoli, A. J., Dahl, K. A., & Stouffer, R. J. (2006). Response of the ITCZ to Northern Hemisphere cooling. *Geophysical Research Letters*, *33*(1), 1–4. https://doi.org/10.1029/2005GL024546

Brumsack, H. (2006). *The trace metal content of recent organic carbon-rich sediments : Implications for Cretaceous black shale formation*. *232*, 344–361. https://doi.org/10.1016/j.palaeo.2005.05.011

Bunn, A. G. (2008). A dendrochronology program library in R (dplR). *Dendrochronologia*, *26*(2), 115–124. https://doi.org/10.1016/j.dendro.2008.01.002

Bustamante, M. G., Cruz, F. W., Vuille, M., Apaéstegui, J., Strikis, N., Panizo, G., Novello, F. V., Deininger, M., Sifeddine, A., Cheng, H., Moquet, J. S., Guyot, J. L., Santos, R. V., Segura, H., & Edwards, R. L. (2016). Holocene changes in monsoon precipitation in the Andes of NE Peru based on δ18O speleothem records. *Quaternary Science Reviews*, *146*, 274–287. https://doi.org/10.1016/j.quascirev.2016.05.023

Chiang, J. C. H., & Bitz, C. M. (2005). Influence of high latitude ice cover on the marine Intertropical Convergence Zone. *Climate Dynamics*, *25*(5), 477–496. https://doi.org/10.1007/s00382-005-0040-5

Chiessi, C. M., Mulitza, S., Taniguchi, N. K., Prange, M., Campos, M. C., Häggi, C., Schefuß, E., Pinho, T. M. L., Frederichs, T., Portilho-Ramos, R. C., Sousa, S. H. M., Crivellari, S., & Cruz, F. W. (2021). Mid- to Late Holocene Contraction of the Intertropical Convergence Zone Over Northeastern South America. *Paleoceanography and Paleoclimatology*, *36*(4), 1–20.

https://doi.org/10.1029/2020PA003936

Clark, I. D., & Fritz, P. (1997). Environmental isotopes in hydrogeology. In *Environmental Geology* (Vol. 43, Issue 5). CRC Press. https://doi.org/10.1029/99eo00169

Craig, H. (1961). Isotopic variations in meteoric waters. *Science*, *133*(3465), 1702–1703. https://doi.org/10.1126/science.133.3465.1702

Cruz, F. W., Vuille, M., Burns, S. J., Wang, X., Cheng, H., Werner, M., Lawrence Edwards, R., Karmann, I., Auler, A. S., & Nguyen, H. (2009). Orbitally driven east-west antiphasing of South American precipitation. *Nature Geoscience*, *2*(3), 210–214. https://doi.org/10.1038/ngeo444

Dansgaard, W. (1964). Stable isotopes in precipitation. *Tellus*, *16*(4), 436–468. https://doi.org/10.3402/tellusa.v16i4.8993

Davis, N. A., Seidel, D. J., Birner, T., Davis, S. M., & Tilmes, S. (2016). Changes in the width of the tropical belt due to simple radiative forcing changes in the GeoMIP simulations. *Atmospheric Chemistry and Physics*, *16*(15), 10083–10095. https://doi.org/10.5194/acp-16-10083-2016

Della Libera, M. E., Novello, V. F., Cruz, F. W., Orrison, R., Vuille, M., Maezumi, S. Y., de Souza, J., Cauhy, J., Campos, J. L. P. S., Ampuero, A., Utida, G., Stríkis, N. M., Stumpf, C. F., Azevedo, V., Zhang, H., Edwards, R. L., & Cheng, H. (2022). Paleoclimatic and paleoenvironmental changes in Amazonian lowlands over the last three millennia. *Quaternary Science Reviews*, *279*. https://doi.org/10.1016/j.quascirev.2022.107383

Deplazes, G., Lückge, A., Peterson, L. C., Timmermann, A., Hamann, Y., Hughen, K. A., Röhl, U., Laj, C., Cane, M. A., Sigman, D. M., & Haug, G. H. (2013). Links between tropical rainfall and North Atlantic climate during the last glacial period. *Nature Geoscience*, *6*(3), 213–217. https://doi.org/10.1038/ngeo1712

Deplazes, G., Meckler, A. N., Peterson, L. C., Hamann, Y., Aeschlimann, B., Günther, D., Martínez-García, A., & Haug, G. H. (2019). Fingerprint of tropical climate variability

and sea level in sediments of the Cariaco Basin during the last glacial period. *Sedimentology*, *66*(5), 1967–1988. https://doi.org/10.1111/sed.12567

Diaz, H. F., & Pulwarty, R. S. (1992). A comparison of Southern Oscillation and El Nino events in the Tropics. In H. F. Diaz & V. Markgraf (Eds.), *El Niño: Historical and Paleoclimatic Aspects of the Southern Oscillation* (pp. 175–192). Cambridge University Press.

Dorale, J. A., Edwards, R. L., Alexander, E. C. J., Shen, C.-C., Richards, D. A., & Cheng, H. (2004). Uranium-series dating of speleothems: current techniques, limits, & applications. In I. D. Sasowsky & J. Mylroie (Eds.), *Studies of Cave Sediments. Physical and chemical records of paleoclimate* (pp. 177–197). Kluwer Academic/Plenum Publishers. https://doi.org/10.1007/978-1-4419-9118-8

Dorale, J. A., & Liu, Z. (2009). Limitations of hendy test criteria in judging the paleoclimatic suitability of speleothems and the need for replication. *Journal of Cave and Karst Studies*, *71*(1), 73–80.

Enfield, D. B., Mestas-Nuñez, A. M., & Trimble, P. J. (2001). The Atlantic multidecadal oscillation and its relation to rainfall and river flows in the continental U.S. *Geophysical Research Letters*, *28*(10), 2077–2080.

Fairchild, I. J., Smith, C. L., Baker, A., Fuller, L., Spötl, C., Mattey, D., & McDermott, F. (2006). Modification and preservation of environmental signals in speleothems. *Earth-Science Reviews*, *75*(1–4), 105–153. https://doi.org/10.1016/j.earscirev.2005.08.003

Fensterer, C., Scholz, D., Hoffmann, D. L., Spötl, C., Schröder-Ritzrau, A., Horn, C., Pajón, J. M., & Mangini, A. (2013). Millennial-scale climate variability during the last 12.5ka recorded in a Caribbean speleothem. *Earth and Planetary Science Letters*, *361*, 143–151. https://doi.org/10.1016/j.epsl.2012.11.019

Fensterer, C., Scholz, D., Hoffmann, D., Spötl, C., Pajón, J. M., & Mangini, A. (2012). *Cuban stalagmite suggests relationship between Caribbean precipitation and the Atlantic Multidecadal Oscillation during the past 1 . 3 ka*.

https://doi.org/10.1177/0959683612449759

Forti, P., Urbani, F., & Rossi, A. (1999). Minerales secundarios de las Cuevas del Indio y Alfredo Jahn, Estado Miranda, Venezuela. *Boletín Informativo de La Comisión de Geoespeleología (Federación Espeleológica de América Latina y El Caribe -FEALC-)*, *7*, 1–6.

Frajka-Williams, E., Beaulieu, C., & Duchez, A. (2017). Emerging negative Atlantic Multidecadal Oscillation index in spite of warm subtropics. *Scientific Reports*, *7*(1), 1–8. https://doi.org/10.1038/s41598-017-11046-x

Fröhlich, K., Gibson, J. J., & Aggarwal, P. K. (2002). Deuterium excess in precipitation and its climatological significance. *International Atomic Energy Agency*, 54–66.

Gat, J. R. (1996). Oxygen and hydrogen isotopes in the hydrologic cycle. *Annual Review of Earth and Planetary Sciences*, *24*, 225–262. https://doi.org/10.1146/annurev.earth.24.1.225

Gat, J. R. (1971). Comments on the Stable Isotope Method in Regional Groundwater Investigations. *Water Resources Research*, *7*(4), 980–993. https://doi.org/10.1029/WR007i004p00980

Gibson, K. A., & Peterson, L. C. (2014). A 0.6 million year record of millenial-scale variability in the tropics. *Geophysical Research Letters*, *41*, 969–975. https://doi.org/10.1002/2013GL058846.Received

Goldenberg, S. B., Landsea, C. W., Mestas-Nuñez, A. M., & Gray, W. M. (2001). The recent increase in Atlantic hurricane activity: Causes and implications. *Science*, *293*(5529), 474–479. https://doi.org/10.1126/science.1060040

Gonfiantini, R. (1986). Environmental isotopes in lake studies. *Handbook of Environmental Isotope Geochemistry, the Terrestrial Environment*, *2*, 113–168.

Gschwendtner, J. V. G. (1963). Valencia lake as a hydrological indicator 1901–62. *International Association of Scientific Hydrology. Bulletin*, *8*(3), 64–70. https://doi.org/10.1080/02626666309493338

Gu, G., & Zhang, C. (2002). Cloud components of the intertropical convergence zone. *Journal of Geophysical Research Atmospheres*, *107*(21), 1–12. https://doi.org/10.1029/2002JD002089

Hammer, Ø., Harper, D. A. T., & Ryan, P. D. (2001). PAST: Paleontological statistics software package for education and data analysis. *Paleontologia Electronica*, *4*(1), 1–9. http://palaeo-electronica.org/2001_1/past/issue1_01.htm

Haug, G. H., Hughen, K. A., Sigman, D. M., Peterson, L. C., & Ro, U. (2001). Southward Migration of the ITCZ Holocene. *Science*, *293*(5533), 1304–1309.

Hendy, C. H. (1971). The isotopic geochemistry of speleothems-I. The calculation of the effects of different modes of formation on the isotopic composition of speleothems and their applicability as palaeoclimatic indicators. *Geochimica et Cosmochimica Acta*, *35*(8), 801–824. https://doi.org/10.1016/0016-7037(71)90127-X

Herbert, T. D., & Schuffert, J. D. (2000). Alkenone unsaturation estimates of sea-surface temperatures at Site 1002 over a full glacial cycle. *Proceedings of the Ocean Drilling Program: Scientific Results*, *165*(June), 239–247. https://doi.org/10.2973/odp.proc.sr.165.030.2000

Hersbach, H., Bell, B., Berrisford, P., Hirahara, S., Horányi, A., Muñoz-Sabater, J., Nicolas, J., Peubey, C., Radu, R., Schepers, D., Simmons, A., Soci, C., Abdalla, S., Abellan, X., Balsamo, G., Bechtold, P., Biavati, G., Bidlot, J., Bonavita, M., … Thépaut, J. N. (2020). The ERA5 global reanalysis. *Quarterly Journal of the Royal Meteorological Society*, *146*(730), 1999–2049. https://doi.org/10.1002/qj.3803

Hetzinger, S., Pfeiffer, M., Dullo, W. C., Keenlyside, N., Latif, M., & Zinke, J. (2008). Caribbean coral tracks Atlantic Multidecadal Oscillation and past hurricane activity. *Geology*, *36*(1), 11–14. https://doi.org/10.1130/G24321A.1

Hodell, D. A., Curtis, J. H., Jones, G. A., Higuera-Gundy, A., Brenner, M., Binford, M. W., & Dorsey, K. T. (1991). Reconstruction of Caribbean climate change over the past 10,500 years. *Nature*, *352*, 790–793. https://doi.org/10.1038/255242a0

Huffman, G. J., Stocker, D. T., Bolvin, E. J., & Nelkin, J. . (2019). *GPM IMERG Final Precipitation L3 1 day 0.1 degree x 0.1 degree* (No. V06). Edited by Andrey Savtchenko, Greenbelt, MD, Goddard Earth Sciences Data and Information Services Center (GES DISC).

Hughen, K. A., Southon, J. R., Lehman, S. J., & Overpeck, J. T. (2000). Synchronous radiocarbon and climate shifts during the last deglaciation. *Science*, *290*(5498), 1951–1954. https://doi.org/10.1126/science.290.5498.1951

Jackson, M. G., Oskarsson, N., Trønnes, R. G., McManus, J. F., Oppo, D. W., Grönvold, K., Hart, S. R., & Sachs, J. P. (2005a). Holocene loess deposition in Iceland: Evidence for millenial-scale atmosphere-ocean coupling in the North Atlantic. *Geology*, *33*(6), 509–512. https://doi.org/10.1130/G21489.1

Jackson, M. G., Oskarsson, N., Trønnes, R. G., McManus, J. F., Oppo, D. W., Grönvold, K., Hart, S. R., & Sachs, J. P. (2005b). Holocene loess deposition in Iceland: Evidence for millenial-scale atmosphere-ocean coupling in the North Atlantic. *Geology*, *33*(6), 509–512. https://doi.org/10.1130/G21489.1

Kageyama, M., Merkel, U., Otto-Bliesner, B., Prange, M., Abe-Ouchi, A., Lohmann, G., Ohgaito, R., Roche, D. M., Singarayer, J., Swingedouw, D., & Zhang, X. (2013). Climatic impacts of fresh water hosing under Last Glacial Maximum conditions : a multi-model study. *Climate of the Past*, *9*, 935–953. https://doi.org/10.5194/cp-9-935-2013

Kayano, M. T., & Capistrano, V. B. (2014). How the Atlantic multidecadal oscillation (AMO) modifies the ENSO influence on the South American rainfall. *International Journal of Climatology*, *34*(1), 162–178. https://doi.org/10.1002/joc.3674

Kerr, R. A. (2000). A North Atlantic climate pacemaker for the centuries. *Science*, *288*(5473), 1984–1986. https://doi.org/10.1126/science.288.5473.1984

Knight, J. R., Folland, C. K., & Scaife, A. A. (2006). Climate impacts of the Atlantic multidecadal oscillation. *Geophysical Research Letters*, *33*(17), 2–5. https://doi.org/10.1029/2006GL026242

Kuhlbrodt, T., Griesel, A., Montoya, M., Levermann, A., Hofmann, A., & Rahmastorf, S. (2007). On the driving processes of the Atlantic Meridional Overturning Circulation. *Reviews of Geophysics*, *45*(RG2001), 1–32. https://doi.org/10.1029/2004RG000166

Lachniet, M. S. (2009). Climatic and environmental controls on speleothem oxygen-isotope values. *Quaternary Science Reviews*, *28*(5–6), 412–432. https://doi.org/10.1016/j.quascirev.2008.10.021

Lachniet, M. S., Asmerom, Y., Burns, S. J., Patterson, W. P., Polyak, V. J., & Seltzer, G. O. (2004). Tropical response to the 8200 yr B.P cold event? Speleothem isotopes indicate a weakened early Holocene monsoon in Costa Rica. *Geology*, *32*(11), 957–960. https://doi.org/10.1130/G20797.1

Lapointe, F., Bradley, R. S., Francus, P., Balascio, N. L., Abbott, M. B., Stoner, J. S., St-Onge, G., de Coninck, A., & Labarre, T. (2020). Annually resolved Atlantic sea surface temperature variability over the past 2,900 y. *Proceedings of the National Academy of Sciences of the United States of America*, *117*(44), 27171–27178. https://doi.org/10.1073/pnas.2014166117

Laskar, J., Robutel, P., Joutel, F., Gastineau, M., Correia, A. C. M., & Levrard, B. (2004). A long-term numerical solution for the insolation quantities of the Earth. *Astronomy and Astrophysics*, *428*(1), 261–285. https://doi.org/10.1051/0004-6361:20041335

Lea, D. W., Pak, D. K., Peterson, L. C., & Hughen, K. A. (2003). Synchroneity of tropical and high-latitude Atlantic temperatures over the last glacial termination. *Science*, *301*(5638), 1361–1364. https://doi.org/10.1126/science.1088470

Ledru, M. P. (2001). Late Holocene rainforest disturbance in French Guiana. *Review of Palaeobotany and Palynology*, *115*(3–4), 161–170. https://doi.org/10.1016/S0034-6667(01)00068-9

LoDico, J. M., Flower, B. P., & Quinn, T. M. (2006). Subcentennial-scale climatic and hydrologic variability in the Gulf of Mexico during the early Holocene. *Paleoceanography*, *21*(3), 1–9. https://doi.org/10.1029/2005PA001243

López Pérez, N. (2012). The influence of El Niño Southern Oscillation episodes (ENSO) on rainfall in Monagas State, Venezuela. *Revista Científica UDO Agrícola*, *12*(2), 400–406. https://dialnet.unirioja.es/servlet/articulo?codigo=4688576&info=resumen&idioma=SPA%0Ahttps://dialnet.unirioja.es/servlet/articulo?codigo=4688576&info=resumen&idioma=ENG%0Ahttps://dialnet.unirioja.es/servlet/articulo?codigo=4688576

Mamalakis, A., Randerson, J. T., Yu, J. Y., Pritchard, M. S., Magnusdottir, G., Smyth, P., Levine, P. A., Yu, S., & Foufoula-Georgiou, E. (2021). Zonally contrasting shifts of the tropical rain belt in response to climate change. *Nature Climate Change*, *11*(2), 143–151. https://doi.org/10.1038/s41558-020-00963-x

Mangini, A., Blumbach, P., Verdes, P., Spötl, C., Scholz, D., Machel, H., & Mahon, S. (2007). Combined records from a stalagmite from Barbados and from lake sediments in Haiti reveal variable seasonality in the Caribbean between 6.7 and 3 ka BP. *Quaternary Science Reviews*, *26*(9–10), 1332–1343. https://doi.org/10.1016/j.quascirev.2007.01.011

Mann, M. E., & Emanuel, K. A. (2006). Atlantic Hurricane trends linked to climate change. *Eos*, *87*(24), 233–241. https://doi.org/10.1029/2006EO240001

Mann, M. E., Zhang, Z., Rutherford, S., Bradley, R. S., Hughes, M. K., Shindell, D., Ammann, C., Faluvegi, G., & Fenbiao, N. (2009). Global Signatures and Dynamical Origins of the Little Ice Age and Medieval Climate Anomaly. *Science*, *326*(November), 1256–1260.

Marshall, J., Donohoe, A., Ferreira, D., & McGee, D. (2014). The ocean's role in setting the mean position of the Inter-Tropical Convergence Zone. *Climate Dynamics*, *42*(7–8), 1967–1979. https://doi.org/10.1007/s00382-013-1767-z

Martinez, C., Goddard, L., Kushnir, Y., & Ting, M. (2019). Seasonal climatology and dynamical mechanisms of rainfall in the Caribbean. *Climate Dynamics*, *53*(1–2), 825–846. https://doi.org/10.1007/s00382-019-04616-4

McDermott, F. (2004). Palaeo-climate reconstruction from stable isotope variations in

speleothems: A review. *Quaternary Science Reviews*, *23*(7–8), 901–918. https://doi.org/10.1016/j.quascirev.2003.06.021

McManus, J., Francois, R., Gherardi, J. M., Keigwin, L., & Brown-Leger, S. (2004). Collapse and rapid resumption of Atlantic meridional circualtion linked to deglacial climate changes. *Nature*, *428*(April), 834–837.

Medina-elizalde, M., Burns, S. J., Lea, D. W., Asmerom, Y., Gunten, L. Von, Polyak, V., Vuille, M., & Karmalkar, A. (2010). High resolution stalagmite climate record from the Yucatán Peninsula spanning the Maya terminal classic period. *Earth and Planetary Science Letters*, *298*(1–2), 255–262. https://doi.org/10.1016/j.epsl.2010.08.016

Moberg, A., Sonechkin, D. M., Holmgren, K., Datsenko, M. H., & Karlén, W. (2005). Highly variable Northern Hemisphere temperatures reconstructed from low- and high-resolution proxy data. *Nature*, *433*(7026), 613–617. https://doi.org/10.1038/nature03265

Mulitza, S., Chiessi, C. M., Schefuß, E., Lippold, J., Wichmann, D., Antz, B., Mackensen, A., Paul, A., Prange, M., Rehfeld, K., Werner, M., Bickert, T., Frank, N., Kuhnert, H., Lynch-Stieglitz, J., Portilho-Ramos, R. C., Sawakuchi, A. O., Schulz, M., Schwenk, T., … Zhang, Y. (2017). Synchronous and proportional deglacial changes in Atlantic meridional overturning and northeast Brazilian precipitation. *Paleoceanography*, *32*(6), 622–633. https://doi.org/10.1002/2017PA003084

Nicholson, S. E. (2018). The ITCZ and the seasonal cycle over equatorial Africa. *Bulletin of the American Meteorological Society*, *99*(2), 337–348. https://doi.org/10.1175/BAMS-D-16-0287.1

Novello, Valdir F., Cruz, F. W., Karmann, I., Burns, S. J., Stríkis, N. M., Vuille, M., Cheng, H., Lawrence Edwards, R., Santos, R. V., Frigo, E., & Barreto, E. A. S. (2012). Multidecadal climate variability in Brazil's Nordeste during the last 3000 years based on speleothem isotope records. *Geophysical Research Letters*, *39*(23), 1–6. https://doi.org/10.1029/2012GL053936

Novello, Valdir Felipe, William da Cruz, F., Vuille, M., Pereira Silveira Campos, J. L.,

Stríkis, N. M., Apaéstegui, J., Moquet, J. S., Azevedo, V., Ampuero, A., Utida, G., Wang, X., Paula-Santos, G. M., Jaqueto, P., Ruiz Pessenda, L. C., Breecker, D. O., & Karmann, I. (2021). Investigating δ13C values in stalagmites from tropical South America for the last two millennia. *Quaternary Science Reviews*, *255*. https://doi.org/10.1016/j.quascirev.2021.106822

O'Brien, S. R., Mayewski, P. A., Meeker, L. D., Meese, D. A., Twickler, M. S., & Whitlow, S. (1995). Reconstructed from a Greenland Ice Core. *Science*, *270*(21), 1962–1964.

Oppo, D. W., McManus, J. F., & Cullen, J. L. (2003). Deepwater variability in the Holocene epoch. *Nature*, *422*(6929), 277–277. https://doi.org/10.1038/422277b

Pérez, W. (1970). Comportamiento fisiológico humano en condiciones subterráneas durante un mes dentro de la Cueva del Guácharo, Venezuela. *Boletin de La Sociedad Venezolana de Espeleología*, *3*(1), 37–49.

Peterson, L. C., Haug, G. H., Hughen, K. A., & Rohl, U. (2000). Rapid changes in the hydrologic cycle of the tropical Atlantic during the last glacial. *Science*, *290*(5498), 1947–1951. https://doi.org/10.1126/science.290.5498.1947

Peterson, L. C., Haug, G. H., Murray, R. W., Yarincik, K. M., King, J. W., Bralower, T. J., Kameo, K., Rutherford, S. D., & Pearce, R. B. (2000). Late Quaternary stratigraphy and sedimentation at Site 1002, Cariaco Basin (Venezuela). *Proceedings of the Ocean Drilling Program: Scientific Results*, *165*, 85–99. https://doi.org/10.2973/odp.proc.sr.165.017.2000

Peterson, Larry C., & Haug, G. H. (2006). Variability in the mean latitude of the Atlantic Intertropical Convergence Zone as recorded by riverine input of sediments to the Cariaco Basin (Venezuela). *Palaeogeography, Palaeoclimatology, Palaeoecology*, *234*(1), 97–113. https://doi.org/10.1016/j.palaeo.2005.10.021

Pfahl, S., & Sodemann, H. (2014). What controls deuterium excess in global precipitation? *Climate of the Past*, *10*(2), 771–781. https://doi.org/10.5194/cp-10-771-2014

Philander, S. G. H., Gu, D., Halpern, D., Lambert, G., Lau, N. C., Li, T., & Pacanowski, R.

C. (1996). Why the ITCZ is mostly north of the equator. *Journal of Climate*, *9*, 2958–2972. https://doi.org/https://doi.org/10.1175/1520-0442(1996)009<2958:WTIIMN>2.0.CO;2.

Polissar, P. J., Abbott, M. B., Wolfe, A. P., Bezada, M., Rull, V., & Bradley, R. S. (2006). Solar modulation of little ice age climate in the tropical andes. *Proceedings of the National Academy of Sciences of the United States of America*, *103*(24), 8937–8942. https://doi.org/10.1073/pnas.0603118103

Poveda, G., Waylen, P. R., & Pulwarty, R. S. (2006). Annual and inter-annual variability of the present climate in northern South America and southern Mesoamerica. *Palaeogeography, Palaeoclimatology, Palaeoecology*, *234*(1), 3–27. https://doi.org/10.1016/j.palaeo.2005.10.031

Pulwarty, R. S., Barry, R. G., & Riehl, H. (1992). Annual and Seasonal Patterns of Rainfall Variability over Venezuela (Jährliche und jahreszeitliche Muster der Niederschlagsvariabilität in Venezuela). *Erdkunde*, *46*(3/4), 273–289.

R Core Team. (2022). *R: A language and environment for statistical computing.* R Foundation for Statistical Computing. https://www.r-project.org/.

Ramirez, V. M. (2018). *Influência da zona de Convergência Intertropical na Monção Sul-Americana durante o Último Período Glacial com base em registros geoquímicos de espeleotemas da Colômbia*. [Tese de doutorado, Universidade de São Paulo].

Riehl, H. (1979). Occurrence and structure of the equatorial trough zone in Venezuela. *Quarterly Journal of the Royal Meteorological Society*, *105*, 217–229.

Rod, E. (1959). Cueva del Guacharo (Notas Geológicas). *Boletin de Geología*, *5*(10), 107–116.

Rozanski, K., Araguás-Araguás, L., & Gonfiantini, R. (1993). Isotopic Patterns in Modern Global Precipitation. *Climate Change in Continental Isotopic Records: American Geophysical Union Geophysical Monograph*, *78*, 1–36. https://doi.org/10.1029/gm078p0001

Rühlemann, C., Mulitza, S., Müller, P. J., Wefer, G., & Zahn, R. (1999). Warming of the tropical Atlantic Ocean and slowdown of thermohaline circulation during the last deglaciation. *Nature*, *402*, 511–514.

Schmittner, A., Latif, M., & Schneider, B. (2005). Model projections of the North Atlantic thermohaline circulation for the 21st century assessed by observations. *Geophysical Research Letters*, *32*(23), 1–4. https://doi.org/10.1029/2005GL024368

Schneider, T., Bischoff, T., & Haug, G. H. (2014). Migrations and dynamics of the intertropical convergence zone. *Nature*, *513*(7516), 45–53. https://doi.org/10.1038/nature13636

Scholz, D., & Hoffmann, D. L. (2011). StalAge - An algorithm designed for construction of speleothem age models. *Quaternary Geochronology*, *6*(3–4), 369–382. https://doi.org/10.1016/j.quageo.2011.02.002

Scholz, D., Hoffmann, D. L., Hellstrom, J., & Bronk Ramsey, C. (2012). A comparison of different methods for speleothem age modelling. *Quaternary Geochronology*, *14*, 94–104. https://doi.org/10.1016/j.quageo.2012.03.015

Schulz, M., & Mudelsee, M. (2002). REDFIT: Estimating red-noise spectra directly from unevenly spaced paleoclimatic time series. *Computers and Geosciences*, *28*(3), 421–426. https://doi.org/10.1016/S0098-3004(01)00044-9

Serrato Marks, G., Medina-Elizalde, M., Burns, S., Weldeab, S., Lases-Hernandez, F., Cazares, G., & McGee, D. (2021). Evidence for Decreased Precipitation Variability in the Yucatán Peninsula During the Mid-Holocene. *Paleoceanography and Paleoclimatology*, *36*(5), 1–21. https://doi.org/10.1029/2021PA004219

SEV. (1973). Catastro Espeleológico de Venezuela. Mi. 35-Cueva Alfredo Jahn. *Boletin de La Sociedad Venezolana de Espeleología*, *4*(1), 63–72.

Sharp, Z. (2017). *Principles of Stable Isotope Geochemistry* (2nd Editio). https://doi.org/https://doi.org/10.25844/h9q1-0p82

Stein, A. F., Draxler, R. R., Rolph, G. D., Stunder, B. J. B., Cohen, M. D., & Ngan, F.

(2015). Noaa's Hysplit atmospheric transport and dispersion modeling system. *Bulletin of the American Meteorological Society*, *96*(12), 2059–2077. https://doi.org/10.1175/BAMS-D-14-00110.1

Stríkis, N. M., Cruz, F. W., Cheng, H., Karmann, I., Edwards, R. L., Vuille, M., Wang, X., de Paula, M. S., Novello, V. F., & Auler, A. S. (2011). Abrupt variations in South American monsoon rainfall during the Holocene based on a speleothem record from central-eastern Brazil. *Geology*, *39*(11), 1075–1078. https://doi.org/10.1130/G32098.1

Sutton, R. T., & Hodson, D. L. R. (2005). Ocean science: Atlantic Ocean forcing of North American and European summer climate. *Science*, *309*(5731), 115–118. https://doi.org/10.1126/science.1109496

SVE. (1968). Catastro Espeleológico de Venezuela. Mo.1-Cueva del Guácharo. 1ra Parte. *Boletin de La Sociedad Venezolana de Espeleología*, *1*(2), 97–118.

SVE. (1971). Catastro Espeleológico de Venezuela. Mo.1-Cueva del Guácharo. 2da Parte. *Boletin de La Sociedad Venezolana de Espeleología*, *3*(2), 116–131.

Sweere, T., van den Boorn, S., Dickson, A. J., & Reichart, G. J. (2016). Definition of new trace-metal proxies for the controls on organic matter enrichment in marine sediments based on Mn, Co, Mo and Cd concentrations. *Chemical Geology*, *441*, 235–245. https://doi.org/10.1016/j.chemgeo.2016.08.028

Tannenbaum, B., & Wrege, P. (1978). Ecología del Guácharo en Venezuela (Steatornis caripensis). *Boletín de La Academia de Ciencias Físicas Matemáticas y Naturales*, *115*, 73–81.

Torrence, C., & Compo, G. P. (1998). A Practical Guide to Wavelet Analysis. *Bulletin of the American Meteorological Society*, *79*(1), 61–78. https://doi.org/10.1175/1520-0477(1998)079<0061:APGTWA>2.0.CO;2

Urbani, F. (1971). Carsos de Venezuela, Parte 1: Serranía del Interior, Oriente de Venezuela. *Boletin de La Sociedad Venezolana de Espeleología*, *3*(2), 87–97.

Urbani, F. (1973). Carsos de Venezuela, Parte 2: Calizas Metamórficas de la Cordillera de la Costa. *Boletin de La Sociedad Venezolana de Espeleología*, *4*(1), 15–37.

Utida, G., Cruz, F. W., Santos, R. V., Sawakuchi, A. O., Wang, H., Pessenda, L. C. R., Novello, V. F., Vuille, M., Strauss, A. M., Borella, A. C., Stríkis, N. M., Guedes, C. C. F., Dias De Andrade, F. R., Zhang, H., Cheng, H., & Edwards, R. L. (2020). Climate changes in Northeastern Brazil from deglacial to Meghalayan periods and related environmental impacts. *Quaternary Science Reviews*, *250*. https://doi.org/10.1016/j.quascirev.2020.106655

Vellinga, M., & Wood, R. A. (2002). Global climatic impacts of a collapse of the atlantic thermohaline circulation. *Climatic Change*, *54*(3), 251–267. https://doi.org/10.1023/A:1016168827653

Vuille, M., Bradley, R. S., Werner, M., Healy, R., & Keimig, F. (2003). Modeling δ18O in precipitation over the tropical Americas: 1. Interannual variability and climatic controls. *Journal of Geophysical Research: Atmospheres*, *108*(6). https://doi.org/10.1029/2001jd002038

Vuille, M., Burns, S. J., Taylor, B. L., Cruz, F. W., Bird, B. W., Abbott, M. B., Kanner, L. C., Cheng, H., & Novello, V. F. (2012). A review of the South American monsoon history as recorded in stable isotopic proxies over the past two millennia. *Climate of the Past*, *8*(4), 1309–1321. https://doi.org/10.5194/cp-8-1309-2012

Waliser, D. E., & Gautier, C. (1993). A Satellite-derived Climatology of the ITCZ. *Journal of Climate*, *6*, 2162–2174.

Wang, C., & Enfield, D. B. (2001). The tropical western hemisphere warm pool. *Geophysical Research Letters*, *28*(8), 1635–1638. https://doi.org/10.1029/2000GL011763

Wang, Chunzai, Lee, S. K., & Enfield, D. B. (2007). Impact of the Atlantic warm pool on the summer climate of the Western Hemisphere. *Journal of Climate*, *20*(20), 5021–5040. https://doi.org/10.1175/JCLI4304.1

Wang, X., Auler, A. S., Edwards, L. L., Cheng, H., Cristalli, P. S., Smart, P. L., Richards, D. A., & Shen, C. C. (2004). Wet periods in northeastern Brazil over the past 210 kyr linked to distant climate anomalies. *Nature*, *432*(7018), 740–743. https://doi.org/10.1038/nature03067

Winter, A., Miller, T., Kushnir, Y., Sinha, A., Timmermann, A., Jury, M. R., Gallup, C., Cheng, H., & Edwards, R. L. (2011). Evidence for 800 years of North Atlantic multi-decadal variability from a Puerto Rican speleothem. *Earth and Planetary Science Letters*, *308*(1–2), 23–28. https://doi.org/10.1016/j.epsl.2011.05.028

Winter, A., Zanchettin, D., Lachniet, M., Vieten, R., Pausata, F. S. R., Ljungqvist, F. C., Cheng, H., Edwards, R. L., Miller, T., Rubinetti, S., Rubino, A., & Taricco, C. (2020). Initiation of a stable convective hydroclimatic regime in Central America circa 9000 years BP. *Nature Communications*, *11*(1), 1–8. https://doi.org/10.1038/s41467-020-14490-y

Wolff, E. W., Chappellaz, J., Blunier, T., Rasmussen, S. O., & Svensson, A. (2010). Millennial-scale variability during the last glacial: The ice core record. *Quaternary Science Reviews*, *29*(21–22), 2828–2838. https://doi.org/10.1016/j.quascirev.2009.10.013

Wurtzel, J. B., Black, D. E., Thunell, R. C., Peterson, L. C., Tappa, E. J., & Rahman, S. (2013). Mechanisms of southern Caribbean SST variability over the last two millennia. *Geophysical Research Letters*, *40*(22), 5954–5958. https://doi.org/10.1002/2013GL058458

Yarincik, K. M., Murray, R. W., Lyons, T. W., Peterson, L. C., & Haug, G. H. (2000). Oxygenation history of bottom waters in the Cariaco Basin, Venezuela, over the past 578,000 years: Results from redox-sensitive metals (Mo, V, Mn, and Fe). *Paleoceanography*, *15*(6), 593–604. https://doi.org/10.1029/1999PA000401

11. APPENDIX

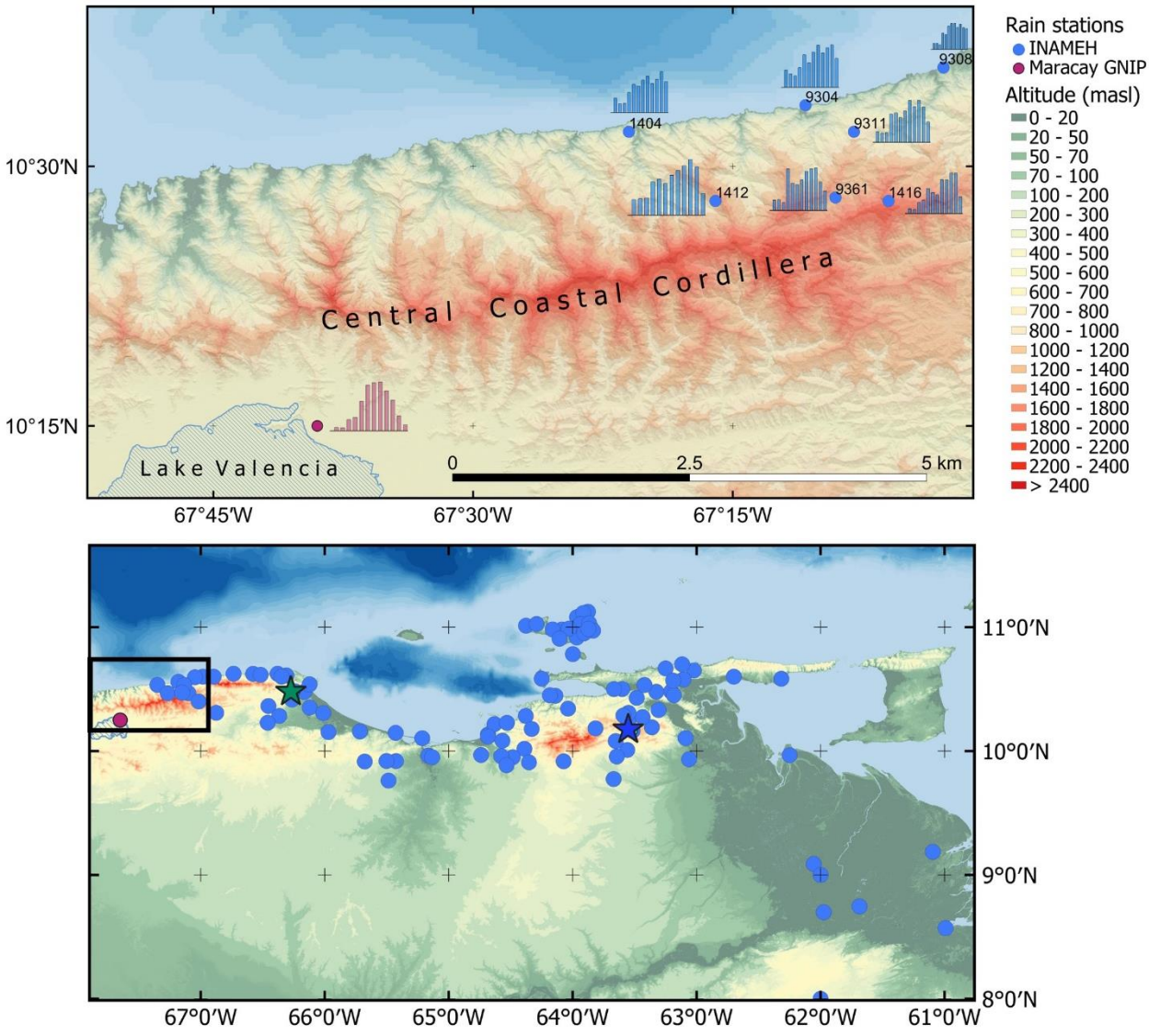

Fig. A1. Monthly mean precipitation histograms of INAMEH stations in the Central Coastal Cordillera- Serranía Interior. Very small (i.e. 9308), small (i.e. 1404, 1412, 1416, 9304, 9311, 9361) and medium (i.e. 1412) histograms denote mean annual precipitation ranges between 0-500, 500-1000 and 1000-1500 mm, respectively. Pink dot: Maracay GNIP station with isotopic data in precipitation.

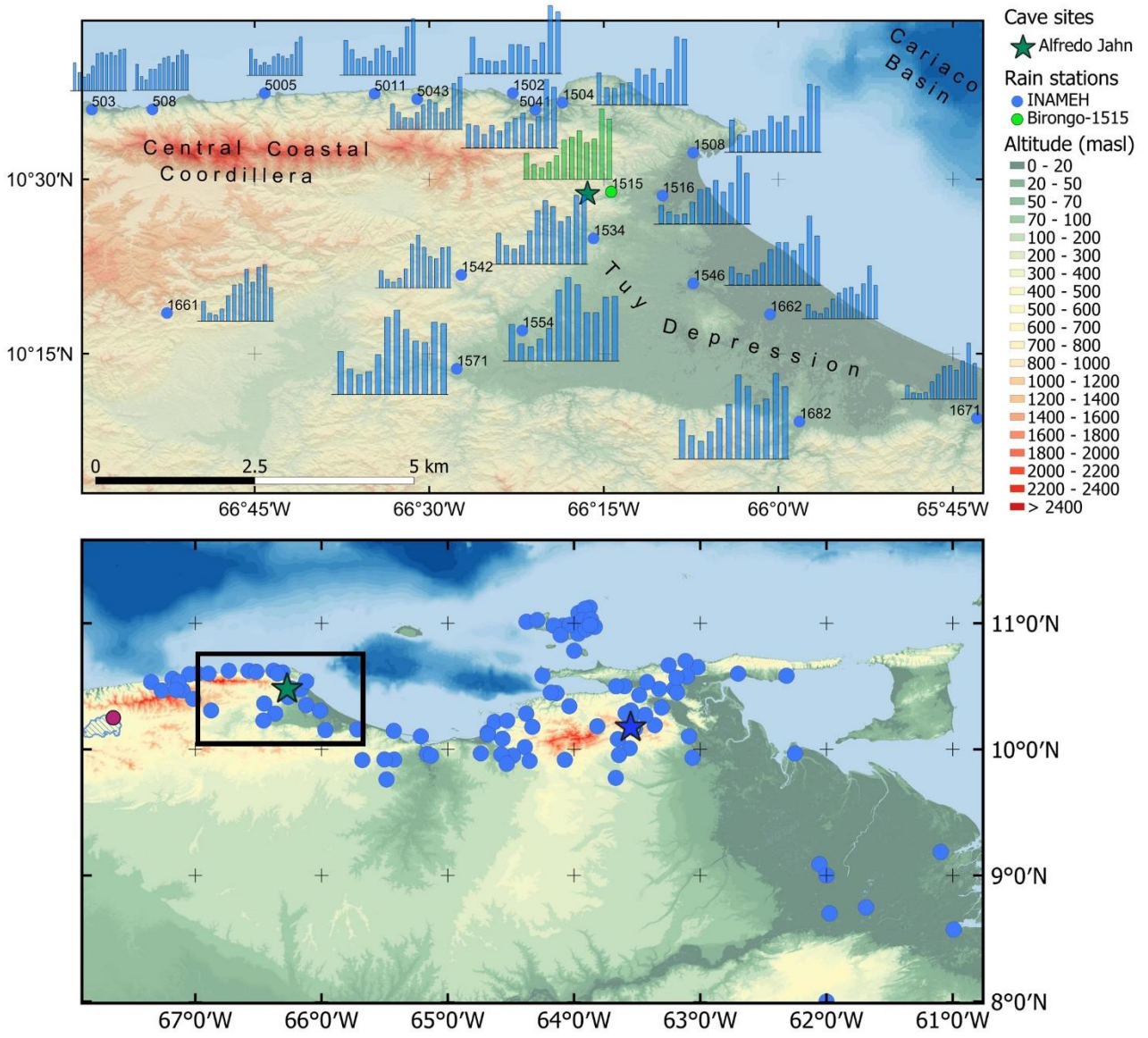

Fig. A2. Monthly mean precipitation histograms of INAMEH stations in the Central Coastal Cordillera- Serranía Litoral and Tuy Depression. Small (i.e. 503, 508, 5005), medium (i.e. 1542, 1661, 1662, 1671, 5011, 5043), large (i.e. 1502, 1504, 1508, 1515, 1534, 1516, 1546, 5041) and very large (i.e. 1554, 1571, 1682) histograms denote annual precipitation ranges between 500-1000, 1000-1500, 1500-2000 and 2000-2500 mm, respectively. Green star: Alfredo Jahn Cave. Green dot: Birongo-1515 closest station to Alfredo Jahn Cave.

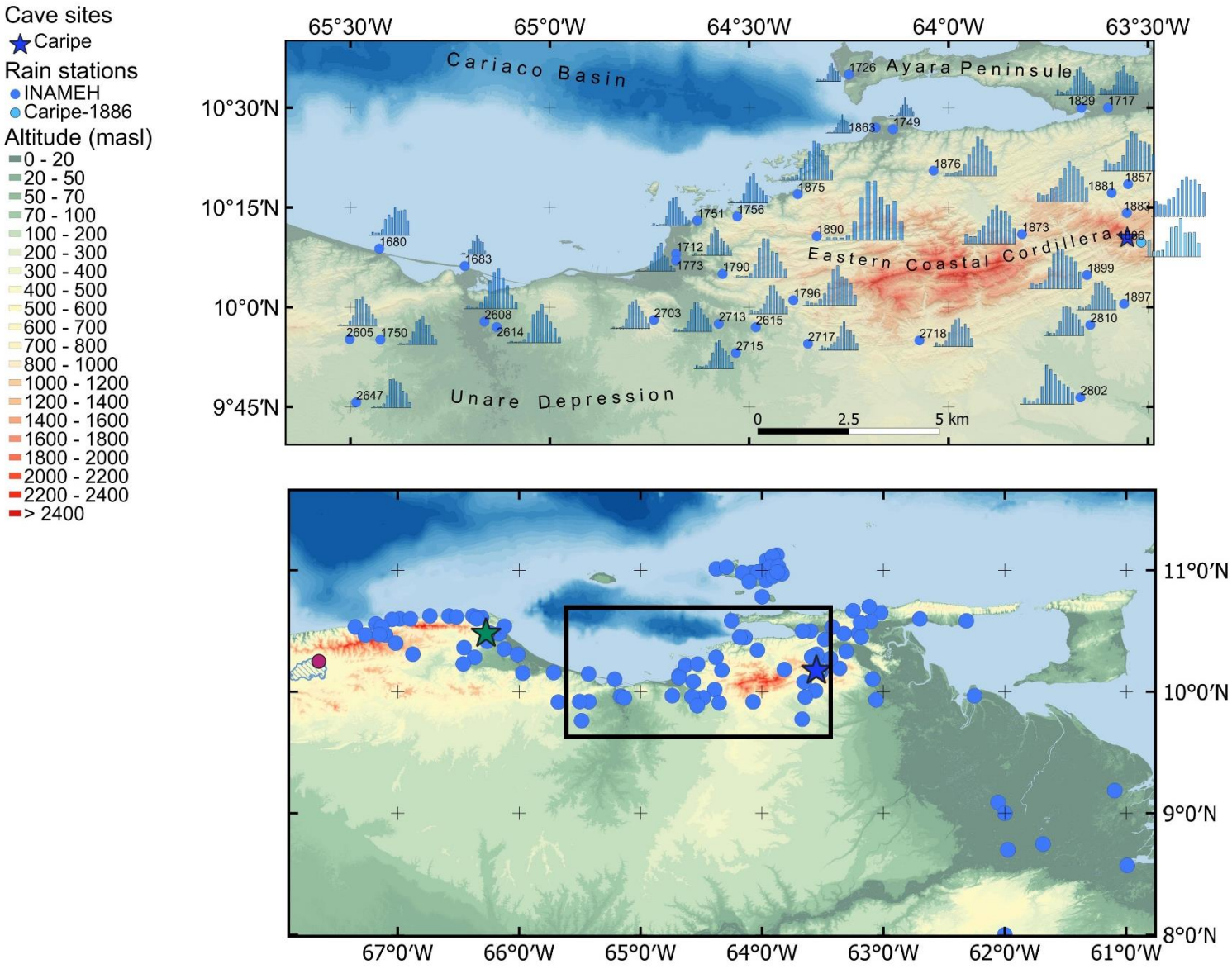

Fig. A3. Monthly mean precipitation histograms of INAMEH stations in the northern Unare Depression, Eastern Coastal Cordillera and Ayara Peninsule. Very small (i.e. 1726, 1735, 1749, 1683), small (i.e. 1680, 1712, 1717, 1750, 1751, 1756, 1773, 1829, 1897, 2605, 2607, 2615, 2617, 2647, 2703, 2713, 2715, 2717, 2718, 2810), medium (i.e. 1790, 1796, 1873, 1876, 1875, 1876, 1881, 1883, 1886, 1899, 2608, 2614), and very large histograms (i.e. 1890) denote mean annual precipitation ranges between 0-500, 100-500, 500-1000, 1000-1500 and 2000-2500 mm, respectively. Blue star: Caripe Cave. Blue dot: Caripe-1886 closest station to Caripe Cave.

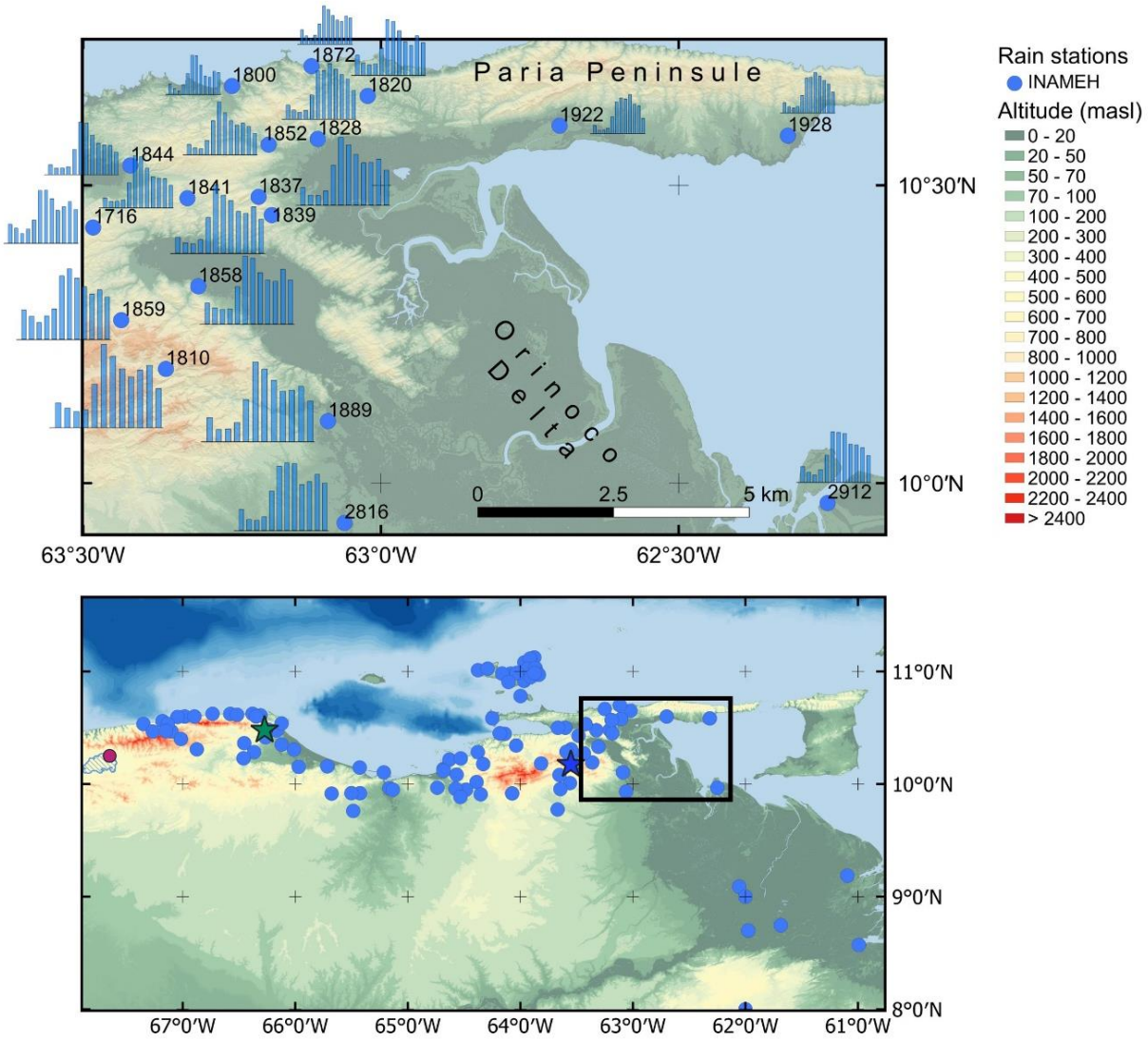

Fig. A4. Monthly mean precipitation histograms of INAMEH stations in the eastern Coastal Cordillera, Paria Peninsule and northern Orinoco Delta. Very small (i.e. 1800, 1872, 1922, 1928), small (i.e. 1716, 1820, 1828, 1841, 1844, 1852, 2912), medium (i.e. 1837, 1839 1858, 1859, 2816) and large histograms (i.e. 1810, 1889) denote annual precipitation ranges between 100-500, 500-1000 and 1000-1500, 1500-2000 mm, respectively.

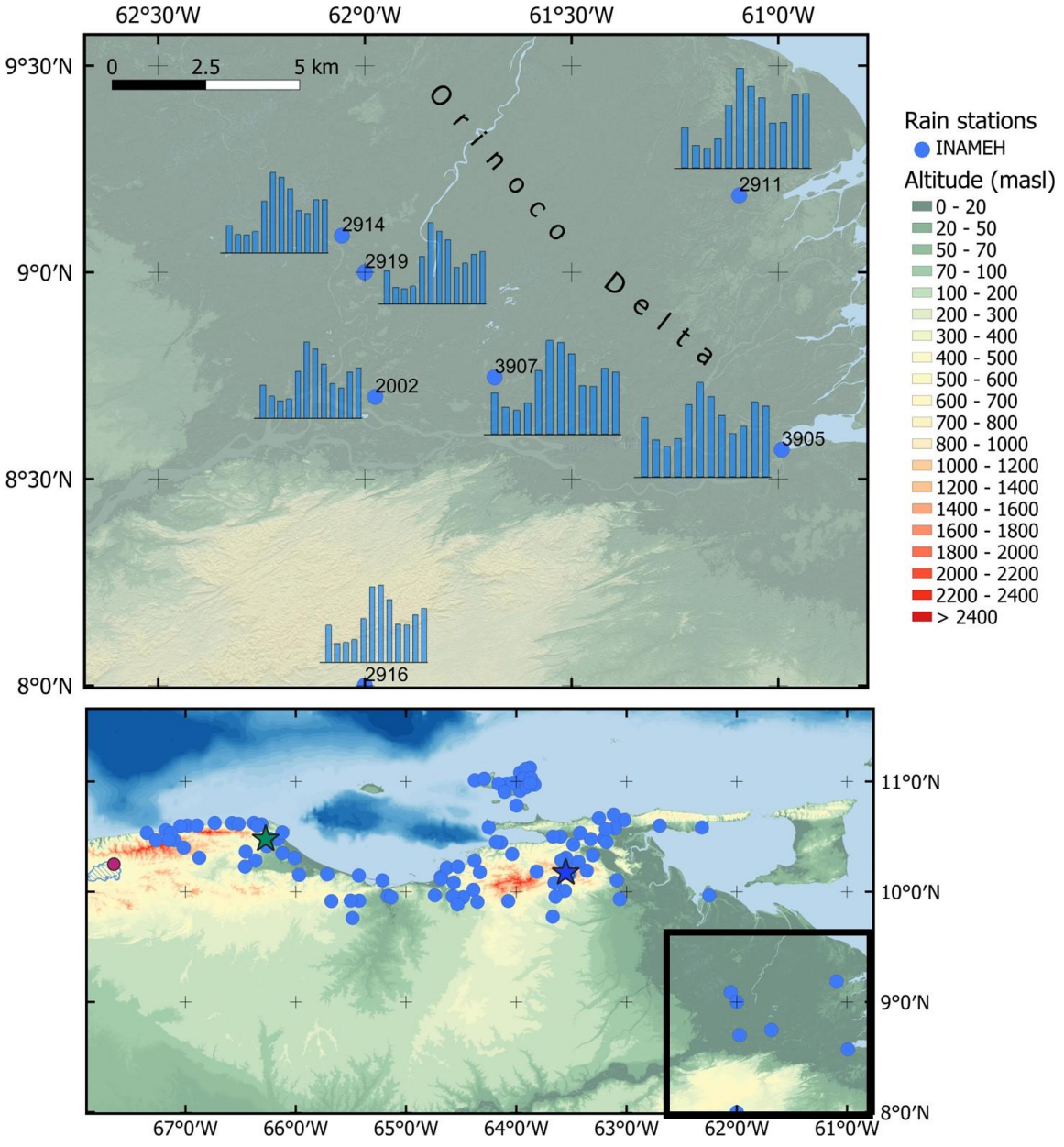

Fig. A5. Monthly mean precipitation histograms of INAMEH stations in the central portion of the Orinoco Delta. Medium (i.e. 2002, 2914, 2919, 2916) and large histograms (i.e. 2911, 3905, 3907) denote annual precipitation ranges between 1000-1500, 1500-2000 mm, respectively.

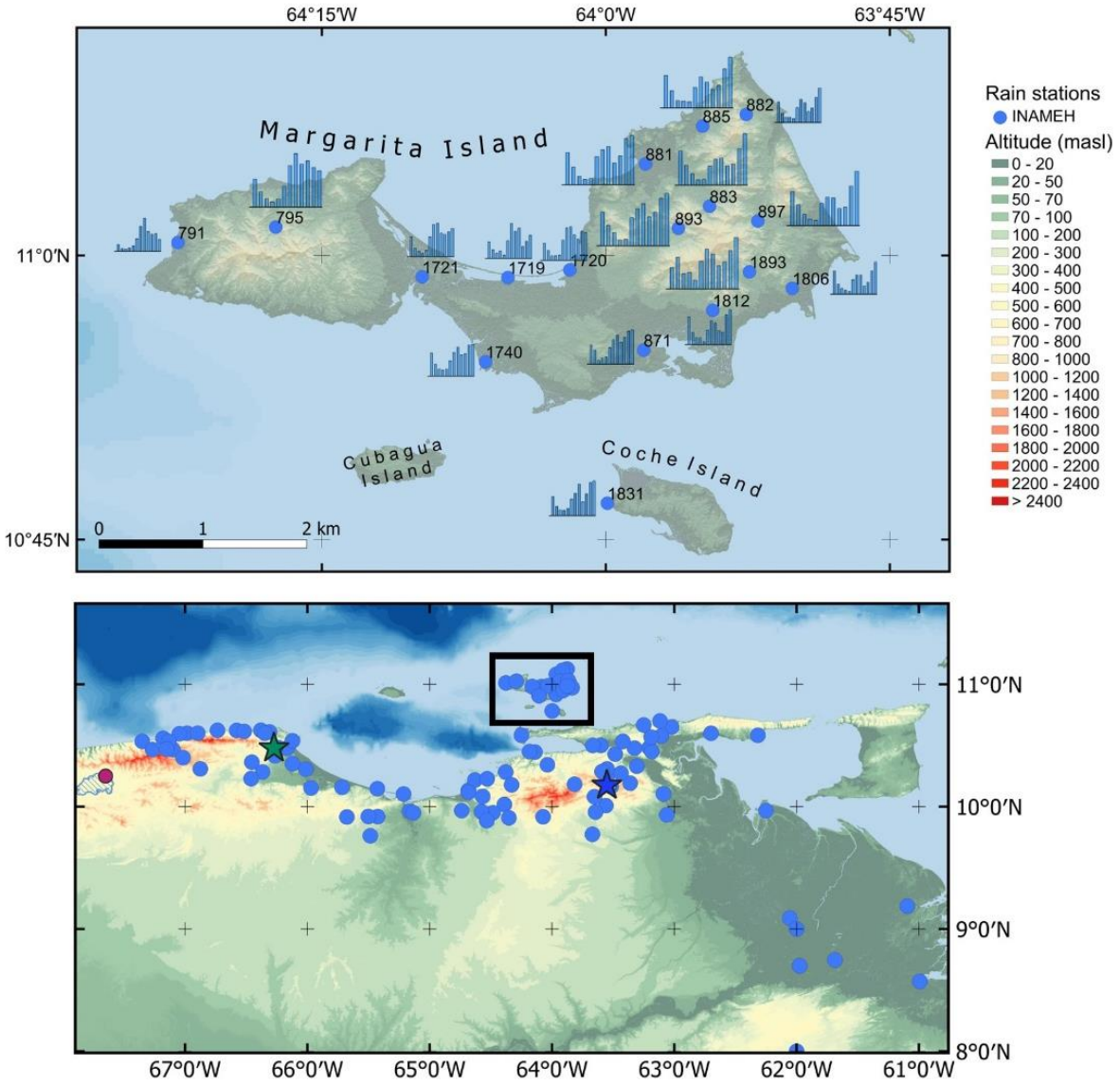

Fig. A6. Monthly mean precipitation histograms of INAMEH stations in the Margarita and Coche Islands. Very small (i.e. 791, 871, 882, 1719, 1720, 1721, 1740, 1806, 1812, 1831) and small (i.e. 795, 881, 883, 885, 893, 897, 1893) histograms denote annual mean precipitation ranges between 0-500 and 500-1000 mm, respectively.

Table A1. ^{230}Th dating results for sample VEAJ from Alfredo Jahn Cave. The error is 2s error. Dates in red were not included in the age-depth model.

Sample Number	^{238}U (ppb)		^{232}Th (ppt)		^{230}Th / ^{232}Th (atomic x10^{-6})		δ^{234}U* (measured)		^{230}Th / ^{238}U (activity)		^{230}Th Age (yr) (uncorrected)		^{230}Th Age (yr) (corrected)		$\delta^{234}U_{initial}$ ** (corrected)		^{230}Th Age (yr BP)*** (corrected)		Years C.E.	Laboratory
VEAJ-top left dating results																				
VE-AJ-2a-2	1380.8	±3.9	724	±15	1047	±21	-13.2	±1.9	0.0333	±0.0001	3745	±17	3729	±20	-13	±2	3660	±20	-1709	Xi'an Jiaotong University, China
VE-AJ-3a-8a	1751.2	±1.5	4325	±87	271	±5	-16.2	±1.2	0.0406	±0.0001	4595	±14	4522	±54	-16	±1	4452	±54	-2502	Xi'an Jiaotong University, China
VE-AJ-3a-12a	1290.0	±1.6	1036	±21	848	±17	-18.0	±1.7	0.0413	±0.0002	4686	±20	4662	±26	-18	±2	4592	±26	-2642	Xi'an Jiaotong University, China
VE-AJ-3a-29a	2091.7	±3.0	1547	±31	906	±18	-24.0	±1.4	0.0407	±0.0001	4641	±13	4619	±20	-24	±1	4549	±20	-2599	Xi'an Jiaotong University, China
VE-AJ-3A-32a	1637.2	±2.1	2043	±41	541	±11	-23.2	±1.6	0.0410	±0.0001	4671	±17	4634	±32	-23	±2	4564	±32	-2614	Xi'an Jiaotong University, China
VE-AJ-3a-44a	1393.5	±1.9	3643	±73	264	±5	-21.4	±1.7	0.0418	±0.0001	4762	±19	4684	±58	-22	±2	4614	±58	-2664	Xi'an Jiaotong University, China
VE-AJ-3a-51a	1222.5	±1.7	1501	±30	555	±11	-17.7	±1.6	0.0414	±0.0001	4691	±17	4655	±31	-18	±2	4585	±31	-2635	Xi'an Jiaotong University, China
VE-AJ-3a-57a	1046.7	±1.1	6355	±127	121	±2	-18.8	±1.5	0.0445	±0.0002	5066	±23	4886	±130	-19	±2	4816	±130	-2866	Xi'an Jiaotong University, China
VE-AJ-2A-64	1799.8	±4.7	13234	±267	100	±2	-21.2	±1.8	0.0448	±0.0001	5108	±20	4889	±156	-21	±2	4820	±156	-2869	Xi'an Jiaotong University, China
VE-AJ-3a-70a	1137.2	±1.4	8046	±161	108	±2	-20.6	±1.6	0.0465	±0.0002	5307	±22	5097	±150	-21	±2	5027	±150	-3077	Xi'an Jiaotong University, China
VE-AJ-3a-76a	2274.6	±3.0	6026	±121	330	±7	-39.6	±1.6	0.0530	±0.0001	6190	±20	6110	±60	-40	±2	6040	±60	-4090	Xi'an Jiaotong University, China
VE-AJ-3a-88a	2347.6	±3.6	2413	±48	864	±17	-46.9	±1.7	0.0538	±0.0001	6343	±21	6311	±30	-48	±2	6241	±30	-4291	Xi'an Jiaotong University, China
VE-AJ-3a-97a	8944.6	±26.9	32012	±649	249	±5	-43.8	±2.0	0.0541	±0.0002	6348	±26	6239	±81	-45	±2	6169	±81	-4219	Xi'an Jiaotong University, China
VE-AJ-3a-96a	4753.7	±11.9	14912	±301	210	±4	-41.7	±1.7	0.0400	±0.0001	4647	±16	4552	±69	-42	±2	4482	±69	-2532	Xi'an Jiaotong University, China
VE-AJ-3a-118	1754.0	±2.9	733	±15	2246	±46	-66.8	±1.7	0.0570	±0.0002	6873	±24	6860	±26	-68	±2	6790	±26	-4840	Xi'an Jiaotong University, China
VEAJ-top right dating results																				
VE-AJ-3a-37b	1318.3	±1.5	1521	±31	480	±10	-7.4	±1.4	0.0336	±0.0001	3754	±12	3720	±27	-7	±1	3650	±27	-1700	Xi'an Jiaotong University, China
VE-AJ-3a-41b	1416.9	±2.6	6801	±137	126	±3	-8.5	±2.3	0.0368	±0.0007	4124	±77	3983	±126	-9	±2	3913	±126	-1963	Xi'an Jiaotong University, China
VE-AJ-3a-46b	1764.5	±2.0	6489	±130	178	±4	2.7	±1.4	0.0396	±0.0001	4395	±13	4288	±77	3	±1	4218	±77	-2268	Xi'an Jiaotong University, China
VE-AJ-3a-56b	1980.6	±3.4	6065	±122	219	±4	-19.0	±2.0	0.0408	±0.0001	4629	±18	4538	±67	-19	±2	4468	±67	-2518	Xi'an Jiaotong University, China
VE-AJ-3a-61b	1048.8	±1.6	9645	±193	84	±2	-13.1	±1.8	0.0470	±0.0003	5325	±32	5054	±195	-13	±2	4984	±195	-3034	Xi'an Jiaotong University, China
VE-AJ-3a-68b	1511.7	±2.1	4143	±83	259	±5	-19.2	±1.7	0.0430	±0.0001	4888	±19	4807	±61	-19	±2	4737	±61	-2787	Xi'an Jiaotong University, China
VE-AJ-3a-81b	1190.0	±1.9	1368	±28	638	±13	-18.7	±1.9	0.0445	±0.0002	5063	±23	5029	±34	-19	±2	4959	±34	-3009	Xi'an Jiaotong University, China
VE-AJ-3a-92b	1622.6	±2.5	6887	±138	195	±4	-29.0	±1.8	0.0502	±0.0002	5790	±22	5663	±93	-29	±2	5593	±93	-3643	Xi'an Jiaotong University, China
VE-AJ-3a-99b	3340.2	±7.1	12097	±243	260	±5	-49.1	±1.8	0.0572	±0.0002	6764	±23	6653	±82	-50	±2	6583	±82	-4633	Xi'an Jiaotong University, China
VE-AJ-3a-103b	2802.8	±4.8	9510	±191	275	±6	-54.6	±1.6	0.0565	±0.0001	6724	±20	6619	±77	-56	±2	6549	±77	-4599	Xi'an Jiaotong University, China
VE-AJ-3a-103b	3503.8	±7.5	7339	±148	436	±9	-54.8	±1.6	0.0554	±0.0001	6589	±21	6524	±50	-56	±2	6454	±50	-4504	Xi'an Jiaotong University, China
VE-AJ-3a-116b	3547.2	±6.6	38419	±772	85	±2	-56.0	±2.0	0.0561	±0.0002	6690	±26	6356	±238	-57	±2	6286	±238	-4336	Xi'an Jiaotong University, China
VE-AJ-3a-97	1542.8	±1.9	9158	±184	130	±3	-53.8	±1.6	0.0470	±0.0001	5554	±20	5372	±131	-55	±2	5302	±131	-3352	Xi'an Jiaotong University, China
VE-AJ-3a-99b	3340.2	±7.1	12097	±243	260	±5	-49.1	±1.8	0.0572	±0.0002	6764	±23	6653	±82	-50	±2	6583	±82	-4633	Xi'an Jiaotong University, China
VE-AJ-3a-103b	2802.8	±4.8	9510	±191	275	±6	-54.6	±1.6	0.0565	±0.0001	6724	±20	6619	±77	-56	±2	6549	±77	-4599	Xi'an Jiaotong University, China

Table A1 (continued). ^{230}Th dating results for sample VEAJ from Alfredo Jahn Cave. The error is 2s error. Dates in red were not included in the age-depth model.

Sample Number	^{238}U (ppb)	^{232}Th (ppt)	^{230}Th / ^{232}Th (atomic x10^{-6})	δ^{234}U* (measured)	^{230}Th / ^{238}U (activity)	^{230}Th Age (yr) (uncorrected)	^{230}Th Age (yr) (corrected)	$\delta^{234}U_{initial}$ ** (corrected)	^{230}Th Age (yr BP)*** (corrected)	Years C.E.	Laboratory
VEAJ-base dating results											
VE-AJ-3a-122	3540.6 ±8.1	8796 ±177	327 ±7	-51.1 ±2.4	0.0493 ±0.0001	5825 ±23	5749 ±59	-52 ±2	5679 ±59	-3729	Xi'an Jiaotong University, China
VE-AJ-3a-124	1670.6 ±1.5	2968 ±59	492 ±10	-63.2 ±1.2	0.0530 ±0.0002	6360 ±21	6305 ±44	-64 ±1	6235 ±44	-4285	Xi'an Jiaotong University, China
VE-AJ-2a-144	2260.1 ±6.3	5826 ±118	375 ±8	-61.4 ±1.7	0.0586 ±0.0002	7039 ±27	6959 ±63	-63 ±2	6890 ±63	-4939	Xi'an Jiaotong University, China
VE-AJ-3a-154	2270.1 ±2.6	2752 ±55	760 ±15	-62.7 ±1.1	0.0559 ±0.0002	6711 ±23	6673 ±35	-64 ±1	6603 ±35	-4653	Xi'an Jiaotong University, China
VE-AJ-3a-165	2916.3 ±5.2	327 ±7	8480 ±174	-67.9 ±1.8	0.0576 ±0.0002	6966 ±24	6963 ±24	-69 ±2	6893 ±24	-4943	Xi'an Jiaotong University, China
VE-AJ-3a-183	3899.3 ±7.5	14072 ±283	286 ±6	-66.6 ±1.9	0.0626 ±0.0002	7572 ±25	7459 ±84	-68 ±2	7389 ±84	-5439	Xi'an Jiaotong University, China
VE-AJ-3a-195	4396.6 ±6.9	3403 ±68	1252 ±25	-66.4 ±1.5	0.0588 ±0.0001	7094 ±20	7070 ±26	-68 ±1	7000 ±26	-5050	Xi'an Jiaotong University, China
VE-AJ-3a-199	2541.3 ±3.9	2809 ±56	866 ±18	-43.9 ±1.7	0.0581 ±0.0002	6837 ±23	6803 ±33	-45 ±2	6733 ±33	-4783	Xi'an Jiaotong University, China
VE-AJ-3a-208	2926.0 ±6.4	4699 ±95	626 ±13	-60.6 ±2.1	0.0610 ±0.0002	7325 ±28	7275 ±45	-62 ±2	7205 ±45	-5255	Xi'an Jiaotong University, China
VE-AJ-3a-216	3703.3 ±6.6	13099 ±263	300 ±6	-63.3 ±1.6	0.0644 ±0.0002	7774 ±26	7664 ±82	-65 ±2	7594 ±82	-5644	Xi'an Jiaotong University, China
VE-AJ-3a-227	2239.0 ±3.3	4755 ±95	511 ±10	-56.9 ±1.6	0.0658 ±0.0002	7897 ±29	7831 ±55	-58 ±2	7761 ±55	-5811	Xi'an Jiaotong University, China
VE-AJ-3a-235	2632.1 ±4.3	2631 ±53	1061 ±21	-66.9 ±1.7	0.0643 ±0.0002	7791 ±26	7759 ±34	-68 ±2	7689 ±34	-5739	Xi'an Jiaotong University, China
VE-AJ-3a-245	2145.1 ±2.8	5046 ±101	471 ±10	-58.3 ±1.6	0.0672 ±0.0002	8076 ±27	8003 ±58	-60 ±2	7933 ±58	-5983	Xi'an Jiaotong University, China
VE-AJ-3a-256	2265.3 ±2.3	1024 ±21	2365 ±48	-73.2 ±1.2	0.0648 ±0.0001	7914 ±18	7900 ±21	-75 ±1	7830 ±21	-5880	Xi'an Jiaotong University, China
VE-AJ-3a-269	2055.5 ±3.0	1787 ±36	1249 ±25	-68.7 ±1.7	0.0659 ±0.0001	8007 ±24	7980 ±31	-70 ±2	7910 ±31	-5960	Xi'an Jiaotong University, China
VE-AJ-3a-275	3072.5 ±4.6	3902 ±78	803 ±16	-61.8 ±1.5	0.0618 ±0.0001	7438 ±21	7399 ±35	-63 ±2	7329 ±35	-5379	Xi'an Jiaotong University, China
VE-AJ-3a-278	1910.2 ±3.7	1500 ±30	1395 ±28	-68.3 ±1.7	0.0665 ±0.0002	8076 ±30	8051 ±34	-70 ±2	7981 ±34	-6031	Xi'an Jiaotong University, China
VE-AJ-2a-288	2708.7 ±7.4	2378 ±48	1251 ±25	-74.0 ±1.6	0.0666 ±0.0002	8148 ±30	8121 ±36	-76 ±2	8052 ±36	-6101	Xi'an Jiaotong University, China
VE-AJ-3a-304	2537.4 ±4.2	25609 ±514	124 ±3	-67.7 ±1.7	0.0762 ±0.0002	9301 ±29	8985 ±225	-69 ±2	8915 ±225	-6965	Xi'an Jiaotong University, China
VE-AJ-3a-315	2238.8 ±5.7	3638 ±73	694 ±18	-72.3 ±2.3	0.0684 ±0.0011	8361 ±136	8310 ±140	-74 ±2	8240 ±140	-6290	Xi'an Jiaotong University, China
VE-AJ-3a-322	2541.9 ±3.6	8583 ±172	348 ±7	-69.2 ±1.6	0.071 ±0.0002	8705 ±25	8599 ±79	-71 ±2	8529 ±79	-6579	Xi'an Jiaotong University, China

U decay constants: $l_{238} = 1.55125 \times 10^{-10}$ (Jaffey et al., 1971) and $l_{234} = 2.82206 \times 10^{-6}$ (Cheng et al., 2013). Th decay constant: $l_{230} = 9.1705 \times 10^{-6}$ (Cheng et al., 2013).

*$\delta^{234}U = ([^{234}U/^{238}U]_{activity} - 1) \times 1000$. ** $\delta^{234}U_{initial}$ was calculated based on ^{230}Th age (T), i.e., $\delta^{234}U_{initial} = \delta^{234}U_{measured} \times e^{l_{234}T}$.

Corrected ^{230}Th ages assume the initial $^{230}Th/^{232}Th$ atomic ratio of 4.4 ±2.2 x10^{-6}. Those are the values for a material at secular equilibrium, with the bulk earth $^{232}Th/^{238}U$ value of 3.8.

The errors are arbitrarily assumed to be 50%.

***B.P. stands for "Before Present" where the "Present" is defined as the year 1950 A.D.

Table A2. ^{230}Th dating results for sample VECA from Caripe Cave. The error is 2s error. Dates in red were not included in the age-depth model.

Sample Number	^{238}U (ppb)	^{232}Th (ppt)	^{230}Th / ^{232}Th (atomic x10^{-6})	δ^{234}U* (measured)	^{230}Th / ^{238}U (activity)	^{230}Th Age (yr) (uncorrected)	^{230}Th Age (yr) (corrected)	$\delta^{234}U_{initial}$ ** (corrected)	^{230}Th Age (yr BP)*** (corrected)	Years C.E.	Laboratory
VE_CA-3a-2	621.3 ±0.8	334 ±7	12 ±5	-34.4 ±1.4	0.0004 ±0.0002	43 ±19	27 ±22	-34 ±1	-43 ±22	1993	University of Minnesota, EEUU
VE-CA-3a-5	656.4 ±0.7	449 ±9	17.2 ±2.8	-33.8 ±1.4	0.00071 ±0.00011	81 ±13	60 ±19	-33.8 ±1.4	-10 ±19	1960	University of Minnesota, EEUU
VE_CA_3a-9	685.9 ±0.8	941 ±19	58 ±2	-28.9 ±1.3	0.0048 ±0.0001	540 ±13	499 ±32	-29 ±1	429 ±32	1521	University of Minnesota, EEUU
VE-CA-3a-19	632.7 ±0.7	86 ±2	956 ±52	-29.3 ±1.4	0.0079 ±0.0004	893 ±44	889 ±44	-29 ±1	820 ±44	1131	Xi'an Jiaotong University, China
VE-CA-3a-20	526.6 ±0.7	237 ±5	187 ±9	-31.1 ±1.4	0.0051 ±0.0002	576 ±26	562 ±27	-31 ±1	492 ±27	1458	University of Minnesota, EEUU
VE-CA-3a-32	574.8 ±0.8	80 ±2	747 ±28	-23.9 ±1.8	0.0063 ±0.0002	710 ±20	706 ±21	-24 ±2	637 ±21	1314	Xi'an Jiaotong University, China
VE-CA-a-40	425.3 ±0.5	228 ±5	203 ±12	-28.7 ±1.3	0.0066 ±0.0004	743 ±42	727 ±44	-29 ±1	657 ±44	1293	University of Minnesota, EEUU
VE-CA-3a-60	709.7 ±1.3	88 ±2	1181 ±34	-28.0 ±2.1	0.0089 ±0.0001	1001 ±16	997 ±17	-28 ±2	928 ±17	1023	Xi'an Jiaotong University, China
VE-CA-3a-65	611.5 ±0.8	160 ±4	659 ±21	-26.9 ±1.3	0.0104 ±0.0002	1177 ±25	1169 ±26	-27 ±1	1096 ±26	851	University of Minnesota, EEUU
VE-CA-3a-68	653.0 ±0.7	73 ±2	1363 ±39	-25.2 ±1.4	0.0093 ±0.0001	1042 ±14	1039 ±14	-25 ±1	969 ±14	981	Xi'an Jiaotong University, China
VE-CA-3a-73	651.8 ±0.6	104 ±2	993 ±29	-29.2 ±1.3	0.0096 ±0.0002	1082 ±19	1078 ±19	-29 ±1	1009 ±19	942	Xi'an Jiaotong University, China
VE-CA-3a-84	579.7 ±0.7	81 ±2	1328 ±37	-24.4 ±1.6	0.0113 ±0.0001	1265 ±16	1261 ±16	-25 ±2	1191 ±16	759	Xi'an Jiaotong University, China
VE-CA-3a-100	538.7 ±0.8	96 ±2	1074 ±29	-26.9 ±1.9	0.0117 ±0.0002	1315 ±19	1309 ±19	-27 ±2	1240 ±19	711	Xi'an Jiaotong University, China
VE-CA-3a-116	753.7 ±1.2	52 ±2	3086 ±98	-26.8 ±1.9	0.0130 ±0.0001	1470 ±16	1468 ±16	-27 ±2	1399 ±16	552	Xi'an Jiaotong University, China
VE-CA-3a-124	357.9 ±0.5	106 ±2	927 ±25	-27.2 ±1.8	0.0167 ±0.0003	1887 ±30	1878 ±30	-27 ±2	1809 ±30	142	Xi'an Jiaotong University, China
VE-CA-3a-134	496.6 ±0.5	414 ±8	325 ±8	-24.0 ±1.5	0.0164 ±0.0002	1853 ±23	1828 ±29	-24 ±1	1758 ±29	192	Xi'an Jiaotong University, China
VE-CA-3a-148	528.8 ±0.5	186 ±4	765 ±18	-24.7 ±1.4	0.0163 ±0.0002	1843 ±19	1833 ±21	-25 ±1	1763 ±21	187	Xi'an Jiaotong University, China
VE-CA-3a-151	510.8 ±0.4	105 ±2	1333 ±34	-25.4 ±1.2	0.0167 ±0.0002	1880 ±21	1874 ±21	-26 ±1	1804 ±21	146	Xi'an Jiaotong University, China
VE-CA-3a-156	626.3 ±0.8	179 ±4	984 ±23	-26.8 ±1.7	0.0170 ±0.0002	1924 ±20	1915 ±21	-27 ±2	1846 ±21	105	Xi'an Jiaotong University, China
VE-CA-3a-158	491.3 ±0.4	126 ±3	1078 ±27	-26.7 ±1.1	0.0168 ±0.0002	1895 ±22	1887 ±23	-27 ±1	1817 ±23	133	Xi'an Jiaotong University, China
VE-CA-3a-165	588.6 ±0.6	185 ±4	1038 ±24	-26.2 ±1.3	0.0197 ±0.0002	2234 ±22	2225 ±23	-26 ±1	2156 ±23	-205	Xi'an Jiaotong University, China
VE-CA-3a-173	540.6 ±0.8	173 ±4	897 ±21	-28.5 ±1.9	0.0174 ±0.0002	1974 ±23	1964 ±24	-29 ±2	1894 ±24	56	Xi'an Jiaotong University, China
VE-CA-3a-178	180.1 ±0.2	80 ±2	638 ±23	-24.9 ±1.6	0.0171 ±0.0005	1930 ±52	1917 ±52	-25 ±2	1847 ±52	103	Xi'an Jiaotong University, China
VE-CA-3a-200	492.6 ±0.6	111 ±2	1313 ±32	-24.4 ±1.4	0.0179 ±0.0002	2025 ±22	2018 ±22	-25 ±1	1948 ±22	2	Xi'an Jiaotong University, China
VE-CA-3a-229	541.8 ±0.7	295 ±6	573 ±13	-22.3 ±1.5	0.0189 ±0.0002	2134 ±19	2118 ±22	-22 ±2	2048 ±22	-98	Xi'an Jiaotong University, China
VE-CA-3a-233	497.6 ±0.5	168 ±4	926 ±21	-23.7 ±1.4	0.0190 ±0.0002	2139 ±19	2129 ±20	-24 ±1	2059 ±20	-109	Xi'an Jiaotong University, China
VE-CA-3a-246	433.3 ±0.5	326 ±7	429 ±10	-21.2 ±1.4	0.0196 ±0.0002	2204 ±23	2182 ±28	-21 ±1	2112 ±28	-162	Xi'an Jiaotong University, China
VE-CA-3a-265	374.5 ±0.5	326 ±7	377 ±9	-22.3 ±1.9	0.0199 ±0.0002	2244 ±27	2218 ±33	-22 ±2	2148 ±33	-198	Xi'an Jiaotong University, China

U decay constants: $l_{238} = 1.55125 \times 10^{-10}$ (Jaffey et al., 1971) and $l_{234} = 2.82206 \times 10^{-6}$ (Cheng et al., 2013). Th decay constant: $l_{230} = 9.1705 \times 10^{-6}$ (Cheng et al., 2013).

*$\delta^{234}U = ([^{234}U/^{238}U]_{activity} - 1) \times 1000$. ** $\delta^{234}U_{initial}$ was calculated based on ^{230}Th age (T), i.e., $\delta^{234}U_{initial} = \delta^{234}U_{measured} \times e^{\lambda 234 \times T}$.

Corrected ^{230}Th ages assume the initial $^{230}Th/^{232}Th$ atomic ratio of 4.4±2.2 x10^{-6}. Those are the values for a material at secular equilibrium, with the bulk earth $^{232}Th/^{238}U$ value of 3.8.

The errors are arbitrarily assumed to be 50%.

***B.P. stands for "Before Present" where the "Present" is defined as the year 1950 A.D.